TERAHERTZ MIIM RECTENNA FOR ENERGY HARVESTING APPLICATIONS

A Thesis

presented to

the Faculty of the Graduate School at

the University of Missouri-Columbia

In Partial Fulfillment

of the Requirements for the Degree

Master of Science

---

by

EVAN ALLISON

Dr. Patrick Pinhero, Thesis Supervisor

May 2018

The undersigned, appointed by the dean of the Graduate School, have examined the thesis entitled

TERAHERTZ MIIM

RECTENNA FOR ENERGY

HARVESTING

APPLICATIONS

presented by Evan Allison,

a candidate for the degree of Master of Science,

and hereby certify that, in their opinion, it is worthy of acceptance.

Dr. Patrick Pinhero

Dr. Karl Hammond

Dr. Heather Hunt

Dedication

This thesis is dedicated to those who have supported me throughout my life and education. It is especially dedicated to my parents, Mark Allison and Deb Vetter, and fiancée, Devin Gardner, for all of their love and encouragement.

Acknowledgements

My sincerest gratitude and thanks are given to my advisor, Dr. Patrick Pinhero, for his mentorship and advice over the past three years. I have learned a variety of skills from him through the opportunity he has given me in working for him.

I would also like to thank the remaining members of my thesis committee: Dr. Karl Hammond and Dr. Heather Hunt. Their time and critique of my work is immensely appreciated.

Finally, I would like to thank the collaborators that I worked with on this project through RedWave Energy. They supplied the samples tested and additionally helped evaluate and understand the results. I would also like to thank the current and former chemical engineering students that I was able to work with daily: Zach Thacker, Lucas Haley, Shendu Yang, Xiang Li, Jeff Cathey and Seth Boeke.

Table of Contents

List of Abbreviations

AC……..Alternating current

A……...Ampere

A/W……Ampere per watt

Au……Gold

BPF……Bandpass filter

Cr……Chromium

DC……Direct current

fs……Femtosecond

FSS……..Frequency selective surface

F.O.M……Figure of merit

FWHM……...Full width at half maximum

GHz……..Gigahertz

Hz……...Hertz

LT-GaAs……...Low-temperature grown gallium arsenide

MHz……..Megahertz

MIM……Metal-insulator-metal

MIIM……..Metal-insulator-insulator-metal

m……..Meter

mm……..Millimeter

mV……Millivolt

mW……Milliwatt

Ni……..Nickel

NiO……Nickel oxide

Nb_2O_5……Niobium oxide

nm……..Nanometer

nW……..Nanowatt

PCA……..Photoconductive antenna

RC……Resistance-capacitance

RF……..Radio frequency

RMS……...Root mean square

s……Second

THz……..Terahertz

THz-TDS……Terahertz time-domain spectroscopy

V……...Volt

W……Watt

ZnO……Zinc oxide

ZnTe……Zinc telluride

µm……..Micrometer

Ω……..Ohm

List of Tables

List of Figures

TERAHERTZ MIIM RECTENNA FOR ENERGY HARVESTING APPLICATIONS

Evan Allison

Dr. Patrick Pinhero, Thesis Advisor

Abstract

Harvesting energy from electromagnetic radiation has been researched for over a century. Utilizing energy harvesting antenna to collect radiation from solar and terrestrial sources has shown promise to be a viable method of energy transfer. Generally, the energy density of electromagnetic radiation increases with frequency with the highest intensity in the optical frequencies. This work focuses on harvesting of terahertz radiation utilizing a rectifying antenna. The objective is to demonstrate zero-bias rectification of alternating current terahertz radiation captured by an antenna to useable direct current with a metal-insulator-insulator-metal diode. The direct current diode characteristics are presented with a two-term exponential fit to understand the rectifying capabilities of the rectenna. The power of the terahertz source is measured and estimated. Two material sets of diodes in the rectenna are measured under illumination from the terahertz source. The zero-bias rectification demonstrated is crucial to producing energy-harvesting devices. The rectification efficiency of the rectenna is 7.1×10^{-10} and 1.7×10^{-9} for the Ni-NiO-Nb_2O_5-CrAu and Ni-NiO-ZnO-CrAu devices, respectively.

Chapter 1 Introduction

1.1 Overview

This thesis will describe the work that has been performed by the author while contributing to the nano-antenna project, a collaboration between the University of Missouri, the University of Colorado, Oregon State University, MicroContinuum Inc., and RedWave Energy, Inc. The overall motivation behind the project is to develop an antenna and metamaterial system that captures electromagnetic radiation and converts the electrical power through a high-speed diode that rectifies the power to useful direct current. The focus of this work will be on the application of a rectifying antenna, or rectenna, to convert free-space electromagnetic radiation with a frequency of 1 THz.

The first chapter of this thesis explores the history, background and applications in understanding the operation of a rectenna. The second chapter delves into analytical modeling and simulation of rectifying diodes. Evidence for a new figure of merit for the diodes in the rectenna is proposed and discussed. Thirdly, the power spectrum of the THz-TDS system is measured and compared to the Fourier electric field that is traditionally measured. Finally, in the fourth chapter, illuminated measurements of fabricated rectenna are presented. The experiments and discussion provided help to clarify the mechanism of response of the 1 THz rectenna. The fifth chapter provides a look back on these results and a look into what comes next.

1.2 Rectenna History

Harvesting energy from the sun has long been a topic of intrigue and exploration. The use of an energy harvesting antenna was studied by Nikola Tesla as a method for wireless energy transmission [1, 2]. The first researchers worked on energy transfer through antenna operating at

low frequency [3]. In the early 1960s, William C. Brown at Raytheon began proposing methods by which to use microwaves to transport energy [4]. By the mid-1960s, he demonstrated the use of a microwave powered helicopter [5]. As the operating frequency of the power transfer antennas was increasing, the necessity to add a rectifying diode to the system became apparent. The system combining the diode and the antenna is today known as a rectenna. The rectenna absorbs radiant electromagnetic energy for conversion of the alternating current (AC) power into a direct current (DC) signal for use or storage. Brown's experiments in the 1960s demonstrated successful energy transfer using a rectenna [4, 6]. Brown's work in the 1960s culminated in a microwave to DC power converter patent in 1969 [7]. Shortly thereafter, more patents in energy harvesting rectenna were filed, such as the patent for an electromagnetic wave energy converter developed by NASA and Bailey [8]. Early rectifiers achieved efficiencies as high as 90% when the rectenna system was optimized at 2.45 GHz [9]. Even as recently as 2010, Schottky diodes of GaAs-W were reported with efficiencies as high as 90% at 2.45 GHz [10], while much lower efficiencies were reported for metal-insulator-metal (MIM) diodes at the same operating frequency [11]. These efficiencies are still significantly higher than the theoretical limits for single or multi *p-n* junction solar cells of 31% and 72%, respectively [12, 13]. However, these efficiencies are still well below the thermodynamic maximum efficiency of 93% for solar radiation conversion given by the Landsberg efficiency [14],

$$\eta_{Landsberg} = 1 - \frac{4}{3}\frac{T_{Earth}}{T_{Sun}} + \frac{1}{3}\left(\frac{T_{Earth}}{T_{Sun}}\right)^4. \quad (1.2.1)$$

The temperature of the earth, T_{Earth}, is 290 K and the temperature of the sun, T_{Sun}, is 5800 K in Equation (1.2.1). It is quite unfortunate that these high efficiencies are at low frequencies where the energy density is low for both terrestrial and solar sources. Therefore, there is a pressing desire to increase the operating frequency into the optical regime where the available energy is substantially higher. This has come not without limitations, however. As the frequency of

operation increases, it has been shown that the antenna absorbs electromagnetic radiation at high efficiencies, but the limitation lies upon the rectification capability of the diode.

1.3 Rectenna Applications

While rectenna have a variety of potential applications, the focus will be on two primary utilizations: detectors and energy harvesters. Energy harvesters are the most prominent and potentially groundbreaking application of a rectenna. The rectenna presented here are designed to operate around one terahertz to begin to bridge the gap from the rectenna operating at microwave frequencies to operating frequencies in the infrared and eventually optical range. The terahertz frequency gap exists between the low frequency end of the infrared frequency spectrum, i.e. 300 GHz to 430 THz, and the high frequency end of the microwave frequency spectrum, i.e. 300 MHz to 300 GHz. The range of the terahertz gap is 100 GHz to 10 THz. The eventual goal is to create rectenna that operate in the optical frequency spectrum, i.e. 430 THz to 750 THz.

1.3.1 Detectors

Much of the recent work in rectenna design and applications has focused on their use as infrared and terahertz detectors. Some early experiments have demonstrated the use of metal-insulator-metal rectenna as detectors [15, 16]. Diodes used in detectors must be non-linear but can be symmetric. A non-linear, symmetric diode could operate as a detector if operating at bias voltage where the diode exhibits significant responsivity. MIM rectenna have been fabricated for use as infrared detectors due to their ability to be used at room temperature with a faster response time compared to conventional bolometers [17]. Rectenna designs incorporating a geometric diode, rather than a MIM diode, have also been developed as room temperature infrared detectors [18].

1.3.2 Energy Harvesters

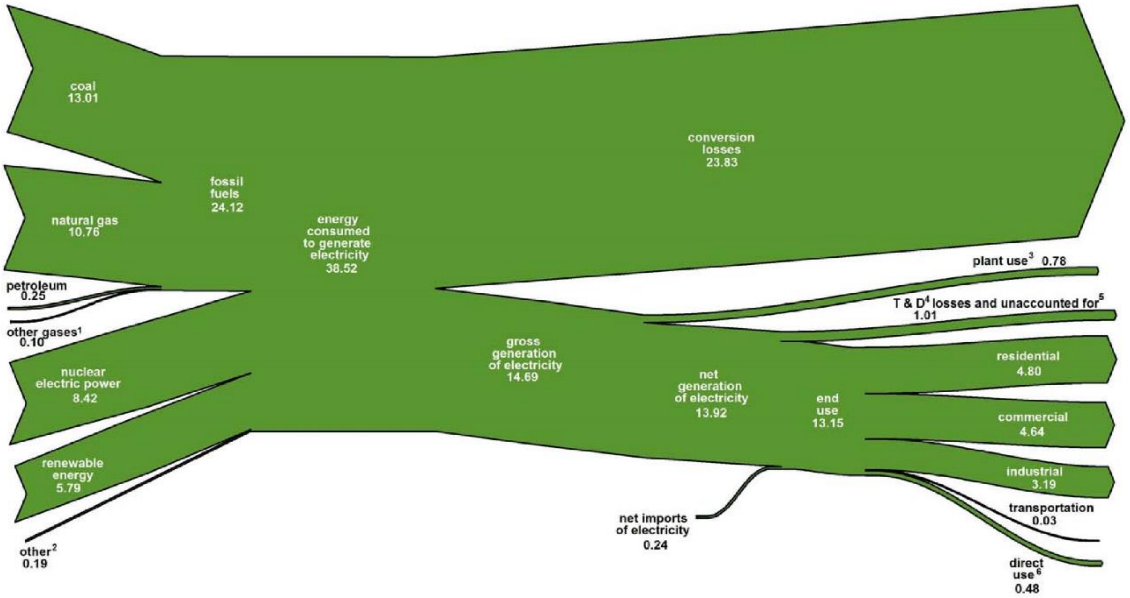

Figure 1.1: Electricity flow diagram from US Department of Energy 2017 Annual Energy Review demonstrating the energy conversion losses of electricity generation in the United States, where these conversion losses are largely losses due to heat [19].

With the world's energy demands constantly growing as the population increases, third world countries begin consuming more energy, and the fossil fuel reserves diminish, new emerging technologies will be required to provide sustainable and renewable sources of energy. Currently, many of the energy sources we utilize are subject to large efficiency losses. Harvesting that waste heat from various sources has been a topic of interest for many years with many solutions discussed, since a substantial portion of the energy losses of a system are due to heat loss. As depicted in Figure 1.1, the US Department of Energy reported in 2016 more than half of the energy input to generated electricity was lost to heat [19]. Finding a method with which the heat losses of any system can be reduced will increase overall efficiencies; therefore, reducing the amount of an energy source required to provide electricity to the United States and our dependence on the ever diminishing, but increasingly difficult to utilize, fossil fuel resources. The overall goal of this specific project is to incorporate a rectenna to a metamaterial device. The metamaterial has a given emission spectrum based on its fabrication and temperature.

Additionally, the rectenna has its own emission spectrum based on its temperature. The emission spectrum for both can be quantified using Planck's law of blackbody radiation [20],

$$B_v(v,T) = \frac{2hv^3}{c^2}\frac{1}{e^{\frac{hv}{k_BT}} - 1}, \tag{1.3.1}$$

where *v* is the frequency of the radiation, *h* is Planck's constant, *c* is the speed of light in a vacuum, k_B is Boltzmann's constant, and *T* is the temperature. If the metamaterial and rectenna are at different temperatures, the energy difference in their emission spectra is available for energy harvesting. The devices presented in this study are free-space rectenna and are not coupled to any metamaterial. They are designed to response to illumination of terahertz frequency radiation.

To this point, successful implementation of rectenna as energy harvesters has been limited. At high frequency, the poor diode efficiency dampens any return from the higher energy of these frequencies. For these diodes to be sustainable energy producers, they must have the ability to rectify the electromagnetic radiation at zero bias. Zero-bias diode rectification requires that the voltage-dependent current of the diode, or its I(V), be substantially asymmetric and non-linear.

1.4 Rectenna Background

For this section, the operating mechanism of the rectenna is presented with an emphasis on the current parameters used to characterize the diodes and reported fabrication limitations. Additionally, the design goals for the diodes used in the rectenna are defined.

In this project, metal-insulator-insulator-metal (MIIM) diodes, rather than metal-insulator-metal (MIM) diodes, are examined for converting terahertz radiation to electrical power. The double-layer insulator improves the non-linearity and asymmetry of the diodes [21]. The MIIM diodes operate on the principle of quantum electron tunneling induced by the photoelectric effect, where the important material properties are the work function of the metals, Φ, and the electron affinity of the insulator layers, X. Rectennas operating at radio and microwave

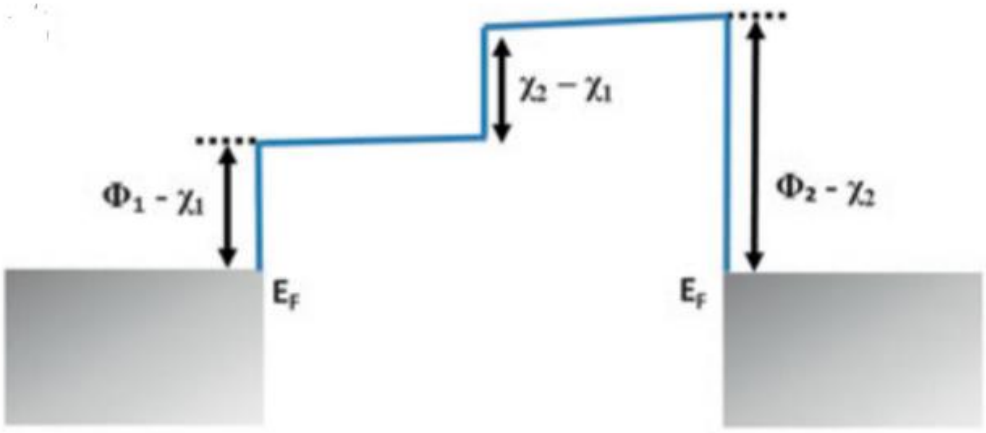

Figure 1.2: Quantum electron tunneling energy diagram for MIIM diode operating at zero-bias. The non-linearity and asymmetry of a diode is provided by the double insulators at zero-bias [26].

frequencies are governed by Maxwell's equations using the wave nature of light [22]. As the drive to increase the frequency of operation continues, the classical approach to describe the operation of the rectenna fails to explain their behavior when the radiating waves oscillate at such high frequencies [23]. The quantum nature of light must be used to describe the behavior in the terahertz, infrared and optical regimes [22, 24, 25].

In the work presented here, the material sets for the diodes examined are Ni-NiO-Nb_2O_3-CrAu and Ni-NiO-ZnO-CrAu. The tunneling mechanism of the MIIM diode is shown in Figure 1.2 for a diode under zero bias [26]. The tunneling distance is linearly dependent on the electron

voltage and the tunneling probability is exponentially proportional to the tunneling distance [21]. This effectively causes the necessary non-linear I(V) characteristics for a diode to rectify an AC current. With two insulators, the electron tunneling phenomena begins to favor one direction over the other, which provides the diode with asymmetric characteristics necessary for zero-bias operation under free-space radiation.

The three commonly used diode performance metrics to quantify the non-linearity and asymmetry of rectifying diodes are the zero-bias responsivity, zero-bias resistance and I(V) asymmetry [26]. The zero-bias responsivity is defined as one-half of the second derivative of the I(V) curve divided by the first derivative evaluated at a voltage of zero, while the zero-bias resistance is defined as the inverse of the first derivative of the I(V) curve again evaluated at zero voltage. The asymmetry can easily be seen in a plot of the differential resistance [16]. For a diode to operate as an energy harvester, it must have a non-zero zero-bias responsivity. If a diode does not have a non-zero zero-bias responsivity, it will require a bias voltage to operate, which precludes it from operating as an energy harvester because a voltage will be required to bias the diode to generate a response. The application of a bias voltage to the diode requires an energy input, greatly reducing the efficiency of the overall device. The resistance of the diode must be sufficiently low to couple with the low impedance of the antenna in the system [27]. In general, the larger the zero-bias responsivity of the diode, the larger the diode resistance will be. This creates a difficulty in finding the “Goldilocks zone”, where the resistance is not too high so that there is a substantial responsivity and good impedance matching to the antenna, or the resistance is too low such that the diode has zero responsivity [28]. From a fabrication standpoint, the insulator layers must be sufficiently thin such that the resistance is not too high, but thick enough to provide non-linear effects for the diode. Typical antenna impedances are on the order of hundreds of ohms, while many of the reported diodes have resistances on the order of 10 kΩ to

have a significant zero-bias responsivity [29, 30, 31]. Diodes with such a high zero-bias resistance are already going to be limited by the antenna resistance-capacitance (RC) coupling efficiency, or impedance matching, even before accounting for the capacitive losses of the diode. Thus, the fabrication goal for the rectenna diodes is < 1000 Ω, and > 1 A/W [32]. Even so, it is posited that the reason for such poorly performing high-frequency diodes is the RC coupling mismatch [16]. A recently published study reported an overall rectification efficiency of 1.75×10^{-14} [33].

1.5 Diode Characterization

In this section, the diode characterization techniques and various parameters of the diodes are explored. This includes the two-term exponential function, which is used to fit the experimental I(V) data of the diodes, and the physical parameters of the diode: resistance, responsivity, and capacitance. The role that each of these parameters play on the diode rectification is also discussed.

1.5.1 Two-Term Exponential Function

The diodes used in the rectenna are characterized by four-point probe DC measurements. The forward and backward DC I(V) characteristics provide insight to the diode. Currently, diode I(V) curves are fit to polynomial equations, often of high order [30, 32, 34, 35]. This has led to the fitting of diode I(V) curves with the two-term exponential function [36]. At a certain point, high order polynomial equations will incorporate any deviation to the data to create a "good" fit.

$$I(V) = a * e^{bV} + c * e^{-dV} = I_0 * \left(e^{bV} - e^{-dV}\right) \tag{1.5.1}$$

$$I_0 = \frac{a + c}{2} \tag{1.5.2}$$

In Equation (1.5.1), *a*, *b*, *c* and *d* are coefficients of the two-term exponential fit, *V* is the voltage across the diode and I_0 is the saturation current. When calculating I_0, it is made sure that *a* and *c*

are sufficiently close with a difference of 2% or less. The units for the coefficients are amperes for *a* and *c* and inverse volts for *b* and *d*. While the coefficients of the fit have no physical meaning, the second part of the equation demonstrates the relationship to an ideal Shockley diode, another motivation for the use of the two-term exponential for MIIM diode I(V) fitting. If *d* = 0, then the diode would behave as an ideal Shockley diode [37], whose I(V) behavior is given by Equation (1.5.3),

$$I(V) = I_S\left(e^{V_D/nV_T} - 1\right), \tag{1.5.3}$$

where I_s is the saturation current, V_D is the voltage across the diode, V_T is the thermal voltage and *n* is the Shockley ideality factor.

1.5.2 Resistance

As mentioned previously, the first performance metric for the diode is the differential resistance,

$$R_{diff} = \left[\frac{dI}{dV}\right]^{-1} = \frac{1}{I_0(be^{bV} + de^{-dV})} \tag{1.5.4}$$

At zero voltage bias, this gives the resistance of the device,

$$R_D = \frac{1}{I_0(b+d)}\ [\Omega]. \tag{1.5.5}$$

1.5.3 Responsivity

Another important performance metric is the small signal responsivity of the diode, which is a measure of the DC current out as a function of the AC power in. The small signal responsivity, given by Equation (1.5.6), is found by taking the Taylor expansion of the I(V) for a small AC signal which provides the diode response. The full derivation of the small signal responsivity is provided in Appendix I.I.

$$\beta_D = \frac{1}{2}\left[\frac{\frac{d^2I}{dV^2}}{\frac{dI}{dV}}\right] = \frac{1}{2}\frac{b^2e^{bV_D} - d^2e^{-dV_D}}{(be^{b*V_D} + de^{-dV_D})} \tag{1.5.6}$$

At zero voltage bias, the responsivity of the device is given by,

$$\beta_0 = \frac{1}{2}(b-d)\left[\frac{ampere}{watt}\right]. \tag{1.5.7}$$

The responsivity is an effective performance metric when the AC signal is sufficiently small because a DC current defined by the responsivity is found by taking the Taylor expansion around V = 0. Therefore, the response will depend on the AC signal non-linearly [38].

1.5.4 Asymmetry

The asymmetry of the diode, A_D, which is related to the responsivity, is a measure of the forward, *I(V)*, and reverse, *I(-V)*, currents in the diode,

$$A_D = \frac{I(V)}{I(-V)}. \tag{1.5.8}$$

1.5.5 Diode Capacitance

The diode capacitance plays a substantial role in the overall efficiency of a rectenna due to the RC impedance match between the diode and the antenna. The diode capacitance is estimated by modeling the capacitance as a parallel plate capacitor with NiO and Nb_2O_5 and NiO and ZnO as the dielectric materials with the estimated thickness and area of the fabricated diodes, respectively [39]. The frequency dependent dielectric constants of NiO, Nb_2O_5 and ZnO have been previously measured at the operating frequencies of these rectenna [40]. The diode capacitance for the niobium oxide diodes is estimated to be 3 fF and 1.5 fF for the ZnO diodes. Since the tested devices were fabricated under the same conditions, the antenna impedance and diode capacitance are assumed to be the same for each device that is tested. As will be shown, even

though the rectenna were fabricated under the same conditions at the same time, there is some variation in the diode resistance. Therefore, there is likely a variation in the diode capacitance as well. However, there is no method to measure the high frequency capacitance of each individual diode, rather the diode capacitance is estimated by the dielectric properties of the diode materials.

1.5.6 RC Coupling Efficiency

One of the largest challenges to high frequency rectenna operation is the antenna and diode impedance match or RC coupling efficiency given by the following equation [16]:

$$\eta_{RC} = \frac{\frac{4R_A R_D}{(R_A + R_D)^2}}{1 + \left(\frac{R_A R_D}{R_A + R_D}\omega C_D\right)^2}, \tag{1.5.9}$$

where R_A is the radiation impedance of the antenna, R_D is the diode resistance, C_D is the diode capacitance and ω is the operating frequency of the diode. The RC coupling efficiency is fully derived in Appendix I.II. For the purposes of calculating the RC coupling efficiency, the antenna impedance is estimated to be entirely real and approximately 100 Ω [38, 39].

At 1 THz and using our diode capacitance, the coupling efficiency is entirely a function of the diode resistance. For a perfectly matched diode to an antenna of 100 Ω, the impedance mismatch efficiency will approach unity with decreasing capacitance at 1 THz. The maximum impedance mismatch efficiency for a diode that has a resistance five times larger than the

antenna's impedance will approach 57% as the diode capacitance is reduced, as shown in Figure 1.3.

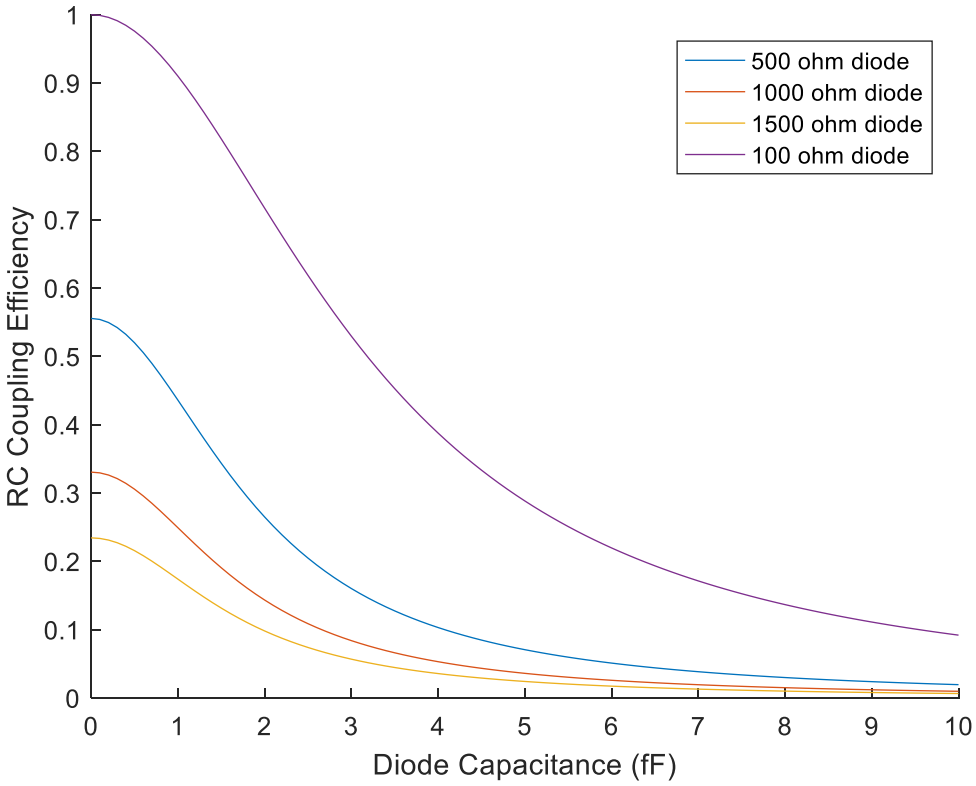

Figure 1.3: Antenna/diode RC coupling efficiency, Equation (1.5.9), as a function of diode capacitance. The antenna impedance is assumed to be 100 ohms and entirely real. The maximum efficiency is achieved for a perfectly matched diode with no capacitive losses. The diode resistances selected here are representative of the measured resistances of the diodes used in this study.

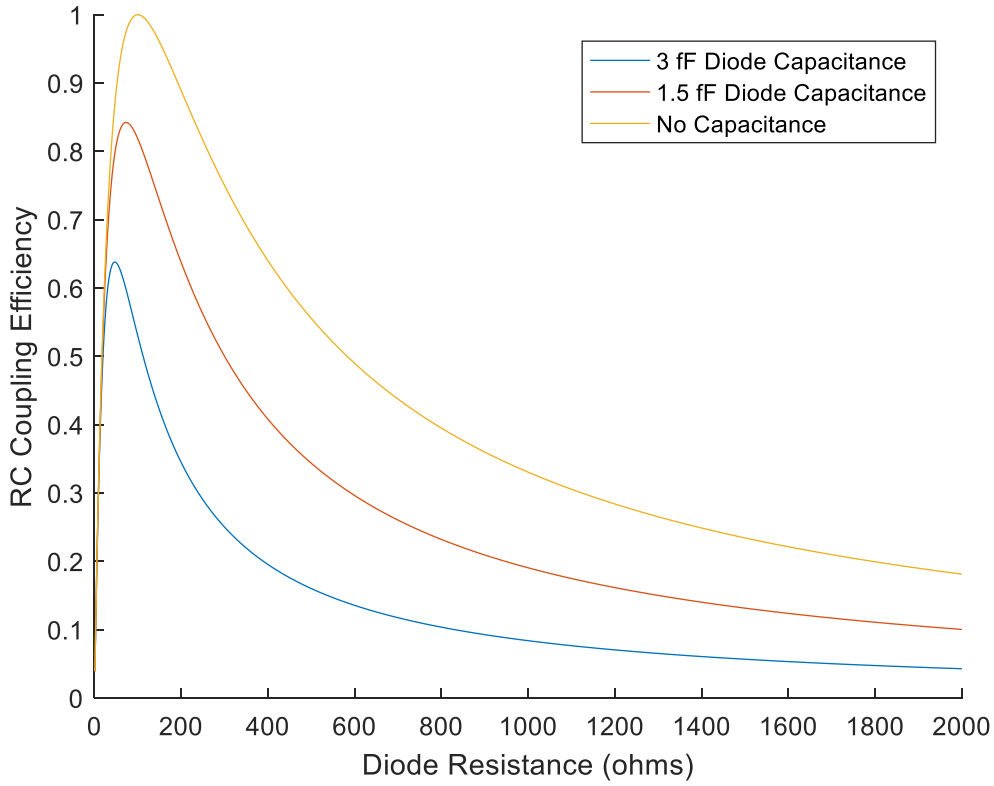

Figure 1.4: Antenna/diode RC coupling efficiency, Equation (1.5.9), as a function of diode resistance. The capacitances shown are representative of the diode capacitances based on the material sets reported in this study.

The capacitive losses from the diode capacitance alone decrease the operating efficiency of the rectenna significantly. For the estimated capacitance of the niobium oxide, Nb_2O_5, diodes, the impedance mismatch efficiency at approximately 20% for a 500-ohm device matched to a 100-ohm antenna, depicted in Figure 1.4. For a 1500-ohm device, the mismatch efficiency is 15% using the capacitance of the zinc oxide, ZnO, diodes. The resistances are chosen here to represent the measured DC resistances of the diodes. By reducing the effective capacitance of the diode, the impedance mismatch efficiency can be maximized.

1.6 Additional Experiment Support for Two-Term Exponential Fit

While most of the evidence and support for the two-term exponential fit as a superior fit has been provided by Pelz et al, [36], a small experiment was performed to provide a stronger basis for the use of the two-term exponential fit.

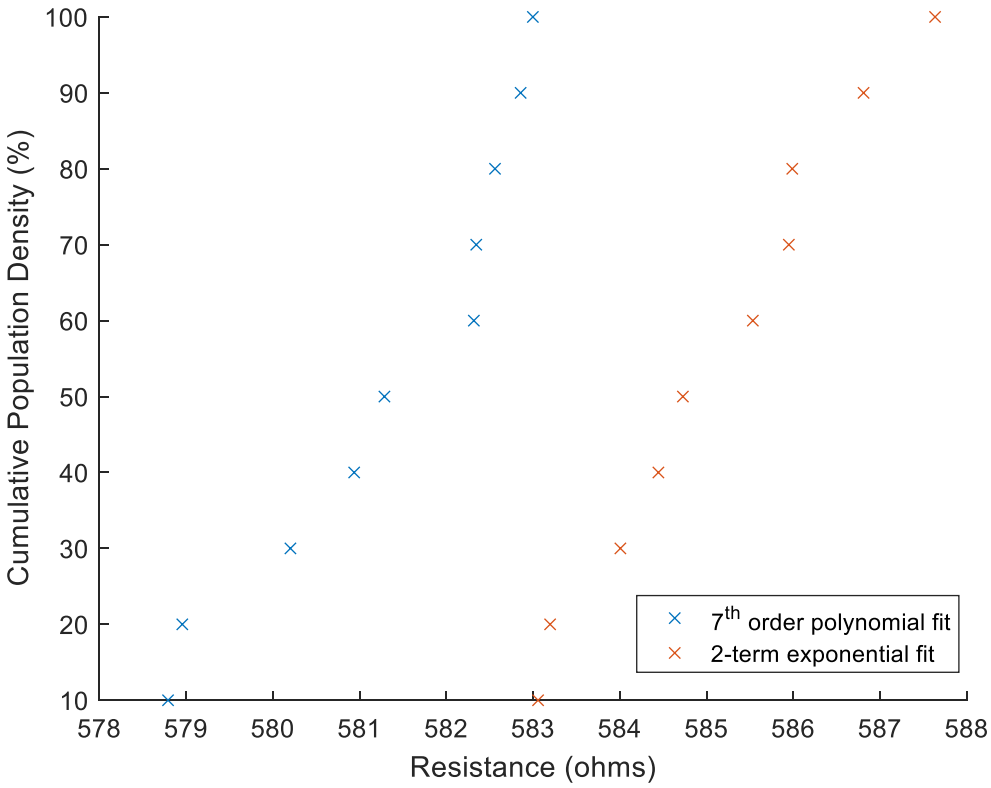

Figure 1.5: Resistance probability plot of two-term exponential and 7th order polynomial fits of repeated experimental I(V) measurements of the same device demonstrating the reproducibility of the instrumentation and the fitting procedure for the two different diode fits.

A single device was measured ten times and fit to a two-term exponential and 7th order polynomial, as is current practice. Between each four-point probe measurement, the probes were completely lifted off the test pads and the process of testing the diode was completely cycled. Figure 1.5 and Figure 1.6 are the probability plots of the resistance and responsivity calculated from the fits of the I(V) data for these repeated measurements, respectively. While the resistance for each fit only varies three to four ohms for each measurement, the clear benefit of the two-

term exponential fit over the 7th order polynomial is the consistency with which the responsivity is measured. The near-vertical line for the two-term exponential responsivity in Figure 1.6 demonstrates consistent measurements of the device's responsivity, while the 7th order polynomial fit is more sensitive to the instrumentation and data that are collected. Reproducing results for the I(V) data is crucial to utilizing the appropriate information when determining the diode rectification capability. The evidence collected supports the use of the two-term exponential function that has been suggested to use in place of the 7th order polynomial fit [36].

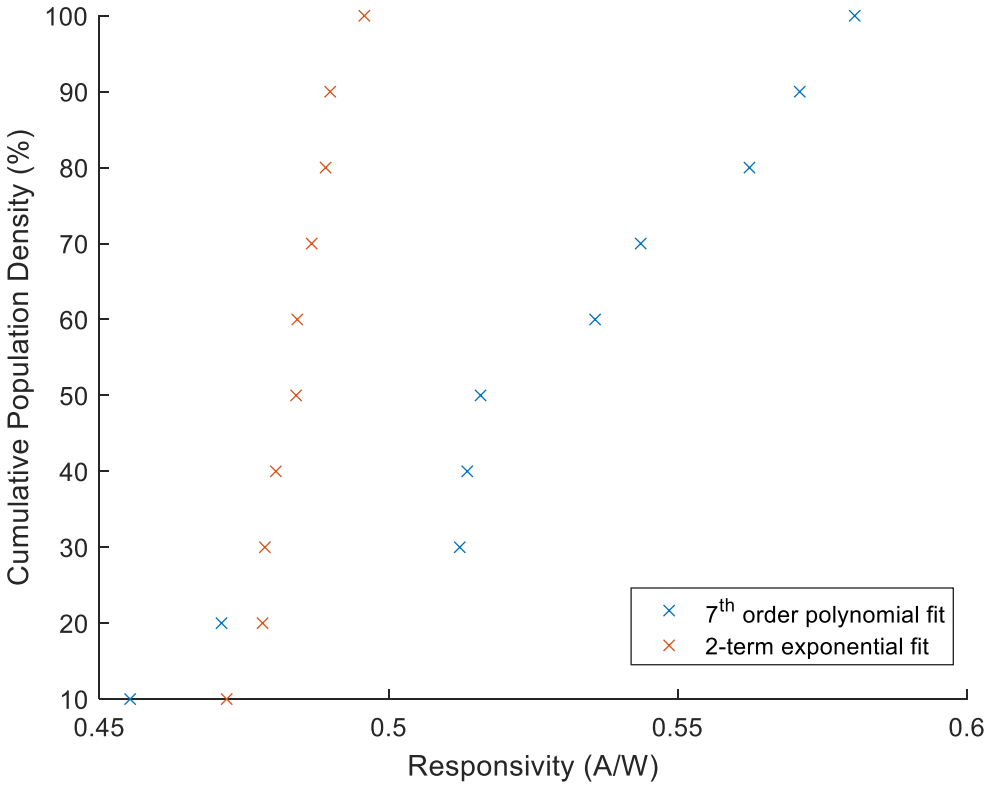

Figure 1.6: Responsivity probability plot of two-term exponential and 7th order polynomial fits of repeated experimental I(V) measurements of same device demonstrating the reproducibility of the instrumentation and the fitting procedure for the two different diode fits.

Chapter 2 MATLAB and Simulink: Understanding and Modeling Diodes

In this chapter, the focus will be on diode modeling and simulation. Simulations are performed utilizing MATLAB and Simulink. Further evolution of the two-term exponential results in the development of an analytical equation that is compared to the Simulink model. This analytical model has multiple uses: primarily a quick and easy calculator for the optimal load resistance for power extraction and a "large" signal responsivity, where the previous small signal responsivity, β_0, fails to correctly calculate DC current for a given AC power due to its limitations. Then, justification for the need of a new figure of merit, based on the Shockley diode equation, is presented and discussed.

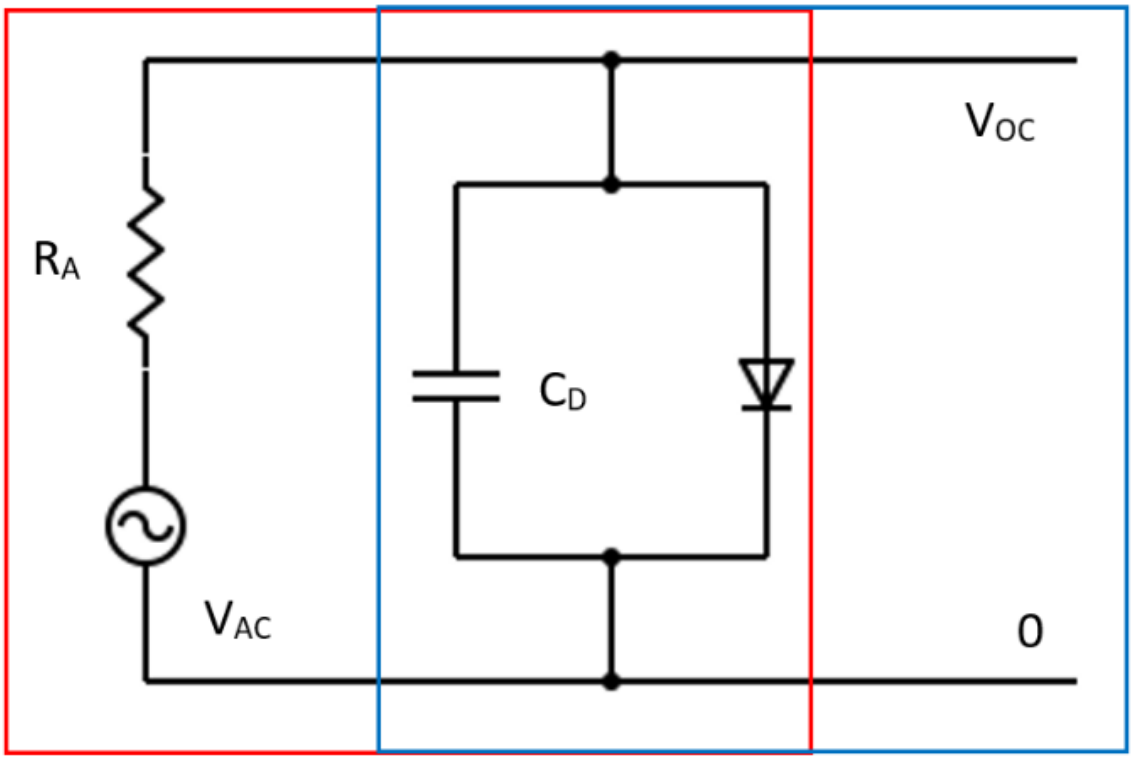

Figure 2.1: A simplified rectenna circuit used for modelling the system is presented with the AC portion shown in red and the DC portion shown in blue.

2.1 MATLAB and Simulink Model

Using MATLAB and Simulink, we simulated the rectenna system can be simulated to estimate the DC voltage or power that can be extracted [41]. The simplified circuit, shown in Figure 2.1 represents the modeled, as well as, the experimentally measured system. The rectenna can be modeled as an overlap of two circuits: AC, shown in red, and DC, shown in blue. The AC portion of the circuit consists of the antenna, AC voltage source and the diode, which also contains the diode capacitance in parallel. The DC portion of the circuit contains the diode and the DC load resistor or open circuit if the load resistance is infinite. In the experimental setup, an open circuit voltage is measured. However, in the Simulink model, a load resistance of 10 MΩ is used to represent the open circuit voltage that is measured. Simulink can be used to understand the relationship between the AC circuit and the DC circuit.

2.1.1 Simulink Model Set-up

The diode in the Simulink system is a MATLAB function defined by the two-term exponential equation that is measured from the DC I(V) of the diode. The Simulink circuit also consists of a blocking capacitor on the AC portion of the circuit to prevent any DC voltage from affecting the AC side of the circuit. A load inductor and capacitor that help the model reach steady state in a reasonable time are used on the DC portion of the circuit with the load resistance. One of the caveats of using the Simulink model is the time it takes in which to model a large volume of diodes for data processing. When performing the Simulink model, an AC voltage source is provided with a frequency of 1 THz and a peak amplitude. The AC voltage input into the circuit is in series with the antenna resistor. The system is run until it reaches steady-state, where the output power is calculated by the product of the root-mean square voltage and root-mean square current across the load resistor. For the modeling presented here, ideal diodes with a resistance of 1000 Ω and responsivity of 1 A/W were chosen. These values were chosen fabrication targets

due to the low resistance and high responsivity [32]. Reasonable values for I_0 that matched experimentally measured values (See Figure 4.1 and Figure 4.2) were used to set the basis for the diode equations used in the model. These parameters for ideal diodes were chosen because of fabrication limits on the diode that tend to restrict low resistance diodes to a low responsivity.

2.1.2 Load Resistance

For power extraction from the diode, the optimum load resistance of the diode depends on the input AC power and diode resistance. Figure 2.2 and Figure 2.3 demonstrate the relationship between maximum output power and the load resistance for two different AC voltages for four different diodes, the characteristics of which are listed in Table 2.1. At low input voltages, the optimal load resistance matches the resistance of the diode. As the input voltage increases, the optimal load resistance decreases for a given diode. Figure 2.2 and Figure 2.3 demonstrate where the peak resistance for each of these diodes is as the input voltage, V_{AC}, is doubled from 200 mV to 400 mV. In Figure 2.2, the lower input AC voltage study, Diode 2 and Diode 3 have peak powers when the load resistance matches their respective diode resistances, approximately 1000 Ω each. However, when the input AC voltage is doubled, the peak output power occurs when the load resistance is significantly lower than their respective diode resistances, near 500 Ω. Diode 1, with a R_D nearly 10× that of Diode 3, provides a good indicator for the effect the diode resistance has on the optimal load resistance for power extraction, as shown in Figure 2.2 and Figure 2.3. The lower resistance diodes have a peak power output when the load resistance is matches the diode resistance. While for the higher resistance diode, the low load resistances are not where the maximum power output is achieved. When designing a system for power extraction, it is crucial to know the optimized load resistance.

Table 2.1: Diode I(V) characteristics for the diodes used in Simulink model for optimizing load resistance demonstrating how the load resistance changes for optimal power extraction.

	Resistance (Ω)	Responsivity (A/W)
Diode 1	10398	0.77
Diode 2	1316	0.48
Diode 3	1042	0.41
Diode 4	1032	0.12

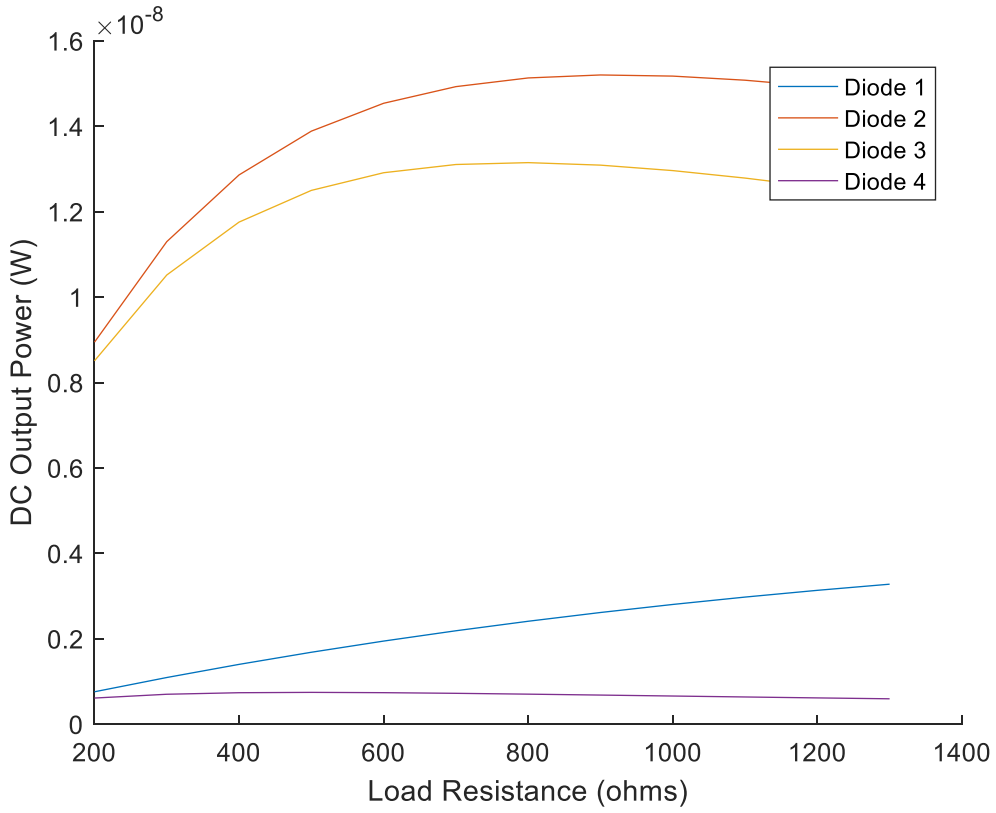

Figure 2.2: Load resistance for various real diodes, given in Table 2.1, at 200 mV AC input, when shown in conjunction with Figure 2.3 demonstrates how the optimal load resistance decreases with increasing V_{AC}.

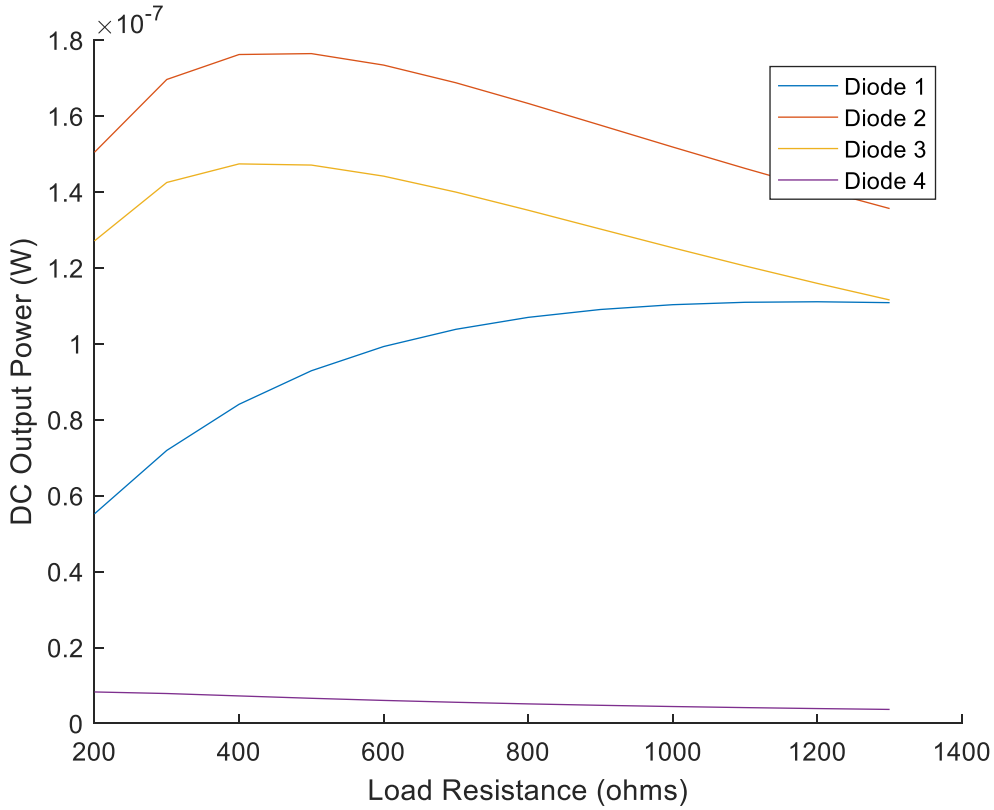

Figure 2.3: Load resistance for various real diodes, given in Table 2.1, at 400 mV AC input, when shown in conjunction with Figure 2.2 demonstrates the how the optimal load resistance decreases with increasing V_{AC}.

2.2 Analytical Model

Mathematically, the DC output voltage of a rectenna with a given input AC voltage and load resistance can be modeled and compared to the simulation performed by the Simulink/MATLAB model. This model can be used to shorten the time necessary to simulate a given diode. Additionally, this analytical model can be used to calculate the appropriate load resistance for optimum power extraction and replace the small signal responsivity when necessary. The analytical model does not account for diode capacitance, as the Simulink model can, but when using it to replace the small signal responsivity, the capacitance is accounted for in the RC coupling efficiency, Equation (1.5.9).

2.2.1 Derivation of Analytical Model

The voltage across the diode can be broken into two components, the AC sine wave input and the DC output [42],

$$V = V_{AC} \sin \omega t - V_{DC}. \tag{2.2.1}$$

If we start with the two-term exponential function of the diode and replacing the voltage with the voltage defined in Equation (2.2.1), the current through the diode is now a function of voltage, *V*, and time, *t*, shown in Equation (2.2.2). The time dependent current is averaging the AC signal over one cycle, $2\pi/\omega$, resulting in the average current in the diode, Equation (2.2.3).

$$I(V,t) = I_0\left(e^{bV} - e^{dV}\right) = I_0\left(e^{b(V_{AC}\sin\omega t - V_{DC})} - e^{-d(V_{AC}\sin\omega t - V_{DC})}\right) \tag{2.2.2}$$

$$\langle I \rangle = \frac{V_{DC}}{R_{Load}} = \frac{\omega}{2\pi}\int_0^{2\pi/\omega} I(V,t)dt = I_0[e^{-bV_{DC}}J_0(bV_{AC}) - e^{-dV_{DC}}J_0(dV_{AC})] \tag{2.2.3}$$

In Equation (2.2.3), the average current in the diode is a function of the DC diode characteristics and the input AC voltage, V_{AC}. $J_0(bV_{AC})$ and $J_0(dV_{AC})$ are modified Bessel functions of the first kind. Since the voltage across the diode is small and near zero, a Taylor expansion centered around V_{DC} equal to zero will approximate the diode voltage. Any terms after the first order are subsequently ignored for the development of this equation. Although omitted here, second order terms may be utilized by solving for V_{DC} using the quadratic equation.

$$\frac{V_{DC}}{R_{Load}} = I_0[J_0(bV_{AC}) - J_0(dV_{AC}) + V_{DC}\,[dJ_0(dV_{AC}) - bJ_0(bV_{AC})]\,] \tag{2.2.4}$$

$$V_{DC} = \frac{J_0(bV_{AC}) - J_0(dV_{AC})}{\frac{1}{R_{Load}I_0} + bJ_0(bV_{AC}) - dJ_0(dV_{AC})} \tag{2.2.5}$$

Since the modified Bessel functions of the first kind here are constant, this provides a simple equation to determine the output voltage that only depends on the AC input voltage, DC diode

characteristics and load resistance. For an open circuit, the voltage can be approximated using the equation,

$$V_{OC} = \frac{\ln\left[\frac{J_0(bV_{AC})}{J_0(dV_{AC})}\right]}{b-d}. \tag{2.2.6}$$

2.2.2 Optimization of Load Resistance

When modeling and designing this system for the optimal power extraction, it can be useful to know what the desired load resistance should be. Equation (2.2.5) can be used to easily and efficiently determine the optimum R_{load}. The maximum power for a given diode and input voltage can be determined using Equation (2.2.5) in Equation (2.2.7), where

$$P_{DC} \propto \frac{V_D}{R_{Load}}. \tag{2.2.7}$$

2.2.3 "Large" Signal Responsivity

The analytical model, Equation (2.2.5), can be used where the small signal responsivity does not suffice. The small signal responsivity, β_0, can be used to approximate the output DC power for small AC voltages, as will be the case for the terahertz radiation to be examined later, but as the AC voltage increases, the small signal responsivity becomes insufficient to approximate the DC output power. At higher (> 10 mV) AC voltage, the responsivity enters the non-linear region of its relationship to the DC power. For example, Diode 1, $I_0 = 5 \times 10^{-5}$ A, is compared using the Simulink model and the small signal responsivity to determine the DC output power, shown in Figure 2.4, where the load resistance is optimized for maximum power extraction. The small signal responsivity begins to deviate from the Simulink model around 10 mV for this example diode.

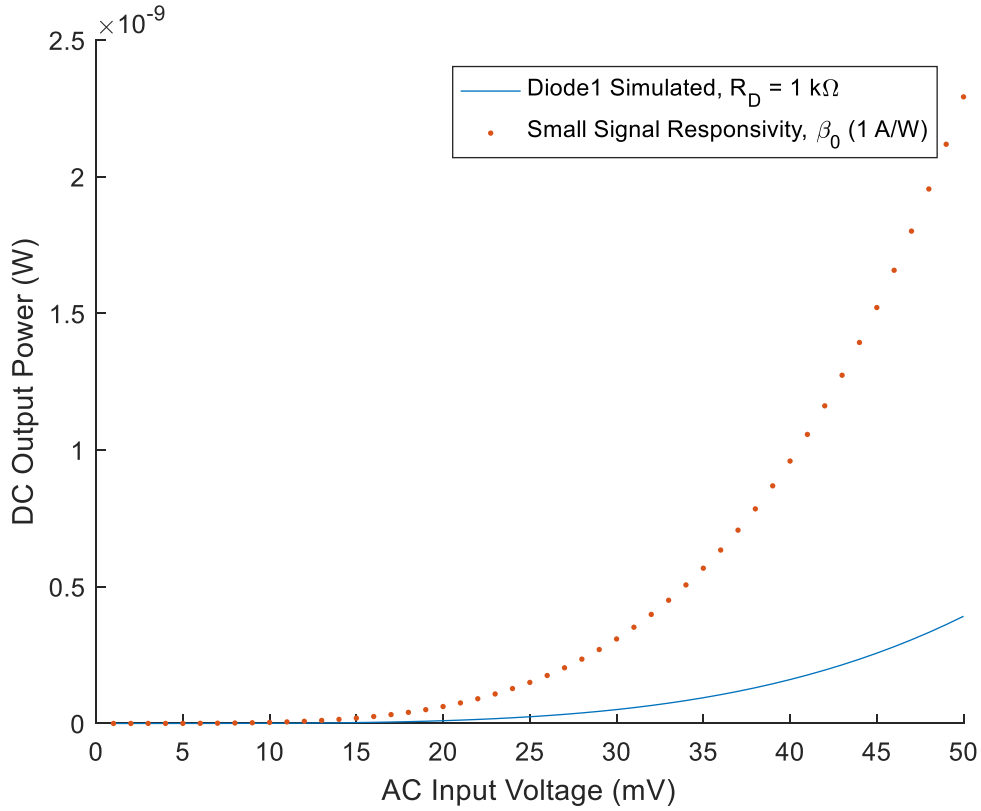

Figure 2.4: The deviation of the small signal responsivity, β_0, compared to the Simulink model for Diode 1, $I_0 = 5 \times 10^{-5}$ A. The small signal responsivity begins to deviate from the simulation results at low input AC voltages, < 10 mV. The small signal responsivity, however, it adequate for the AC input voltages reported in this work for the AC to DC rectification using MIIM rectenna.

Considering multiple diodes could have the same responsivity but different rectification results from Simulink, it becomes clear that the small signal responsivity is only adequate for use at low input AC voltages. The analytical model can be referred to as a non-linear or "large" signal responsivity equation to replace the small signal responsivity. At extremely high input voltages, the Simulink model would still be required, but the MIIM diodes examined in this study experience a dielectric breakdown when the AC voltage approaches 1 V.

2.2.4 Comparison of Analytical Model to Simulink Model

From Equation (2.2.5) it is obvious that the DC voltage is dependent on three inputs: the AC input voltage, the load resistance and the diode DC characteristics.

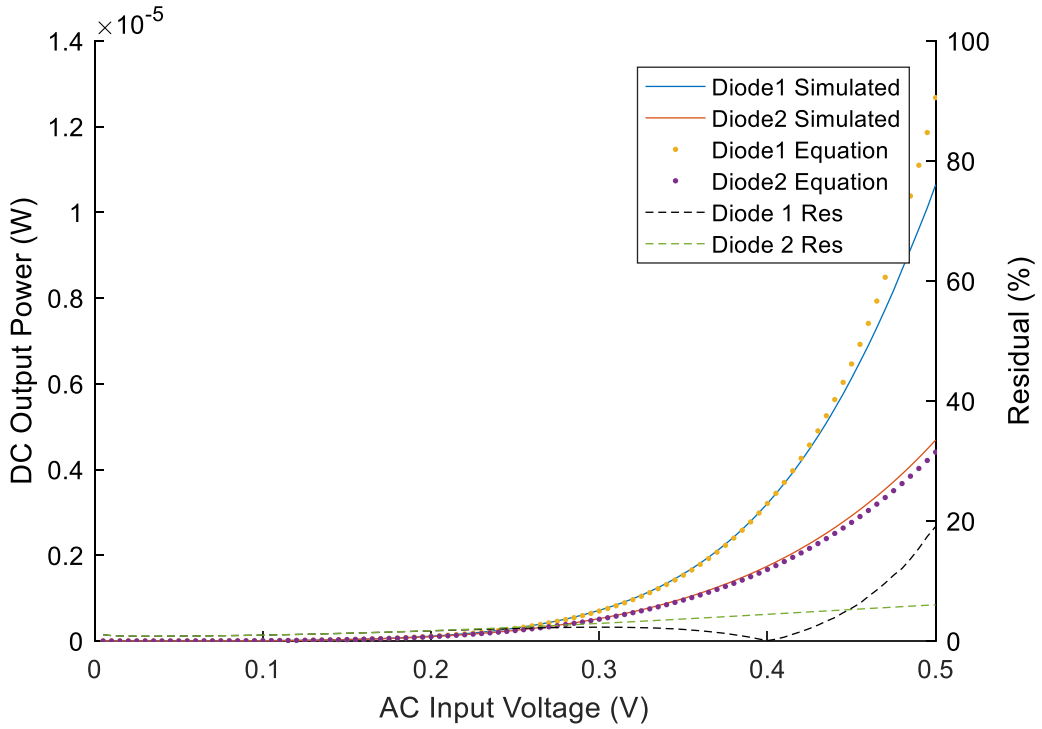

Figure 2.5: Comparison of mathematical model to the Simulink model for two 1 kΩ and 1 A/W diodes when both are optimized for the maximum power output by changing the load resistance. Diode 1 has an $I_0 = 5 \times 10^{-5}$ A and Diode 2 has an $I_0 = 1 \times 10^{-4}$ A. Values for I_0 were chosen to be representative of measured diodes. The right y-axis shows the residue, or difference, between the mathematical model and the Simulink model.

Equation (2.2.5) was compared to the results of the Simulink model for two "ideal" diodes with an I_0 of 5×10^{-5} A and 1×10^{-4} A, respectively. The chosen values for I_0 are on the order of experimentally measured diodes (See Figure 4.1 and Figure 4.2). Figure 2.5 plots the results of the comparison study between the Simulink model and the analytical model. As the AC voltage increased, the optimal load resistance was changed for each diode to extract the maximum value for the DC power.

2.2.5 Breakdown

Figure 2.5 demonstrates the strong correlation between the simulation and the mathematical model up to 500 mV. For Diode 1, the breakdown at 400 mV occurs when the dominant term in the denominator changes. The diode equation breaks down when the load resistance term becomes the dominant term and the equation begins to over-predict the Simulink model. For Diode 2, the breakdown occurs around 800 mV. For a third diode with $I_0 = 1.5 \times 10^{-4}$ A, or three times the I_0 of Diode 1, the breakdown occurs at around 1.2 V. In general, the diodes studied have $I_0 < 1.5 \times 10^{-4}$ A. The diodes fabricated in this study experience dielectric breakdown if biased with a voltage > 1 V. If load resistance is not optimized for each diode and input voltage, the mathematical model holds throughout the AC voltage regime necessary for the study of these MIIM diodes.

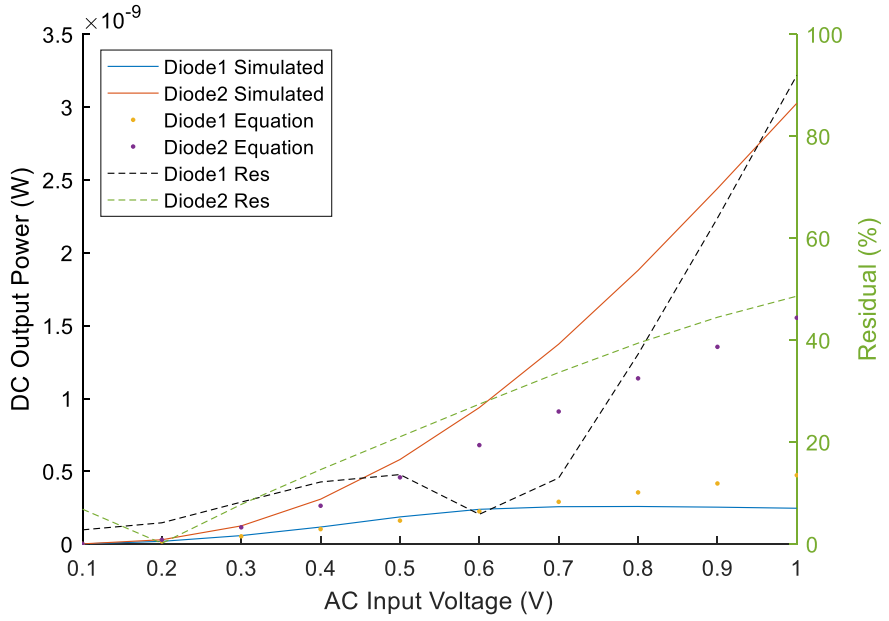

Figure 2.6: Comparison of mathematical model to the Simulink model for two 1 kΩ and 1 A/W diodes with the load resistance set to 10 MΩ. Diode 1 has an $I_0 = 5 \times 10^{-5}$ A and Diode 2 has an $I_0 = 1 \times 10^{-4}$ A. Values for I_0 were chosen to be representative of measured diodes. The right y-axis shows the residue, or difference, between the mathematical model and the Simulink model.

Figure 2.6 demonstrates the relationship between the analytical model and the Simulink model when the system is not optimized for maximum power extraction with the load resistance. Instead, the load resistance is 10 MΩ. The same diodes are compared as before, but the analytical model breaks down at lower voltages than the previous setup. The difference between the analytical model and the Simulink model stays below 20 % up to about 400 mV V_{AC} input. The input AC voltages the diodes in this study experience is significantly lower than 400 mV; thus, the analytical model can be used in place of the small signal responsivity in this case. Figure 2.5 and Figure 2.6 present the need to explore and define "design" rules for the analytical model based on the diode and load resistance.

The analytical model can be used to quickly and efficiently predict the output DC power for a given rectenna system. However, further validation of the high AC voltage breakdown of the mathematical model should be explored, including the development of "design" rules for when the analytical model deviates from the Simulink model. Additionally, Equation (2.2.5) can be used to approximate the ideal load resistance for a system or as a replacement for the small signal responsivity as the AC voltage to the diode increases.

2.3 New Figure of Merit based on Exponential Fit for MIM diodes

For a rectifying diode, three performance metrics are commonly used to characterize the diode: diode resistance, zero-bias responsivity, and asymmetry [26]. The asymmetry, A_D, of the diode is directly related to the responsivity [36]. For example, the two "fake" diodes previously used have a responsivity equal to 1 A/W, according to the two-term exponential equation. The asymmetry for Diode 1, $I_0 = 5 \times 10^{-5}$ A, would be 1.22 at a voltage of ± 0.1 V. At that same voltage, ± 0.1 V, Diode 2, $I_0 = 1 \times 10^{-4}$ A, would also have an asymmetry of 1.22. This could be done for any diode that has the same responsivity according to the two-term exponential equation with any

resistance. The asymmetry is purely dependent of the diode responsivity. That leaves reasonably two figures of merit for a diode based on three coefficients determined from the exponential fit of the I(V) data. Again, an exponential fit for diodes is convenient because it is easily related to the Shockley equation for ideal diodes, Equation (1.5.3). Therefore, for a given resistance and responsivity, a diode could have drastically different zero-bias rectifying abilities but only one defined asymmetry. It may be useful to define another figure of merit to truly quantify the quality of a diode's zero-bias rectification ability.

2.3.1 Figure of Merit Definition

The diodes are characterized using four-point probe DC measurements fit to a two-term exponential [36], Equation (1.5.1). As described in Chapter 1, if *d* = 0 in the exponential fit, the diode would be an ideal Shockley diode, obeying Equation (1.5.3) [36]. Hence, it is convenient to define the proposed figure of merit with respect to the Shockley diode,

$$F.O.M = \begin{cases} 1 - \dfrac{d}{b} \; if \; [|b| > |d|] \\ 1 - \dfrac{b}{d} \; if \; [|b| < |d|] \end{cases}. \tag{2.3.1}$$

In Equation (2.3.1), the smaller of the two exponential coefficients *b* and *d* is the numerator in the fraction such that the figure of merit always ranges from 0 to 1. It becomes clear that when *d* = 0, the figure of merit is 1 and is adherent to the Shockley diode equation. While when *b* = -*d*, the figure of merit is 0 and the diode will not rectify AC to DC at zero bias. In this case, the diode is symmetric and will have a zero zero-bias responsivity, but any diode with asymmetry can be defined on this scale. Thus, for this figure of merit, a diode that is fit to the two-term exponential function can be quantified by the quality of its adherence to the Shockley diode equation and its zero-bias rectification ability on a scale of 0 to 1. The adherence to the Shockley diode equation is not to be confused with the ideality, *n*, in the Shockley diode equation. The definition of

asymmetry, Equation (1.4.8), is useful for demonstrating the ratio of the forward and reverse currents in the diode. However, as shown previously, for a given diode resistance and responsivity, the asymmetry will always be the same for any voltage bias point. Therefore, it is a function of only the diode responsivity.

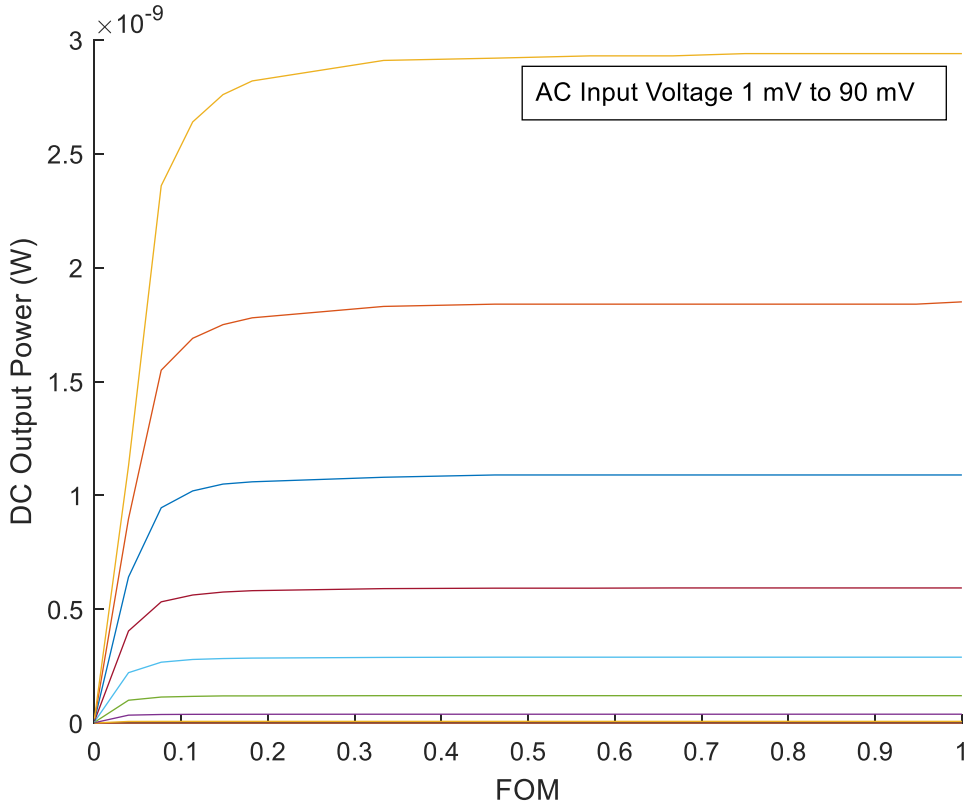

Figure 2.7: Proposed figure of merit for low AC input voltages, < 100 mV where it is evident that a F.O.M. > 0.1 will approach the maximum output power for a given V_{AC}.

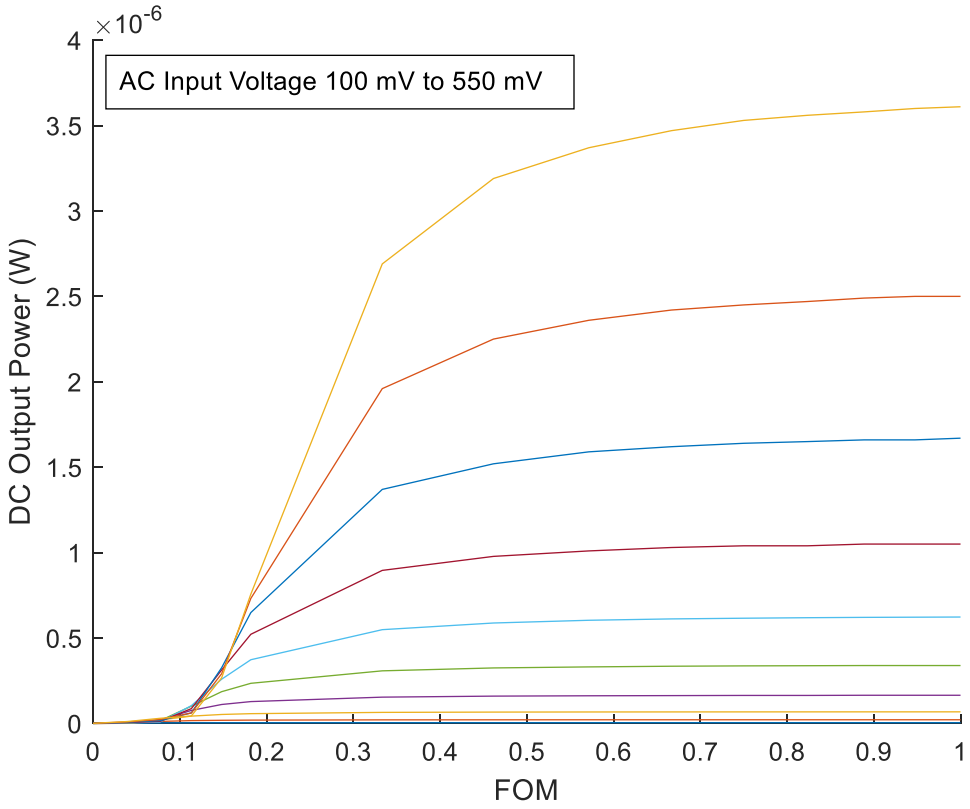

Figure 2.8: Proposed figure of merit for high AC input voltages, > 100 mV, where the necessity for a third figure of merit for two-term exponential diodes can be demonstrated for F.O.M.s up to 0.6.

As shown in Figure 2.7 and Figure 2.8, a diode with the same resistance and responsivity can have drastically different output voltages, depending on the coefficients from the exponential fit, but the asymmetry at any point, if measured with the traditional method, will remain exactly the same. To test the figure of merit for exponential fits of MIIM diodes, diodes with the same resistance, 1000 Ω, and responsivity, 1 A/W, were simulated over a range of input voltages. Each of the diodes had a different F.O.M. value ranging from 0 to 1. Figure 2.7 demonstrates the results for voltages ranging from 0 to 90 mV AC while Figure 2.8 demonstrates the results for voltages greater than 100 mV. While for AC voltages less than 100 mV, the figure of merit will not be a factor for FOMs greater than 0.1. For higher input AC voltages, however, the F.O.M. is necessary to determine the rectification quality of a diode. Figure 2.8 shows that for AC voltages greater

than 200 mV, the DC power could be affected by as much as an order of magnitude for an F.O.M. of 0.1 or greater.

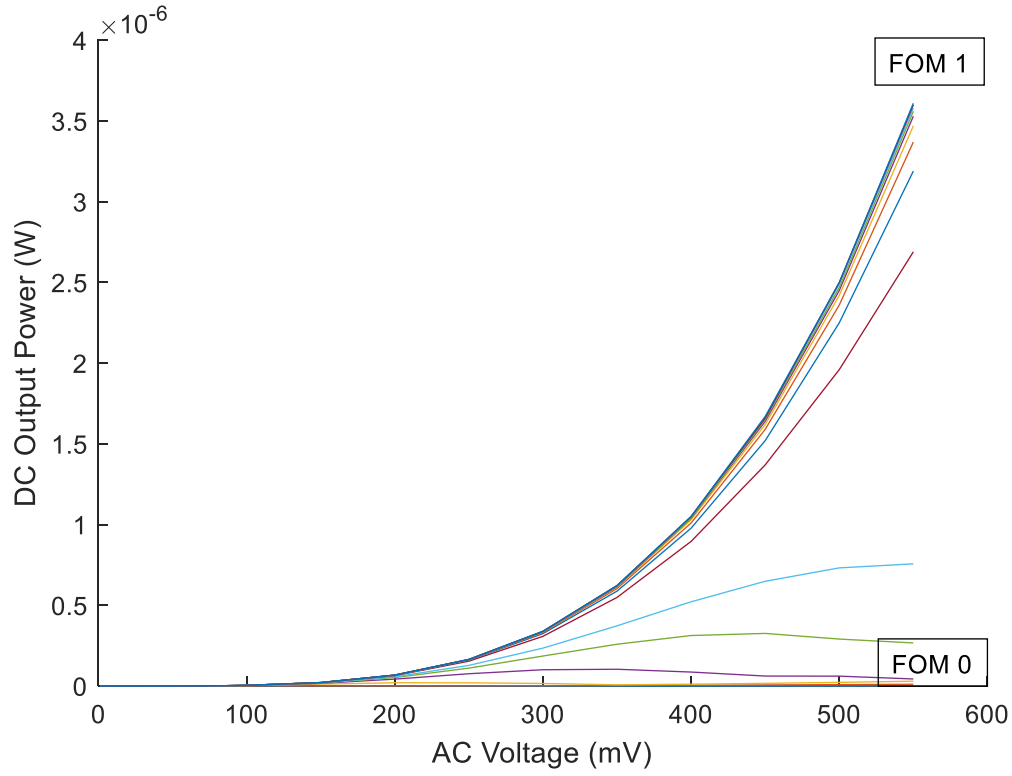

Figure 2.9: DC output power for 1 kΩ, 1 A/W device with range of F.O.M. values from 0 to 1 showing how the output power depends on the figure of merit for higher V_{AC} for a diode with the same resistance and responsivity.

2.3.2 Figure of Merit Conclusions

A figure of merit for two-term exponential fits for diodes in zero-bias rectenna circuits. For the diodes measured in this study, a typical figure of merit is around 0.1, putting it in a region where the diodes behave linearly with respect to the AC input voltage due to the low power of the terahertz source. The exponential coefficients likely depend on the material properties and fabrication techniques of the diodes. Unfortunately, due to the low power of the terahertz source used and the low F.O.M. of the diodes measured, experimental validation of this figure of merit is not available. Additionally, it is rare that two fabricated diodes of the same materials will have

identical resistance and responsivity and different F.O.M.s. To justify this F.O.M., diodes of differing material sets providing a range of values for the resistance, responsivity and figure of merit should be experimentally tested. Only evidence based on the simulation suggests the effectiveness of this figure of merit, while objective evidence suggests that the asymmetry figure of merit does not adequately provide a third value for diodes characterized by the two-term exponential fit. A higher power source to sufficiently probe the rectenna with higher AC voltages is also necessary to confirm the figure of merit.

2.4 Conclusions

An analytical model is presented to approximate the diode performance based on the two-term exponential fit for MIIM diodes. The analytical model agreed with the results of the Simulink model for AC input voltages ranging from 10 mV to 500 mV, depending on the DC diode characteristics and load resistance. While the small signal responsivity is sufficient at the low voltages and the Simulink model should be utilized for high voltages, the analytical model can be utilized as a “large” signal responsivity in the intermediate AC voltage range. A figure of merit is presented for two-term exponential fits of diode I(V) data. The figure of merit scales the diode zero-bias rectification ability from 0 for symmetric diodes to 1 for a Shockley diode and provides third performance metric for diodes that fit the two-term exponential equation.

Chapter 3 Terahertz Radiation Generation, Detection and Power

This chapter covers the terahertz generation that is used in the AC to DC rectification study of the diodes in Chapter 4. The primary motivation for much of the work in this chapter is to determine the power spectrum that is available to the diode for rectification. If the power spectrum is determined, the integration of that power spectrum of the antenna bandwidth will provide the amount of power into the antenna. In this chapter, the power spectrum is measured and compared to a power spectrum that is derived from the Fourier frequency spectrum measured by the THz-TDS system. Two methods of using the THz-TDS Fourier frequency spectrum to estimate the power the power meter measures are used to confirm the shape of the THz power spectrum greater 1 THz.

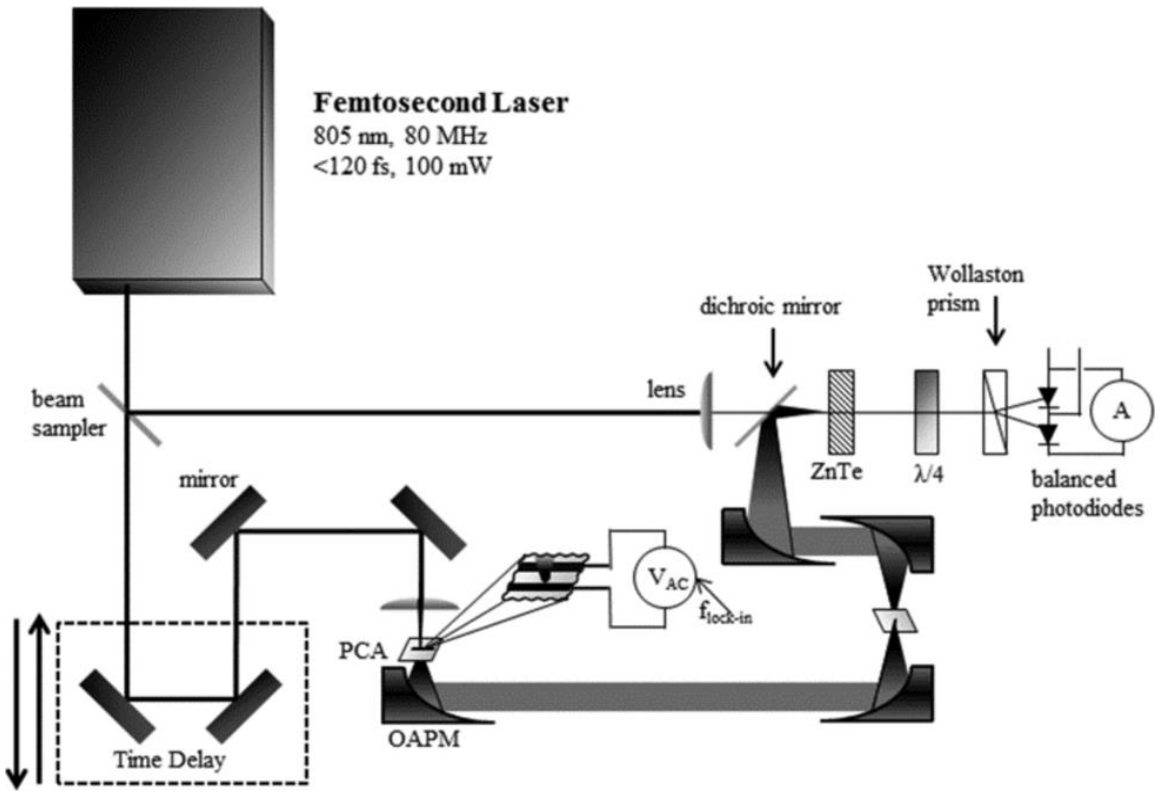

Figure 3.1: THz-TDS setup for the generation and detection of terahertz radiation with the location of the rectification and power meter placed at the focal point of the terahertz radiation and the bandpass filters placed in the collimated portion [40].

3.1 Terahertz Time-Domain Spectroscopy

The terahertz pulse was generated and detected from a standard terahertz time-domain spectroscopic (THz-TDS) set-up, shown in Figure 3.1. This THz-TDS system contains an erbium-doped Raman-shifted fiber laser (IMRA Femtolite FX-100) which operates at a central wavelength of 805 nm. The laser produces ≤ 120 fs free-space pulses with a repetition rate of 80 MHz and an average power of 100 mW. The beam is split into two portions: the probe beam and the pump beam. The primary portion of the beam is used to generate the terahertz pulse where it is focused on the terahertz emitter. The emitter is a photo-conductive antenna (PCA) with a LT-GaAs photoconductive substrate. As the pump beam is incident on the PCA, it is biased with 175 V.

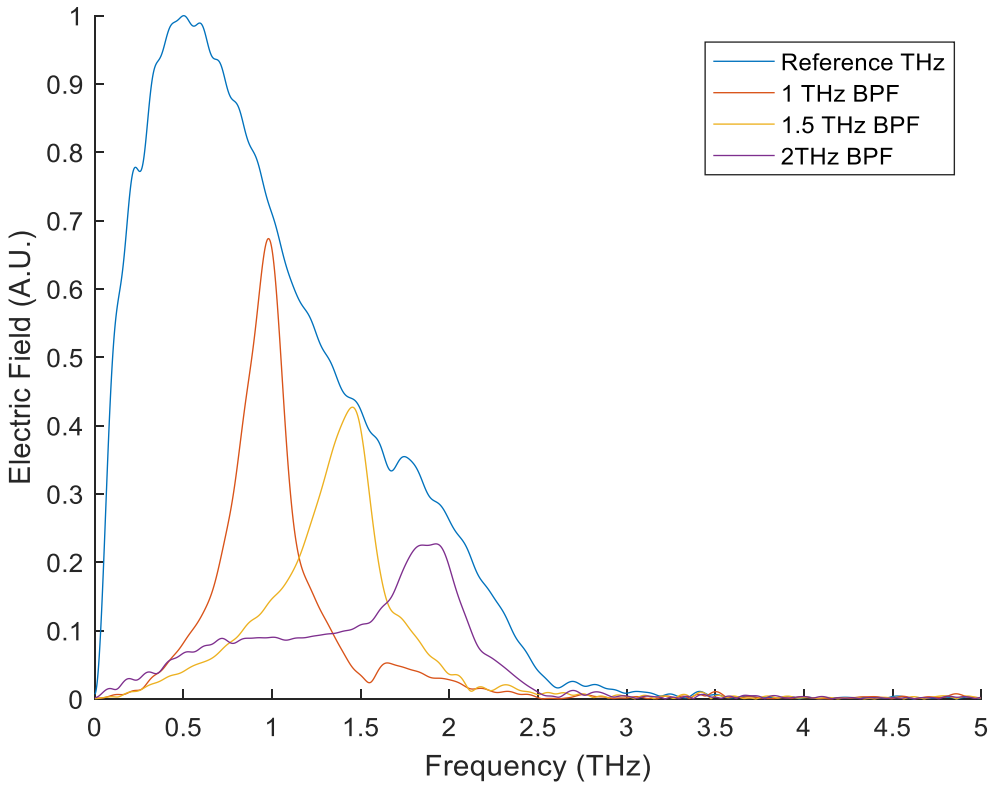

Figure 3.2: Normalized Fourier frequency spectrum of the measure THz-TDS reference, 1 THz BPF, 1.5 THz BPF and 2 THz BPF demonstrating the detectable frequency spectrum of the THz-TDS system.

The PCA then emits a terahertz beam that propagates until it is focused onto the non-linear crystal. The crystal used is 2 mm thick <110> ZnTe. In the non-linear crystal, the terahertz pulse propagates collinearly with the pump pulse, which has passed through a double-pass time delay. As the collinear beams pass through the crystal, the polarization of the probe beam is shifted proportionally to the electric field strength of the terahertz pulse, a technique called electro-optic sampling [43]. Using a Wollaston prism to split the probe beam into two orthogonally polarized portions, the relative change in polarization of the probe beam can be detected by two photodiodes. The difference in voltage of the photodiodes is measured by the lock-in amplifier with a time-constant of 3 s and a repetition rate of 5001 Hz. The double-pass time delay is scanned in 5 µm steps, thus giving a time-domain resolution of 33 fs.

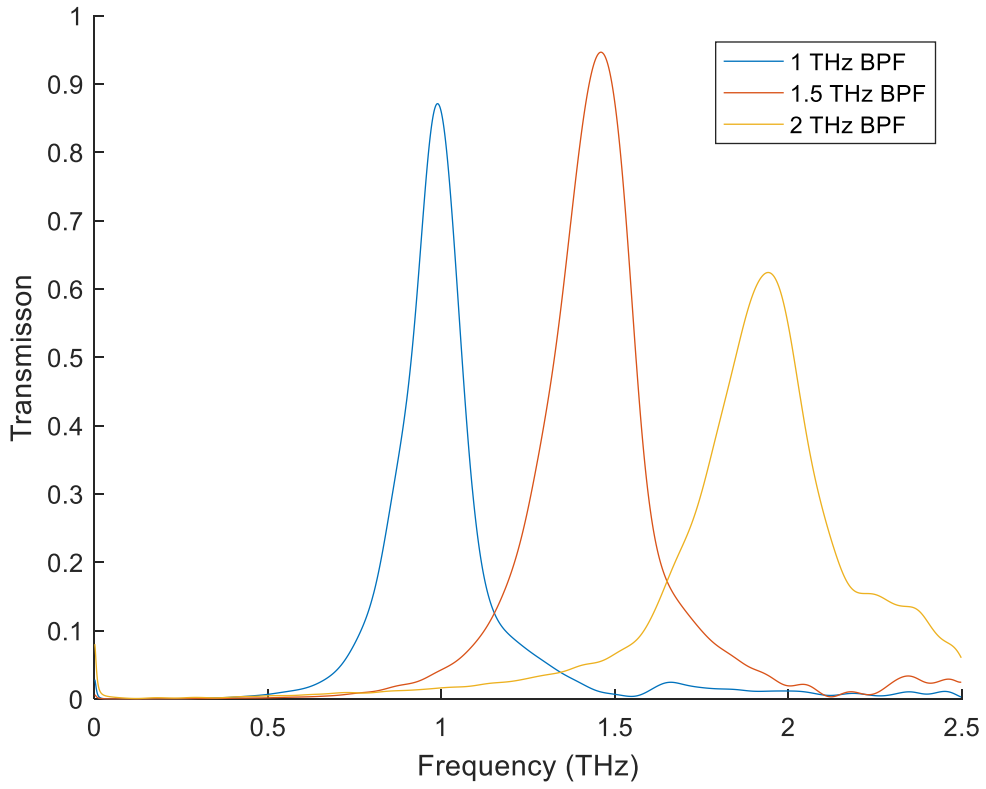

Figure 3.3: Power transmission of the 1 THz BPF, 1.5 THz BPF and 2 THz BPF measured by the THz-TDS.

This THz-TDS setup was also used to measure the dielectric properties of the diode materials used in the fabrication of the diodes used in this study [40]. By taking the Fourier transform of the time domain spectrum the frequency spectrum of the THz pulse can be determined. The normalized Fourier frequency spectrum is shown in Figure 3.2 for each of the reference, 1 THz bandpass filter, 1.5 THz bandpass filter and 2 THz bandpass filter measurements. A bandpass filter (BPF) passes light of certain frequencies, defined by its central wavelength and full-width at half-maximum, and rejects light of all other frequencies. The reference terahertz spectrum represents the detected Fourier frequency spectrum when no bandpass filters or other optics are used that may inhibit the electric field. The detected terahertz pulse generated in our system peaks at 500 GHz and extends out to near 2.5 THz. At 5.3 THz, the ZnTe has strong phonon resonance band that reduces the overall effectiveness of utilizing ZnTe as a terahertz detector at the higher frequencies [44, 45, 46].

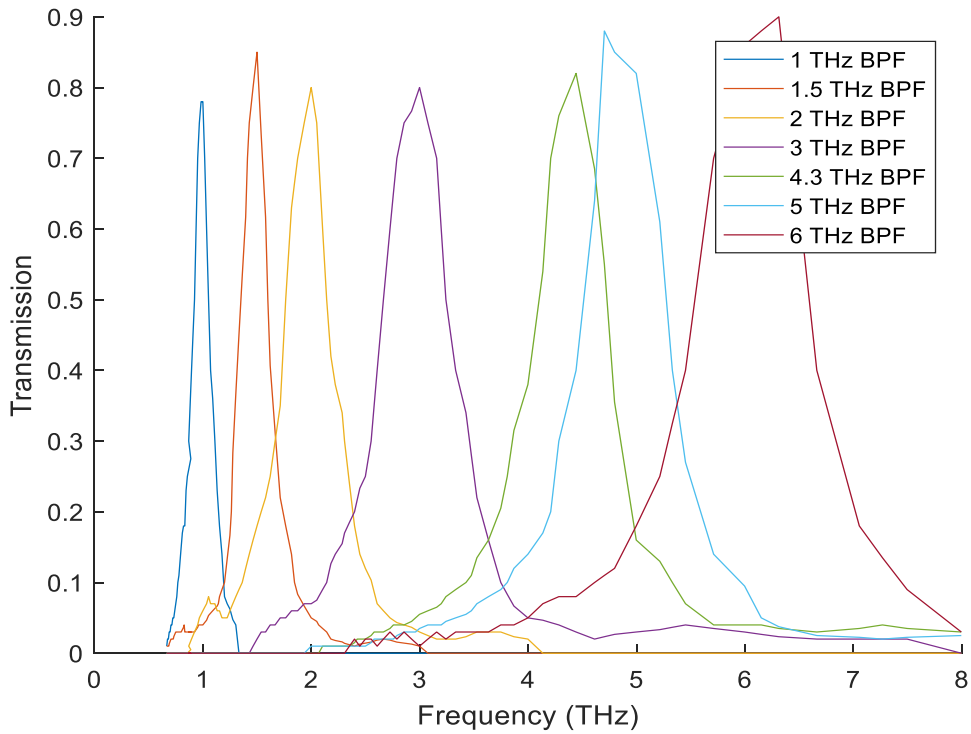

Figure 3.4: Transmission spectra of the terahertz bandpass filters, provided by the manufacturer, used in the power spectrum measurement [46].

The power transmission spectra of the bandpass filters, shown in Figure 3.3, are determined by taking the ratio of the squares of the electric field through the bandpass filters to the square of the electric field of the reference terahertz pulse. For the other higher frequency bandpass filters, the transmission spectra are provided by the manufacturer [47], shown in Figure 3.4. The detected electric field by the THz-TDS is not representative of the power emitted by the photoconductive antenna [40, 44, 46, 48]. To determine the power, a series of manipulations, that will be described in the subsequent sections, must be performed.

3.2 Terahertz Power

The primary motivation for this section is to determine the shape of the power spectrum that will be available for rectification for the rectenna studied in Chapter 4. The power was measured for frequencies greater than 1 THz using a series of terahertz bandpass filters. The

Fourier spectrum measured by the THz-TDS constitutes the detectable power spectrum and will require manipulations to determine an accurate shape of the terahertz power. The measured power spectrum and detected power spectrum are compared to provide a better understanding of the shape of the power spectrum. If the power spectrum at the rectenna is known, the spectrum can be integrated over the bandwidth of the antenna to determine the power into the device.

3.2.1 Peak Power

The peak intensity of the terahertz pulse was measured with a terahertz power meter (Gentec-EO THz9B-BL-BNC). A thin black polyethylene cover was placed over the power meter aperture to filter out ambient light, noise, and any remaining portion of the 805 nm pump beam that may reflect through the setup to the power meter. The absorption spectrum of the power meter and transmission spectrum of the black polyethylene are shown in Figure 3.5 and Figure 3.6, respectively. The absorption spectrum of the power meter and the transmission spectrum of the black polyethylene were provided by the manufacturer and any coarse points in the data provided were linearly interpolated. Using a 1.77 mm^2 circular aperture and a moveable three-dimensional stage, the peak measured irradiance of the terahertz radiation was found to be 900 mW/m^2.

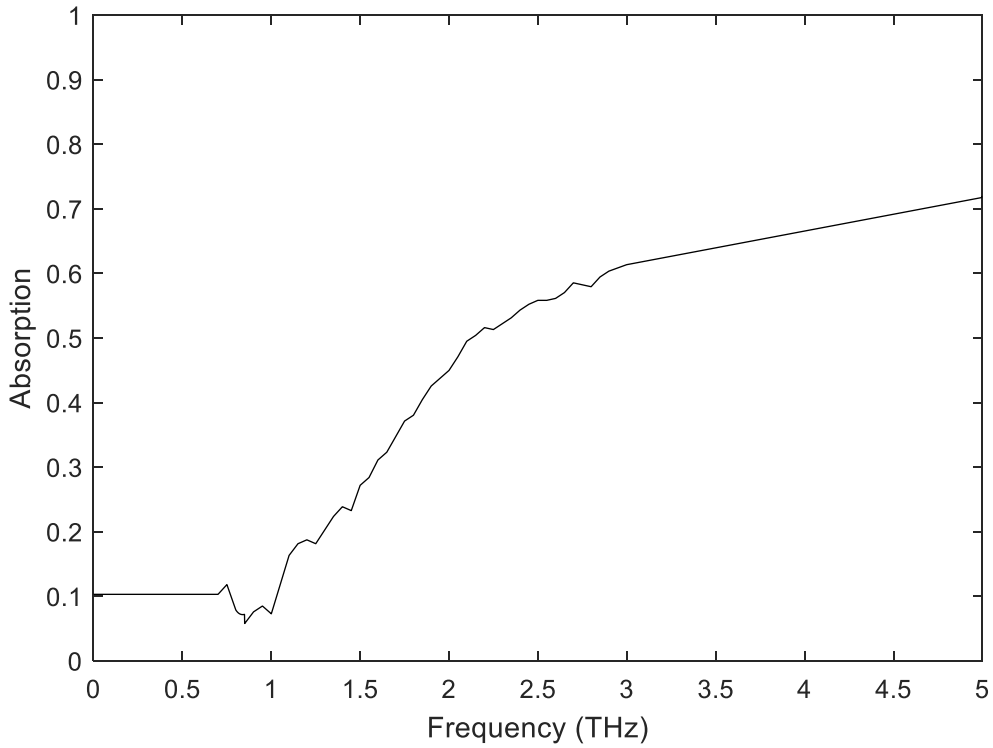

Figure 3.5: Absorption spectrum of the terahertz power meter provided by the manufacturer and any coarse points in the provided data were linearly interpolated.

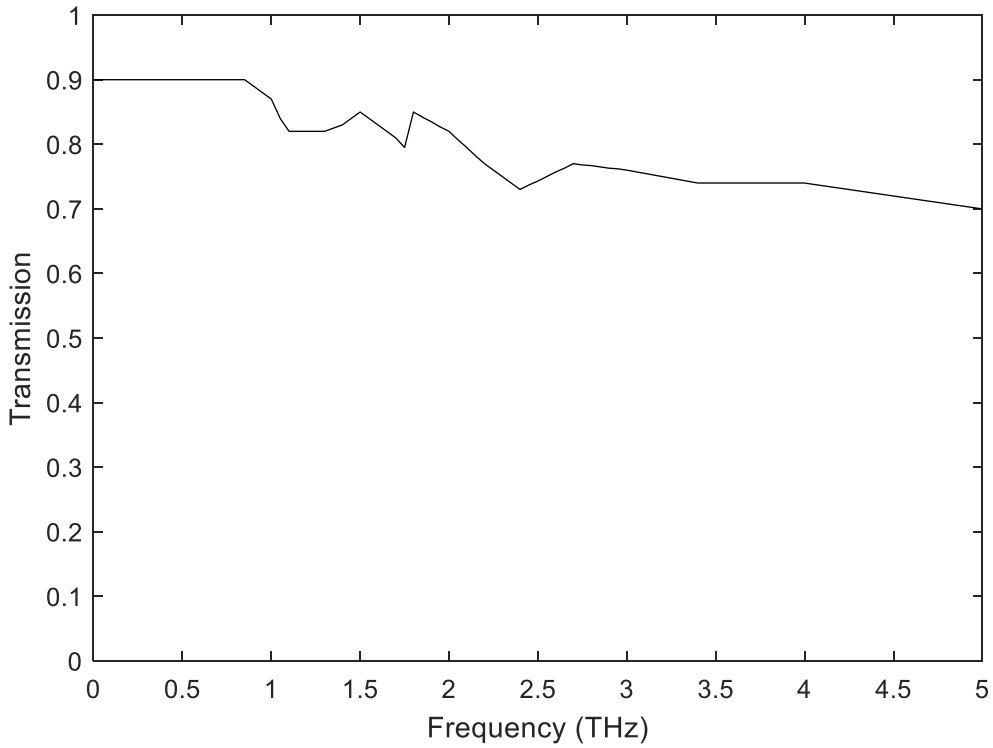

Figure 3.6: Transmission spectrum of the black polyethylene used to filter ambient light, heat and noise, especially the 805 nm pump pulse. Any coarse points in the provided data were linearly interpolated.

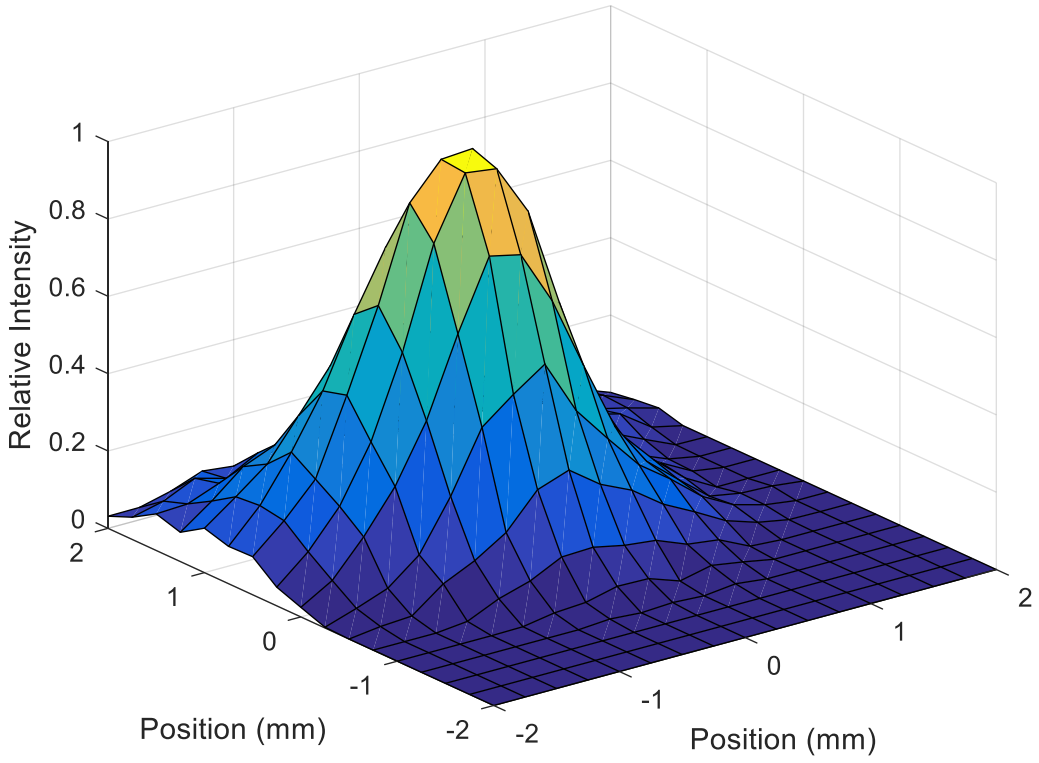

Figure 3.7: Location of the peak intensity of the terahertz radiation found by moving a 3-dimenional stage with a 1.77 mm^2 aperture and scanning the THz-TDS.

The resulting three-dimensional plot of the intensity at each 0.25 mm position is shown in Figure 3.7. The peak terahertz intensity is not located at the origin of Figure 3.7 but is symmetric around its peak. Using the aperture area of the antenna, 4.2x10^{-9} m^2 [49], and the peak power measured by the power meter, 900 mW/m^2, the maximum overall power delivered to the antenna is calculated to be 3.9 nW.

3.2.2 Frequency-Dependent Power Measurement

Using the bandpass filters, whose transmission spectra are shown in Figure 3.4, the power spectrum from 1 THz to 6 THz was measured using the terahertz power meter. Up to this point, the terahertz spectrum has been presented in arbitrary units of the electric field normalized to the peak value of the reference terahertz radiation. From this point onward, the terahertz electric

field spectrum will be squared to represent an arbitrary shape of the power spectrum. It is expected that the PCA emits terahertz radiation at the higher frequencies than what is shown in Figure 3.2, the spectrum of the detected terahertz. The inability to detect the terahertz electric field by the ZnTe crystal and THz-TDS instrumentation is due to deficiencies in ZnTe crystal [38]. The resulting measured power spectrum is shown in Figure 3.8. The measured power spectrum is fit to a power function to be compared to the estimated power spectrum from the detected Fourier power spectrum. The measured power spectrum demonstrates a $1/v^{3.1}$ dependence on the frequency from 1 THz to 6 THz with a R^2 value of 0.9988, where v is the terahertz frequency. The same circular aperture, with an area of 1.77 mm^2,

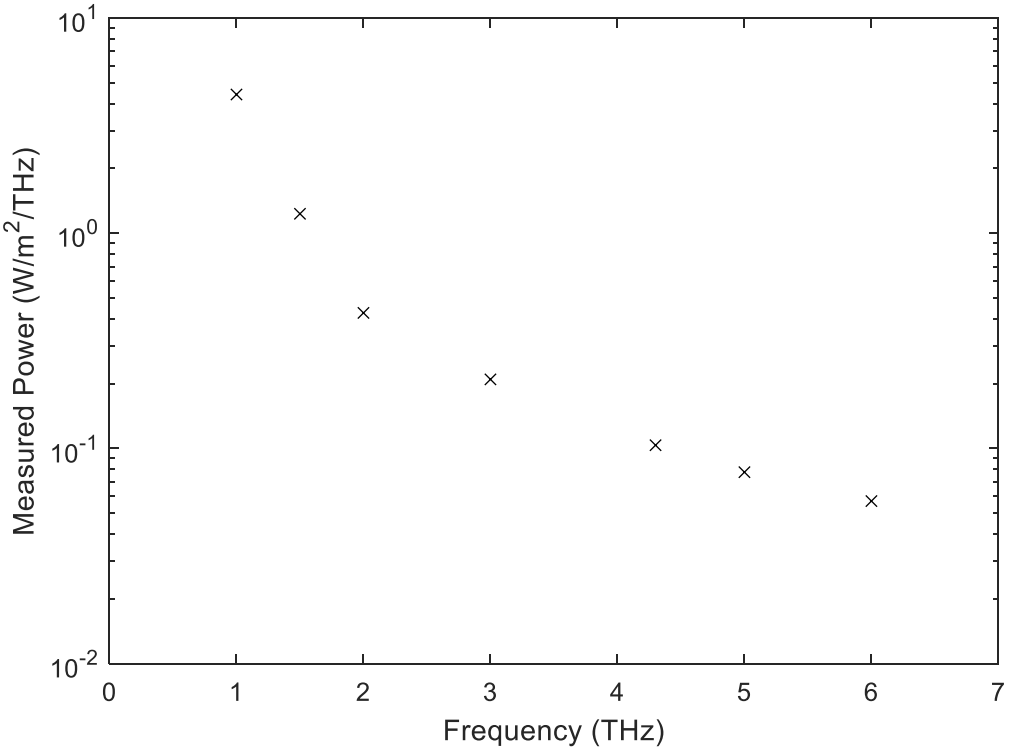

Figure 3.8: Measured power spectrum of the terahertz radiation shown in log scale and found by measuring the power through each bandpass filter and accounting for the transmission of the black polyethylene, absorption of the power meter, and transmission and FWHM of each bandpass filter.

and the same black polyethylene filter used in the total power measurement were applied. To calculate the attenuated power of each bandpass filter, the measured voltage from the power meter was converted to W/m^2/THz using the power meter responsivity, aperture area, single line transmission of each bandpass filter at the center frequency, single line transmission of the black polyethylene, single line absorption of the power meter and FWHM of each bandpass filter.

3.3 Estimated Power Spectrum

The shape of the power spectrum of the terahertz radiation from the Fourier transform is not accurately known due to deficiencies in the ZnTe as the crystal for detecting the terahertz. The measured power spectrum does not measure frequencies below 1 THz, where the power is expected to peak near 1 THz and diminish at lower frequencies [38]. Two methods to approximate the power spectrum at the operating frequencies of the rectenna are demonstrated using the detected electric field spectrum. The electro-optic response function for zinc telluride [44] and the detectivity for zinc telluride [48] are utilized to determine the terahertz electric field.

3.3.1 Electro-Optic Response Function of Zinc Telluride

Since the detected electric field depends strongly on the characteristics of zinc telluride, a series of modifications to the detected electric field through various transfer functions will provide an estimated power spectrum [44, 48]. For the power meter, it is important to adjust for the absorbance of the power meter and the transmittance of the black polyethylene, which has already been shown in Figure 3.5 and Figure 3.6, respectively. The zinc telluride detectability depends on the frequency-dependent material properties. To obtain an optimal response, the group velocity of the terahertz pulse should match the group velocity of the probe pulse in the ZnTe crystal [44]. The group velocity is defined as follows [50]:

$$V_g = \frac{c}{n}\left(1 + \frac{\lambda}{n}\frac{dn}{d\lambda}\right), \tag{3.3.1}$$

where *c* is the speed of light in a vacuum, *n* is the refractive index and λ is the wavelength of the light. For the 805 nm probe pulse, it is calculated that V_g/c in the ZnTe crystal is 0.304, which replicates numbers previously published [44]. For all subsequent calculations, it is assumed that the terahertz pulse and probe beam enter the ZnTe crystal parallel to the primary axis of the crystal and collinear with each other. The primary material property to be examined for the zinc telluride is the refractive index, *n*. At optical [51] and infrared [52] frequencies, the refractive index of ZnTe has been measured. Equation (3.3.2) [50] and Equation (3.3.3) are used to parameterize the refractive index at these frequencies.

$$n(\lambda) = \sqrt{A + \frac{B\lambda^2}{\lambda^2 - C}} \tag{3.3.2}$$

For zinc telluride, the values of the coefficients in Equation (3.3.2) have been experimentally measured [51]. From these experimental results, A = 4.27, B = 3.01 and C = 0.142. For the lower terahertz frequencies, the complex dielectric function, Equation (3.3.3), can be used to determine the refractive index [50].

$$\varepsilon(\omega) = \varepsilon_{el} + \frac{S_0 {\omega_0}^2}{{\omega_0}^2 - \omega^2 - i\Lambda_0\omega} = [n(\omega) + ik(\omega)]^2 \tag{3.3.3}$$

For ZnTe, the published values for the parameters of the fit of the complex dielectric function used in the following calculations are given in Table 3.1 [44, 45].

Table 3.1: Characteristic parameters for ZnTe in the calculation of the complex refractive index for use in Equation (3.3.3) [44, 45].

ε_{el}	7.4
S_0	2.70
$\Lambda_0/(2\pi)$	0.09 THz
$\omega/(2\pi)$	5.3 THz

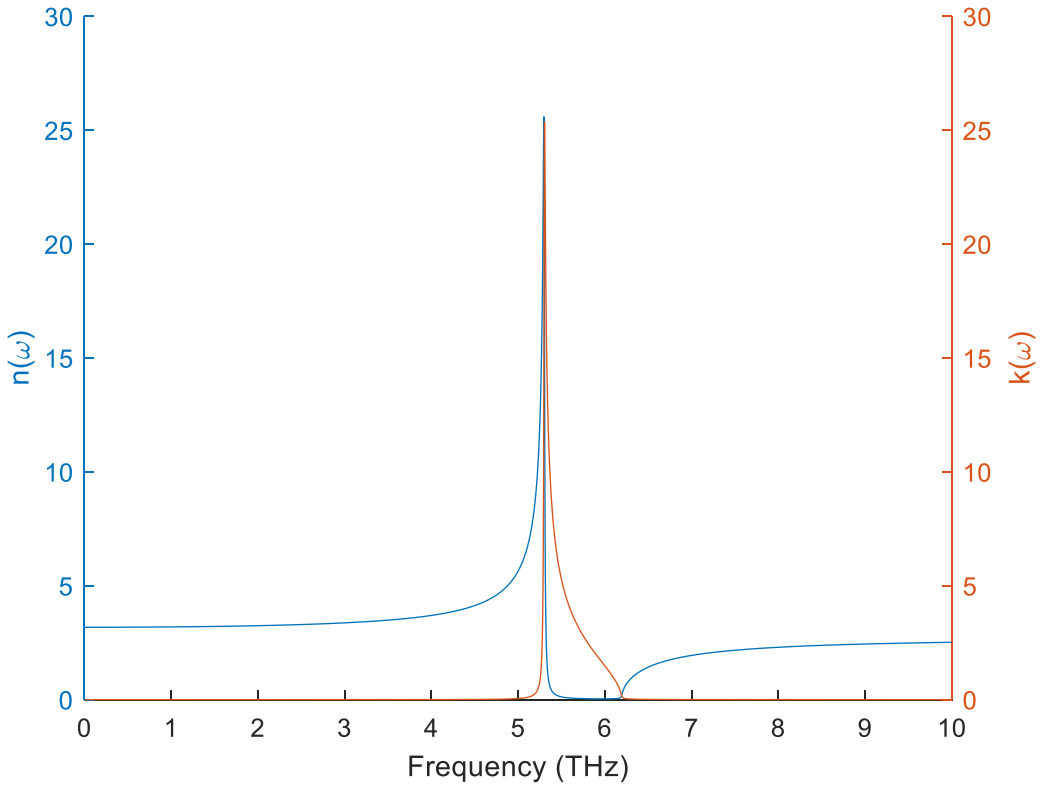

Figure 3.9: Real, or refractive index, n, and imaginary, or absorption coefficient, k, parts of the complex refractive index of zinc telluride calculated from Equation (3.3.3).

The real and imaginary parts of the refractive index generated from these previously published data are plotted as a function of frequency in Figure 3.9 [44, 52].

The electro-optic coefficient, r_{41}, another parameter which is used to characterize the electro-optic sampling provided by the non-linear crystal [44]. Since it is affected by the same lattice oscillations that effect the dielectric function, it is a similarly-structured equation with the values for Λ_0 and ω_0 remaining the same. The electro-optic coefficient, estimated from [44], is

$$r_{41}(\omega) = d_E\left(1 + \frac{C{\omega_0}^2}{{\omega_0}^2 - \omega^2 - i\Lambda_0\omega}\right). \tag{3.3.5}$$

For ZnTe, it is expected that the electro-optic coefficient at terahertz frequencies will not deviate substantially from its value at high frequencies. The values of the coefficients in Equation (3.3.5) are C = -0.07 and d_E = 4.25 × 10^{-12} m/V [44]. The remaining equations used to describe the transmission of light in the ZnTe crystal are the amplitude transmission, $A_{tr}(\omega)$, and the geometric response function, $G(\omega)$. The amplitude transmission is given by [44]

$$A_{tr}(\omega) = \frac{2}{n(\omega) + ik(\omega) + 1}. \tag{3.3.6}$$

Previous work [44] in this area has demonstrated the calculation of a geometric response function,

$$G(\omega) = \frac{1}{d}\int_0^d \exp\left(\frac{i\omega z}{v_{ph}(\omega)} - \frac{i\omega z}{v_g}\right)dz, \tag{3.3.7}$$

as well as, the confirmation of the refractive index and electro-optic coefficient, which is used here to estimate the detectability of the 2 mm ZnTe crystal used in this experimental setup. Equation (3.3.7) assumes that the angle between the polarization of the probe pulse, terahertz pulse and primary axis of the zinc telluride is zero degrees and that the two pulses overlap throughout the transmission through the crystal. The geometric response function for a given crystal depends on the thickness of the crystal, d.

The group velocity and phase velocity, v_g and v_{ph}, of the probe pulse and terahertz pulse, respectively, are functions of the refractive index of the crystal. The group velocity of the probe pulse, shown by the red dashed line, and the terahertz pulse, shown in black, in ZnTe are plotted in Figure 3.10. The sharp change in the group velocity of the terahertz pulse in the ZnTe is due to the phonon resonance in ZnTe at 5.3 THz.

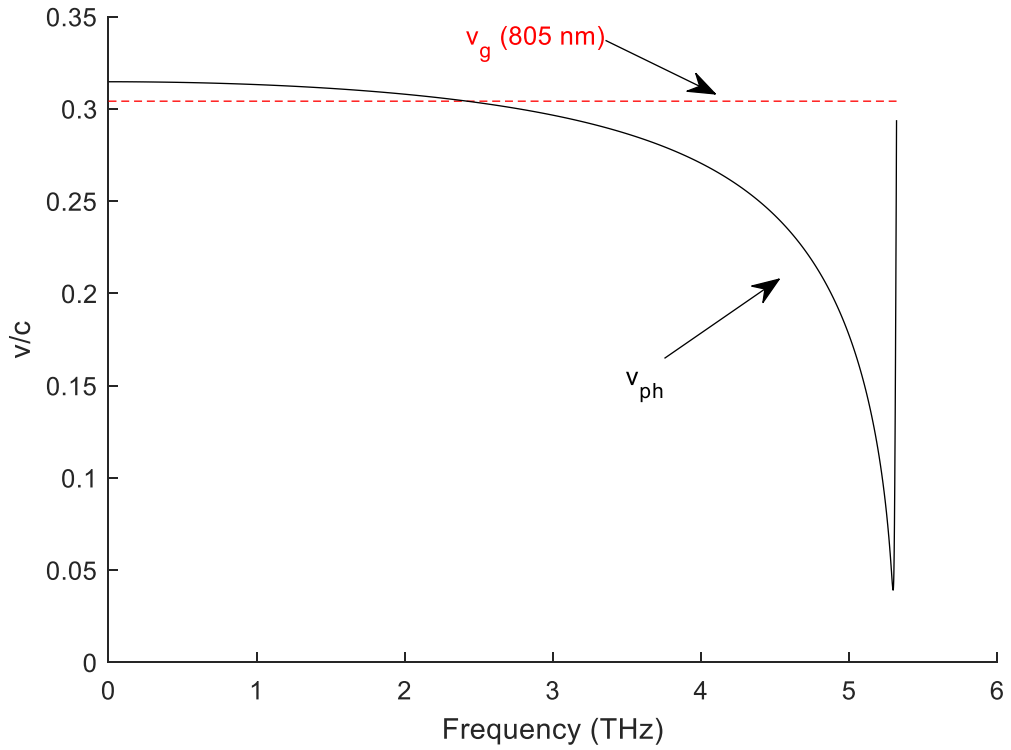

Figure 3.10: Phase and group velocity for the terahertz pulse (black) and probe pulse (red) in ZnTe calculated using Equation (3.3.1) and the respective ZnTe refractive index for the probe pulse frequency and the terahertz frequencies. The sharp change in the group velocity of the terahertz pulse in the ZnTe is due to a phonon resonance.

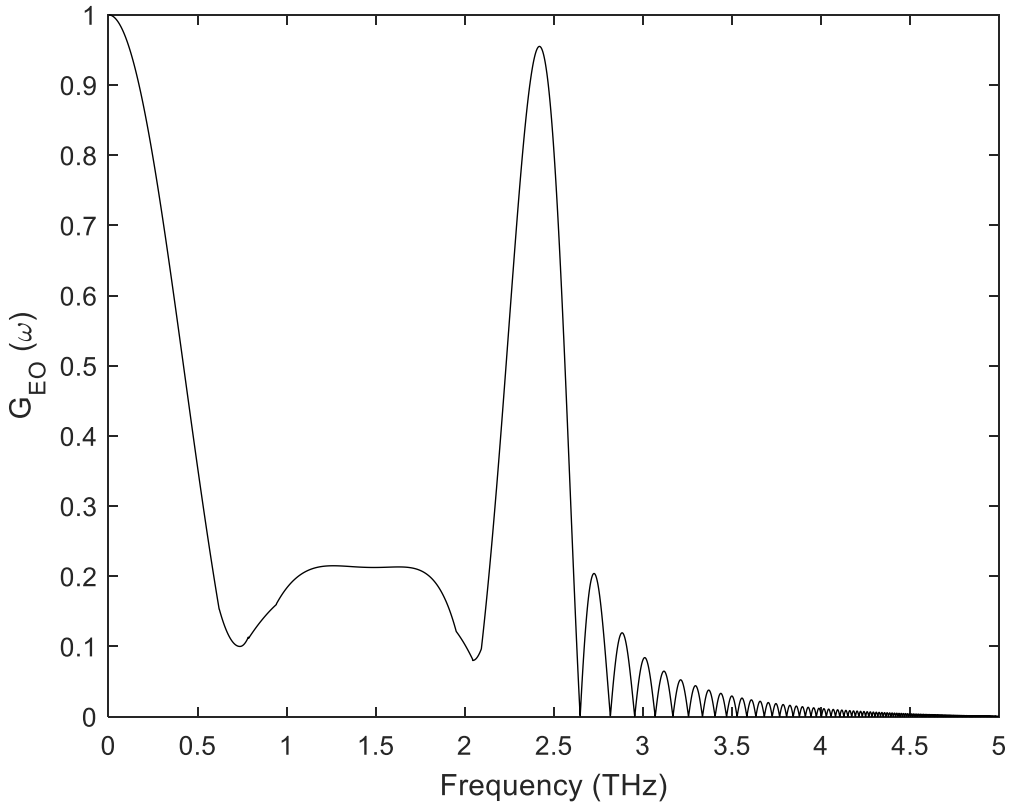

Figure 3.11: Electro-optic response function for ZnTe calculated using Equation (3.3.8). The dips in the electro-optic response at 800 GHz and 2.1 THz are due to phase retardation in the 2 mm thick ZnTe crystal. The peak at 2.4 THz appears when the group velocity in the ZnTe for each pulse is equal.

By combining the geometric response function, Equation (3.3.7), amplitude transmission function, Equation (3.3.6), and electro-optic coefficient, Equation (3.3.5), an electro-optic response function, G_{EO}, can be determined, shown in Figure 3.11.

$$G_{EO}(\omega) = G(\omega)A_{tr}(\omega)r_{41}(\omega) \tag{3.3.8}$$

The electro-optic response function for ZnTe can subsequently be used to account for the effects of the zinc telluride and the measured electric field. The peak at 2.4 THz demonstrates the maximum detection of ZnTe when the group velocities of the probe pulse and the terahertz pulse are equal.

3.3.2 Detection of Zinc Telluride

Another method with which is extract the power spectrum from Fourier frequency spectrum of the terahertz pulse is the use of a series of transfer functions [38]. Highlighted here is the transfer function for the detection of the zinc telluride [38, 48],

$$T_{DET} = \frac{2}{1 + n_{THz}(\omega)} \frac{\exp\left(\frac{id\omega}{c}\left(n_{THz}(\omega) - n_g\right)\right)}{\frac{i\omega}{c}\left(n_{THz}(\omega) - n_g\right)} \exp\left(\frac{-\left(\tau_p \omega\right)^2}{16\, ln(2)}\right). \tag{3.3.9}$$

In this transfer function, τ_P is the pulse duration of the probe beam, or the full-width at half-maximum of the probe pulse [38]. The first exponential term of the detection transfer function accounts for the dispersion, absorption and phase mismatch of the zinc telluride, similarly to the electro-optic response function, Equation 3.3.8. The second exponential term accounts for the loss of resolution caused by the finite duration of the probe beam [48]. Figure 3.12 is the detection transfer function for a 2 mm thick zinc telluride crystal, like the one used in our THz-TDS. The detection transfer function is similar in shape to the geometric response function with only a noticeably different peak height at 2.4 THz. The maximum of the geometric response function and ZnTe detection at 2.4 THz arises due to the exact matching of the phase velocity and the group velocity of the terahertz beam and probe beam in the zinc telluride, as seen in Figure 3.10. The second exponential term of the detection transfer function accounts for the dampening of the magnitude at high frequencies compared to the geometric response function.

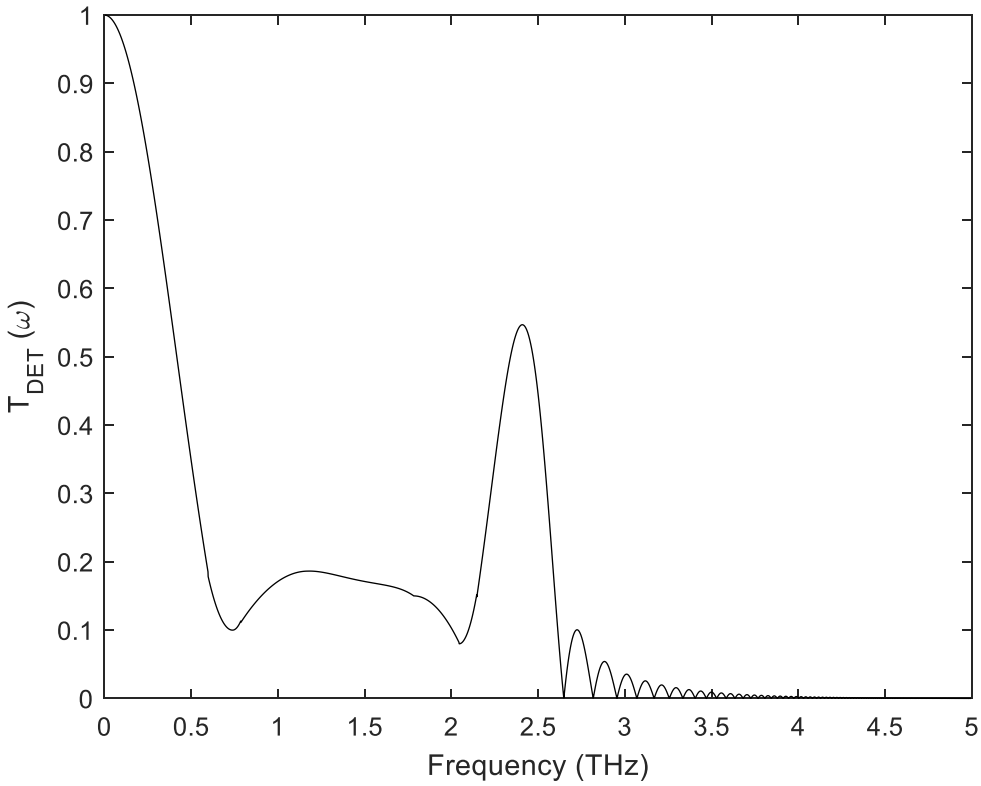

Figure 3.12: Terahertz detection transfer function for ZnTe calculated using Equation (3.3.9), which is used in the calculation of the terahertz power spectrum from the Fourier power spectrum. The dips in the detection transfer function at 800 GHz and 2.1 THz are due to phase retardation in the 2 mm thick ZnTe crystal. The peak at 2.4 THz appears when the group velocity in the ZnTe for each pulse is equal.

An additional transfer function, T_{OV}, for the overlap of the probe pulse and terahertz pulse is presented [48]. This transfer function accounts for the change in the beam width of the terahertz pulse as a function of frequency and the overlap between it and the width of the probe pulse. As Figure 3.13 demonstrates, this transfer function plays a larger affect at lower frequencies (< 1 THz) and peaks at 2 THz, given by [38]:

$$T_{OV} = \frac{r_{THz}(\omega)^2}{(2r_{THz}(\omega)^2 + {r_p}^2)^{\frac{1}{2}}}, \tag{3.3.10}$$

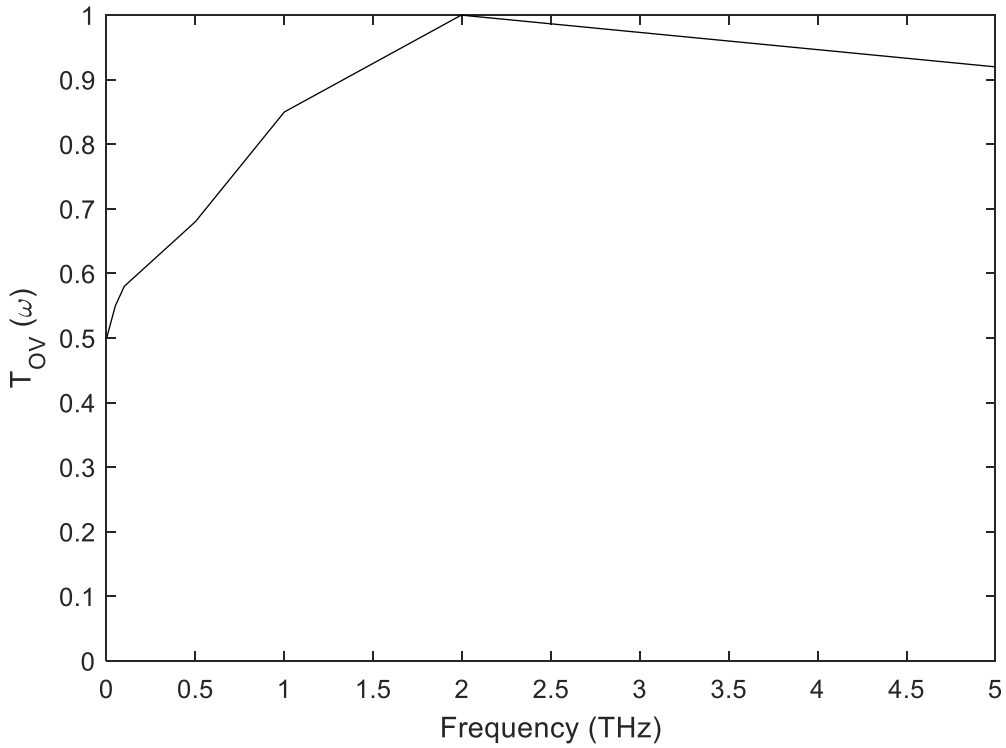

Figure 3.13: Transfer function for the overlap of the terahertz and probe pulses calculated using Equation (3.3.10).

where $r_{THz}(\omega)$ is the frequency-dependent radius of the terahertz pulse and r_p is the radius of the probe pulse.

Utilizing these transfer functions will account for the crystal effects of ZnTe and allow us to use the detected Fourier frequency spectrum to estimate the shape of the terahertz power spectrum. This detected power spectrum was then compared to the measured terahertz power spectrum using the power meter.

3.3.3 Estimation of the Terahertz Power Spectrum

To estimate the power spectrum from the Fourier spectrum, we will assume that the probe beam and terahertz beam enter the zinc telluride at an angle equal to the primary axis of the crystal. When aligning the system, the crystal is rotated to achieve a maximum signal so that

this can be confidently assumed. We will also assume the propagation and dispersion effects of the terahertz pulse in air are negligible. With these assumptions, the normalized Fourier frequency spectrum of the terahertz pulse, corrected with the appropriate transfer functions, gives the shape of the power spectrum, where its integration gives the total amount of power measured by the power meter. The integral of the square of the electric field frequency spectrum, given in Equation (3.3.11), can be used to determine the amount of power at a given frequency range by assigning the integral the amount of power measured by the power meter in a given frequency range:

$$E_{meas} = \frac{E_{det}}{a_{PM} t_{poly} T_{det} T_{ov}} \tag{3.3.11}$$

$$P_{Total} = \int_{-\infty}^{\infty} {E_{meas}}^2 \, d\omega \tag{3.3.12}$$

E_{meas} is the measurable electric field for the terahertz power meter that has been corrected for the transfer functions, E_{det} is the Fourier frequency spectrum of the electric field that is detected, a_{PM} is the absorption of the power meter and t_{poly} is the transmission of the black polyethylene cover. To confirm that this method accurately estimates the power over a frequency range, two experiments were performed. In the first, the power through three bandpass filters was measured and compared to the estimated power by found by Equation (3.3.12) when using the reference spectrum, where the frequency range is set to the FWHM of the transmission spectrum for each bandpass filter. In the second, the Fourier electric field spectrum detected for each of the bandpass filters was integrated following Equation (3.3.12) and the ratio that integral to the reference spectrum integral is used to estimate the power for each bandpass filter.

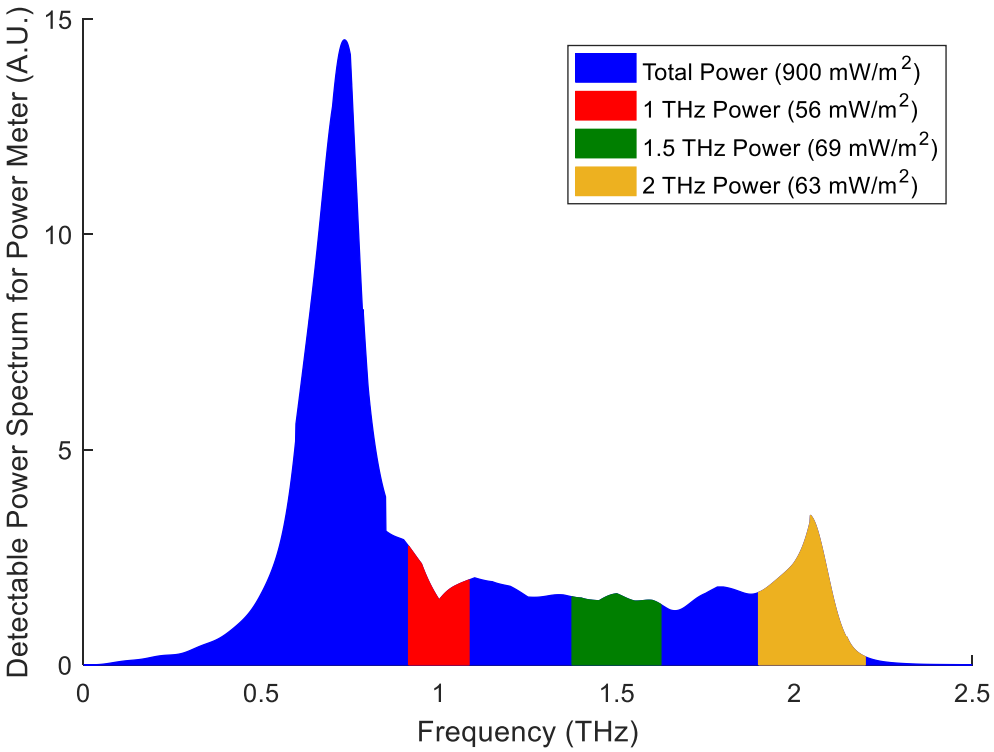

Figure 3.14: Detectable power spectrum for power meter demonstrating the first method for estimating terahertz power through each bandpass filter. The total power measured by the power meter without the use of any bandpass filters is assigned to the entire power spectrum, shown in blue. The power measured through each bandpass filter is estimated by integrating this power spectrum over the FWHM of each bandpass filter and multiplied by the central wavelength transmission.

Figure 3.14 and Figure 3.15 provide a visualization of these two methods to estimating the power measured by the power meter. Table 3.2 shows the results of this study, where the frequency is the centerline frequency of each bandpass filter. The power of the terahertz radiation is expected to peak around 1 THz and diminish precipitously at higher frequencies, as shown in Figure 3.16. Figure 3.8 demonstrates the measurable power spectrum for the power meter for the reference terahertz pulse and each of the bandpass filters used. It can be concluded that at the frequencies examined here, 1 THz to 2 THz, Equation (3.3.10) can be used to estimate the power transmitted over a given frequency range.

Table 3.2: Results of the Terahertz bandpass filter power study.

Frequency (THz)	FWHM (THz)	Estimated Power: Method 1 (mW/m^2)	Estimated Power: Method 2 (mW/m^2)	Measured Power (mW/m^2)
1.00	0.17	56	72	62
1.50	0.25	69	75	70
2.00	0.30	60	73	58

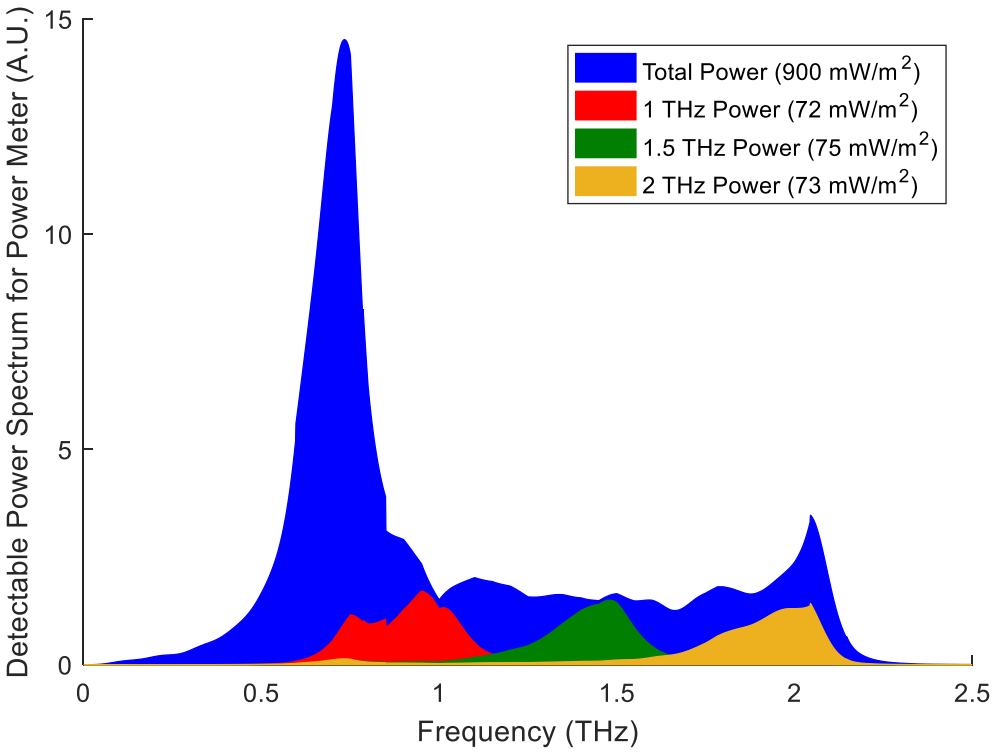

Figure 3.15: Detectable power spectrum from the power meter for the reference THz, 1 THz BPF, 1.5 THz BPF and 2 THz BPF accounting for all transfer functions. This represents the second method with which the terahertz power through each bandpass filter is measured. The total power measured without any bandpass filters used is assigned to the entire detectable power spectrum, shown in blue. The power measured through each bandpass filter is estimated by integrating the detectable Fourier spectrum of each bandpass filter.

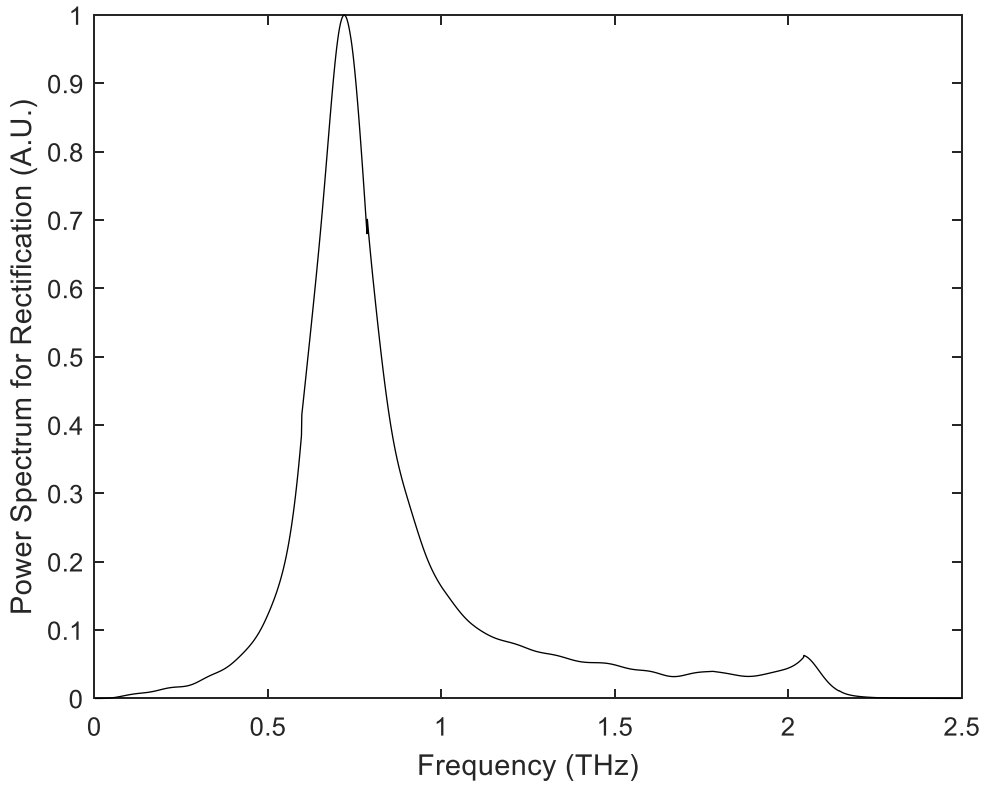

Figure 3.16: Estimated power spectrum at the rectenna using Fourier spectrum and transfer functions for ZnTe. The peaks at approximately 800 GHz and 2.1 THz are likely due to the phase retardation in the ZnTe crystal, shown in Figure 3.12.

Figure 3.16 shows the estimated power spectrum at the rectenna calculated from the Fourier spectrum and modified with the transfer functions T_{DET} and T_{OV}. The power spectrum greater than 1 THz is fit to a power function to compare to the measured power spectrum. The estimated power spectrum is found to be proportional to a $1/v^{2.7}$ with a coefficient of determination of 0.95. The rate at which the power diminishes with increasing frequency for our terahertz source for both methods of measuring or estimating the power is proportional to $1/v^3$ to a reasonable approximation.

3.3.4 Caveats for Power Approximation

The terahertz pulse propagation through the ZnTe crystal is crucial to understanding the accurate reconstruction of the true shape of the terahertz power spectrum. The estimation used

here compensates for a couple of the many effects of the ZnTe: group velocity mismatch between the terahertz pulse and the probe pulse, and the refractive index, absorption, dispersion, phase mismatch, and loss of resolution [44, 48]. Additionally, a few more effects could play a role in more accurately describing the shape of the detected electric field, including the phase retardation, Fabry–Perot reflections inside the crystal, and laser pulse broadening [44]. Since the measurements taken here are firmly in the region where the terahertz pulse is detectable, this approximation has been shown to be appropriate to estimate the power for a given bandwidth in the frequency range greater than 1 THz. This estimation and further modifications to it will be necessary when determining the absorbable power for the rectenna and the rectenna efficiency. The terahertz power spectrum from the modified Fourier electric field spectrum reasonably compares when estimating the power spectrum from the power meter. Not all the effects of terahertz propagation, zinc telluride optics or power detection are completely accounted for in this estimation. Future work should pertain to confirming the shape of the power spectrum, especially at lower frequencies (< 1 THz).

3.4 Conclusions

A method for terahertz radiation generation and detection was presented. Using terahertz bandpass filters, the power spectrum of the terahertz radiation was measured from 1 to 6 THz but is significantly reduced at frequencies greater than 3 THz. The detected Fourier frequency spectrum is corrected for a series of transfer functions to estimate the shape of the terahertz power spectrum. The estimated power spectrum and measured power spectrum compared relatively well to a $1/\nu^3$ dependence for frequencies greater than 1 THz. The estimated terahertz power spectrum can be integrated over the appropriate frequencies to calculate the power in the range of frequencies, approximately 1-2 THz, measured.

Chapter 4 Rectification of Terahertz Radiation using MIIM Diodes in a Rectenna

4.1 Terahertz Rectification

Rectification using metal-insulator-metal (MIM) and metal-insulator-insulator-metal (MIIM) diodes has been shown at near-infrared frequencies with low efficiencies [33, 39], while others have demonstrated rectification at much lower RF frequencies [11, 53]. Since higher frequency waves have higher energy, the target operating frequency for energy harvesting purposes is in the optical or infrared ranges. Therefore, understanding rectenna operation at terahertz frequencies and bridging the gap between ultra-high frequency microwave and optical frequency operation is critical.

4.2 Rectenna Fabrication and Characterization

4.2.1 Fabrication of Antenna and Diode

The material set for the diodes measured are Ni-NiO-Nb_2O_5-CrAu and Ni-NiO-ZnO-CrAu, building from the bottom up of the diode stack. The rectenna used in this experiment were fabricated by our colleagues at the University of Colorado-Boulder [39]. The rectenna are fabricated using a germanium shadow mask process where the bottom layer nickel is thermally evaporated at an angle 43^o to the right of the germanium shadow mask bridge. The NiO is grown in an oxygen plasma. The next insulator layers, Nb_2O_5 and ZnO, are then sputter deposited. The chromium, used as an adhesion layer, and gold, used for its optimum optical properties at 1 THz, are then evaporated at normal incidence. The insulator thickness plays a crucial role in determining the diode resistance, responsivity and capacitance. For the first set of diodes, the insulator thickness of NiO and Nb_2O_5 is estimated to be 3 nm and 2 nm, respectively, while the

insulator thickness of NiO and ZnO in the second set is 3 nm and 2 nm, respectively. The antenna design is a traditional bowtie antenna design, shown in Figure 4.7.

4.2.2 Diode DC I(V) Characteristics

The DC I(V) curve of a Ni-NiO-Nb_2O_5-CrAu device and Ni-NiO-ZnO-CrAu is shown in Figure 4.1 and Figure 4.2, respectively, as measured using a four-point probe measurement system. The data is fit to a two-term exponential function with a coefficient of determination of 1.0000 for the diodes with Nb_2O_5 and 0.9999 for the diodes with ZnO.

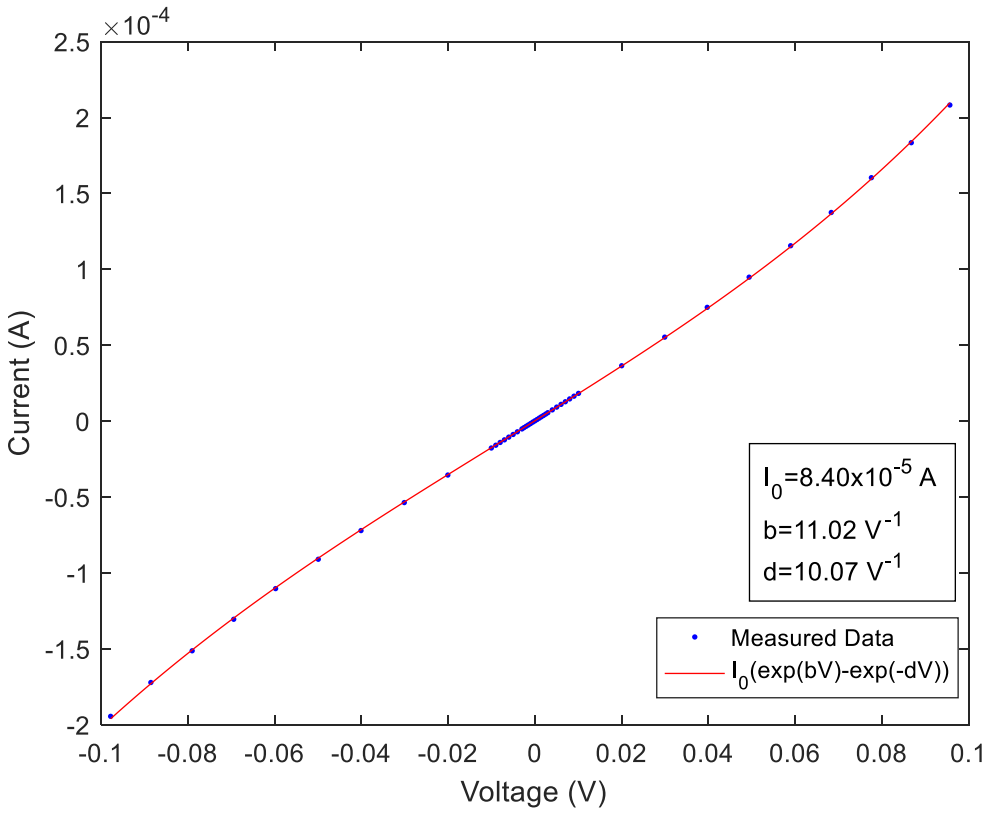

Figure 4.1: I(V) curve for a typical Ni-NiO-Nb_2O_5-CrAu diode used in the rectification experiments is shown with coefficients from the two-term exponential fit.

The coefficient of determination is a value that quantifies the quality of the linear regression fit. The coefficients of the two-term exponential fit (I_0, b and d) are shown in the respective figures for each device. Figure 4.3 and Figure 4.4 show the diode differential resistance and responsivity

for each of the material sets. In these plots, the non-linearity of the device is easily deduced. The resistance at 0.1 V and −0.1 V clearly varies, which shows the asymmetry of each diode. From Equation (1.5.5) and Equation (1.5.7), the zero-bias resistance of the niobium oxide diode is 566 Ω and the zero-bias responsivity is 0.51 A/W.

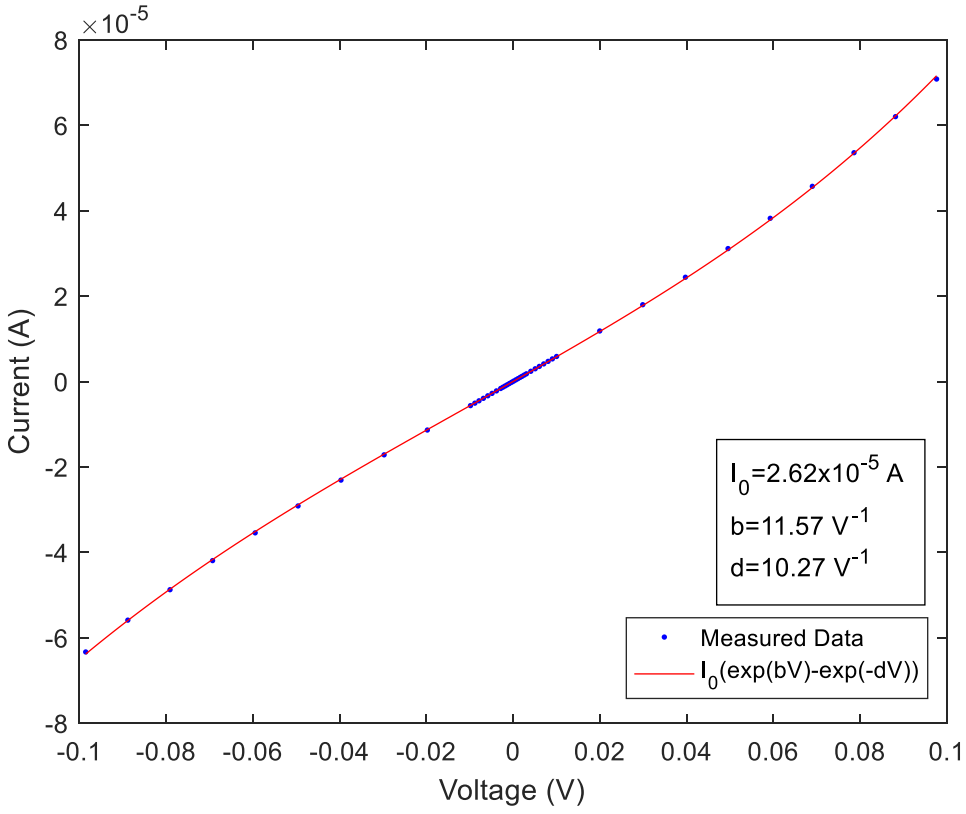

Figure 4.2: I(V) curve for a typical Ni-NiO-ZnO-CrAu diode used in the rectification experiments is shown with coefficients from the two-term exponential fit.

The zero-bias resistance of the zinc oxide diode is 1745 Ω and the zero-bias responsivity is 0.65 A/W. All rectenna were fabricated under the same conditions in each sample set. A large sample size of devices was then measured and tested. The distribution of the diode resistance and zero-bias responsivity is shown in the probability plots, Figure 4.5 and Figure 4.6. The S-shape of the

probability plot suggests a bell curve distribution in the measured devices. The probability plots do not include linear devices.

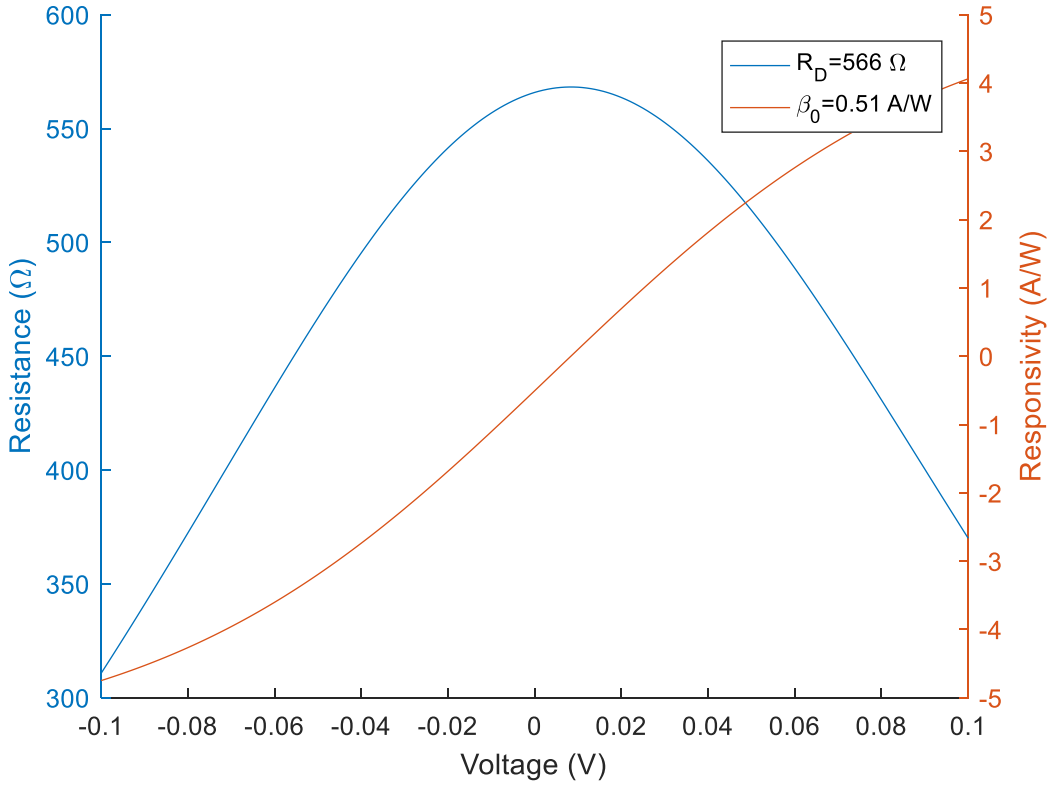

Figure 4.3: Resistance and responsivity curves for a typical Ni-NiO-Nb_2O_5-CrAu diode calculated from fit to a two-term exponential equation.

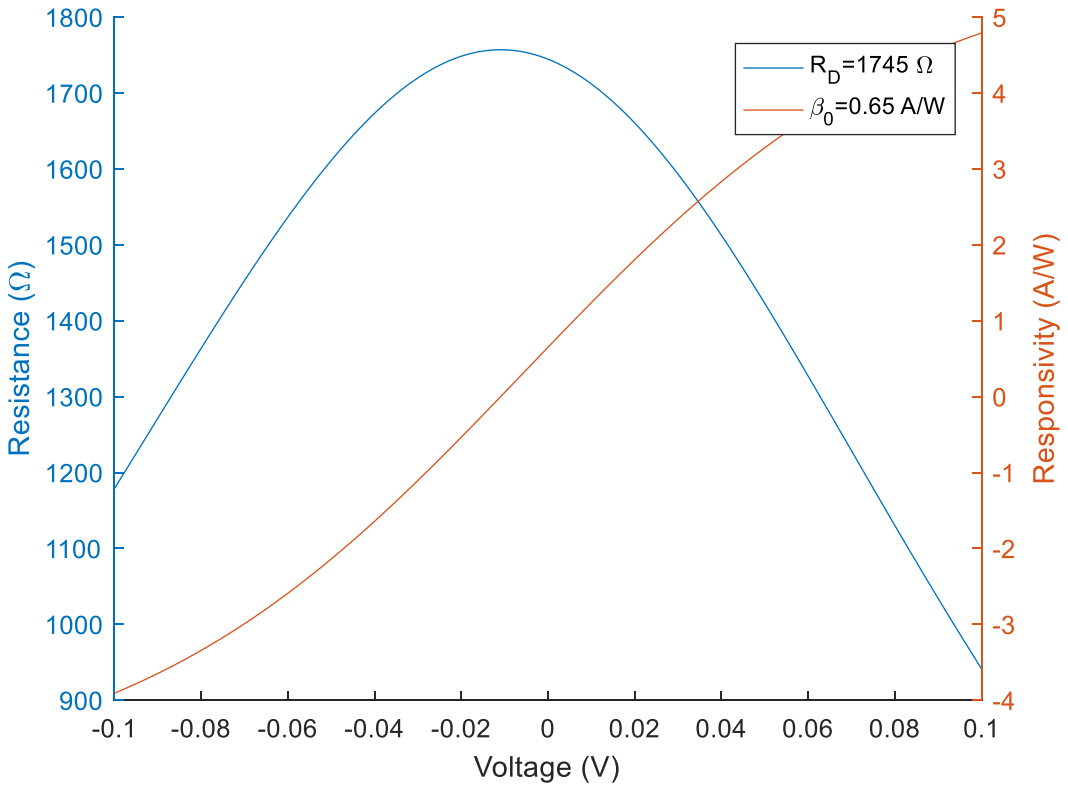

Figure 4.4: Resistance and responsivity curves for a typical Ni-NiO-ZnO-CrAu diode calculated from a fit to the two-term exponential function.

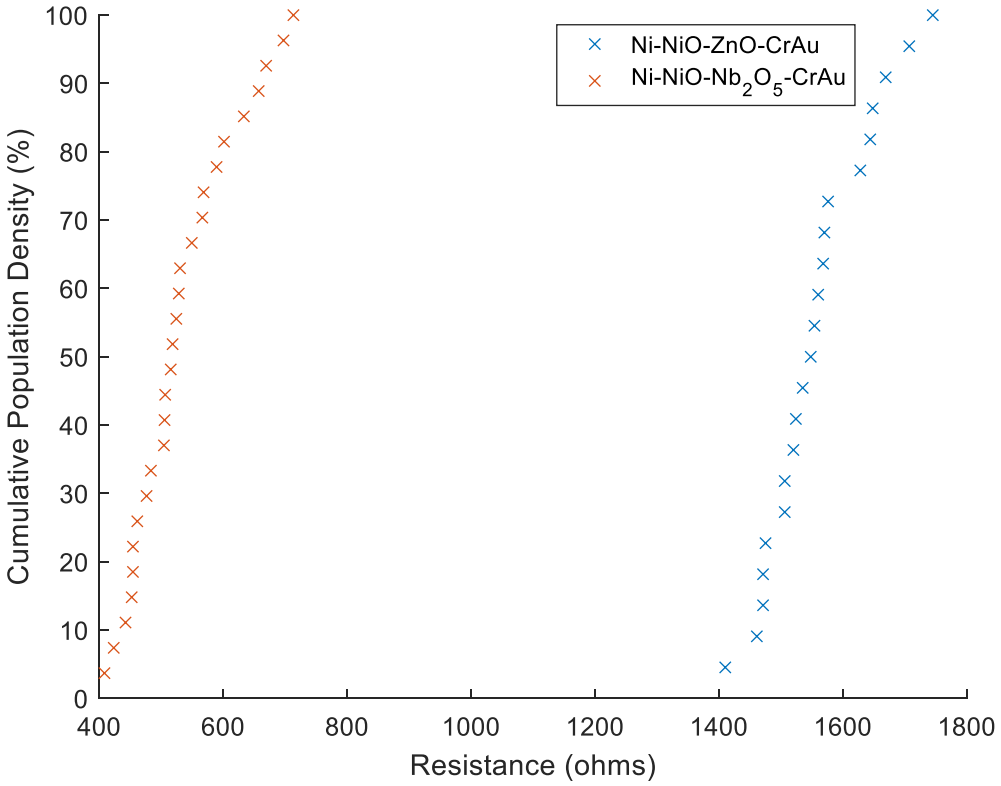

Figure 4.5: Distribution probability plot of the diode resistance of the entire test group used in the rectification studies.

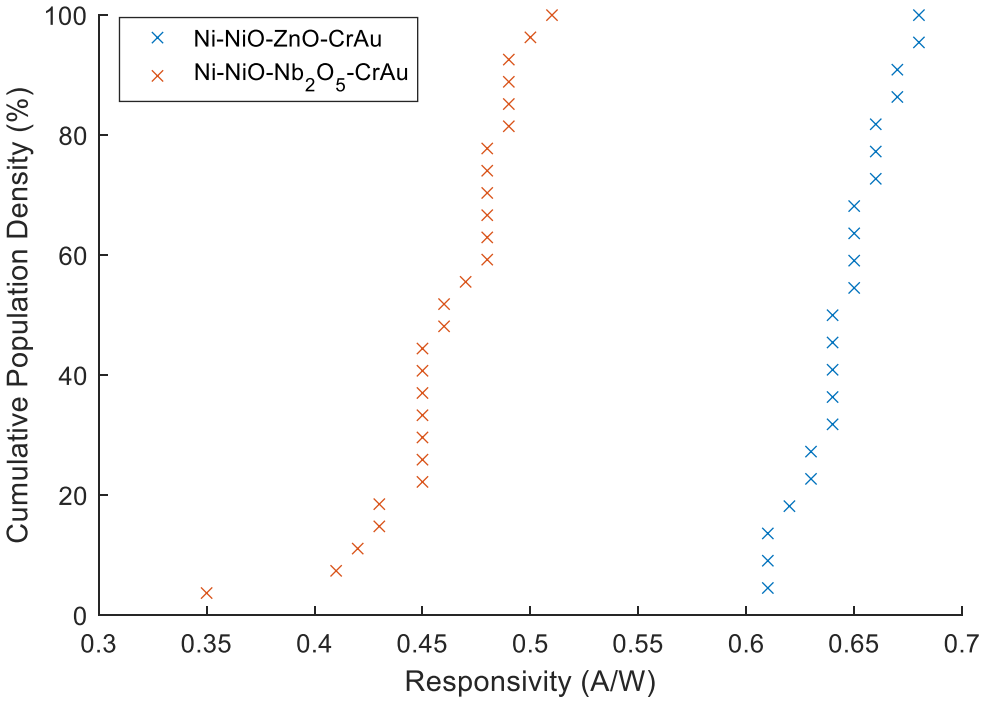

Figure 4.6: Distribution probability of the zero-bias responsivity of the entire test group used in the rectification studies.

4.3 Rectification of Terahertz Radiation

4.3.1 Rectification Measurement

The MIIM rectenna terahertz operation was tested under illumination from the THz-TDS system described in Section 3.1. The rectenna was placed at the point of peak power as measured using the three-dimensional translational stage, shown in Figure 3.7. A rotatable linear wire-grid polarizer is placed in the collimated portion of the terahertz pulse. The wire-grid polarizer is used to block the linearly polarized terahertz pulse to confirm a response to the terahertz radiation

Figure 4.7: Rectenna test setup is visualized with terahertz bowtie rectenna in center, highlighted by the blue circle, and electrical testing pads for four-point probe and illumination testing. The inset in the lower left-hand corner is an illustration of the bow-tie antenna with the diode located in the center, where the two fins of the antenna come together.

rather than electrical noise in the system. The pump portion of the infrared beam is passed through a mechanical chopper oscillating at 311 Hz to supply a frequency for the lock-in amplifier (Stanford Research Systems SR810 DSP) with a time constant of 3 s. The open-circuit RMS voltage of the rectenna is measured using the lock-in amplifier. An image of an individual rectenna connected to the test pads for four-point probe and illuminated testing is shown in Figure 4.7. Using the open circuit voltage, diode resistance, diode responsivity and antenna efficiencies, the AC power absorbed by each rectenna can be calculated. The results of the Ni-NiO-Nb_2O_5-CrAu rectenna are tabulated in Table 4.1, while the results of the Ni-NiO-ZnO-CrAu rectenna are shown

in Table 4.2. Both sets of materials estimate the P_{AC} of the terahertz source to be approximately 0.7-0.8 nW. The variability of the estimated AC power is likely due to the assumption that all the devices of a given material set have the same capacitance and antenna resistance. That assumption is sufficient in place of a lack of a high frequency capacitance measurement, but just as the devices, although fabricated the same, have different resistances and responsivities, it is expected that the capacitance will vary as well.

Table 4.1: Terahertz illumination results for Ni-NiO-Nb_2O_5-CrAu rectenna.

	R_D (Ω)	B_0 (A/W)	V_{OC} (nV)	Measured P_{DC} Out (W)	Calculated P_{AC} In (W)	Rectenna Efficiency (%)
	483	0.46	40.9	8.64E-19	9.12E-10	9.47E-08
	423	0.41	34.1	6.89E-19	8.84E-10	7.79E-08
	452	0.45	34.0	6.41E-19	7.94E-10	8.07E-08
	442	0.45	29.1	4.78E-19	6.73E-10	7.11E-08
	408	0.48	33.6	6.92E-19	7.45E-10	9.29E-08
	476	0.50	26.0	3.54E-19	5.39E-10	6.57E-08
	461	0.45	26.7	3.86E-19	6.14E-10	6.28E-08
	505	0.45	30.4	4.56E-19	7.02E-10	6.51E-08
	633	0.48	61.8	1.51E-18	1.30E-09	1.16E-07
	657	0.35	40.8	6.35E-19	1.16E-09	5.48E-08
	566	0.51	40.8	7.36E-19	8.20E-10	8.97E-08
	506	0.48	30.2	4.51E-19	6.47E-10	6.97E-08
	515	0.47	34.8	5.87E-19	7.66E-10	7.67E-08
	454	0.42	32.7	5.90E-19	8.05E-10	7.33E-08
	454	0.49	20.2	2.25E-19	4.32E-10	5.22E-08
	518	0.43	29.4	4.16E-19	6.97E-10	5.98E-08
	530	0.48	25.8	3.14E-19	5.52E-10	5.69E-08
	504	0.46	27.4	3.71E-19	6.09E-10	6.09E-08
	713	0.49	38.8	5.28E-19	7.87E-10	6.71E-08
	568	0.43	22.9	2.32E-19	5.38E-10	4.31E-08
	524	0.48	30.5	4.45E-19	6.55E-10	6.79E-08
	528	0.48	33.2	5.23E-19	7.09E-10	7.37E-08
	601	0.45	27.5	3.14E-19	6.19E-10	5.08E-08
	549	0.45	33.1	5.00E-19	7.43E-10	6.73E-08
	589	0.49	40.0	6.80E-19	8.30E-10	8.18E-08
	669	0.49	40.9	6.26E-19	8.27E-10	7.57E-08
	697	0.45	42.2	6.38E-19	9.38E-10	6.80E-08
AVERAGE	**534**	**0.46**	**33.6**	**5.51E-19**	**7.52E-10**	**7.10E-08**
STD DEVIATION	**82**	**0.03**	**8.1**	**2.44E-19**	**1.81E-10**	**1.51E-08**

Table 4.2: Terahertz illumination results for Ni-NiO-ZnO-CrAu rectenna.

	R_D (Ω)	β_0 (A/W)	V_{OC} (nV)	Measured P_{DC} Out (W)	Calculated P_{AC} In (W)	Rectenna Efficiency (%)
	1644	0.64	96.1	1.41E-18	7.06E-10	1.99E-07
	1669	0.64	102.6	1.58E-18	7.50E-10	2.10E-07
	1707	0.61	81.8	9.79E-19	6.25E-10	1.57E-07
	1648	0.61	77.8	9.18E-19	6.02E-10	1.52E-07
	1576	0.62	73.7	8.61E-19	5.60E-10	1.54E-07
	1568	0.64	120.8	2.33E-18	8.96E-10	2.60E-07
	1628	0.68	94.1	1.36E-18	6.55E-10	2.08E-07
	1524	0.66	101.9	1.70E-18	7.28E-10	2.34E-07
	1461	0.64	86.2	1.27E-18	6.37E-10	1.99E-07
	1570	0.65	91.5	1.33E-18	6.66E-10	2.00E-07
	1520	0.66	85.7	1.21E-18	6.18E-10	1.96E-07
	1548	0.61	80.5	1.05E-18	6.21E-10	1.69E-07
	1475	0.65	88.8	1.34E-18	6.52E-10	2.05E-07
	1506	0.68	98.9	1.62E-18	6.89E-10	2.36E-07
	1410	0.64	74.7	9.89E-19	5.56E-10	1.78E-07
	1745	0.65	111.3	1.77E-18	8.01E-10	2.21E-07
	1471	0.63	100.4	1.71E-18	7.61E-10	2.25E-07
	1471	0.63	100.4	1.71E-18	7.61E-10	2.25E-07
	1506	0.66	111.3	2.06E-18	7.95E-10	2.59E-07
	1554	0.67	107.8	1.87E-18	7.61E-10	2.46E-07
	1535	0.65	109.8	1.97E-18	7.97E-10	2.47E-07
	1560	0.67	116.5	2.17E-18	8.21E-10	2.65E-07
AVERAGE	***1559***	***0.64***	***96.0***	***1.51E-18***	***7.03E-10***	***2.11E-07***
STD DEVIATION	***83***	***0.02***	***13.4***	***4.12E-19***	***8.90E-11***	***3.36E-08***

4.3.2 Antenna Polarization

To confirm rectification of the terahertz pulse, the rectenna is rotated with respect to the linearly polarized terahertz radiation. The angle between the antenna and the linearly polarized terahertz radiation, Θ, is shown in Figure 4.8. Figure 4.9 illustrates the polarity of the terahertz with respect to the antenna polarization as it is rotated. When the antenna is aligned with the polarization of the terahertz pulse, the maximum open-circuit voltage is expected; when the antenna is perpendicular to the polarization of the terahertz pulse, a minimum open-circuit voltage should be measured. As expected, Figure 4.10 and Figure 4.11 demonstrate that when

the beam polarization is aligned with the axis of the antenna (0°, 180° and 360°), the maximum open-circuit voltage is measured. It is expected that the rectenna open-circuit voltage has a cosine-squared dependence on the polarization angle [16],

$$V_{oc} = V_{Rect} \cos^2 \theta + V_{thermal} \sin^2 \theta \,. \tag{4.3.1}$$

Figure 4.10 shows the relationship of the measured open circuit voltage as a function of the polarization angle of the rectenna with respect to the terahertz polarization for the Ni-NiO-Nb_2O_5-CrAu rectenna. From the fit of Equation (4.3.1), the rectified voltage is 44 nV with a measured peak open-circuit voltage of 56 nV and a thermal voltage of 9 nV with a R^2 value of 0.77 for the Ni-NiO-Nb_2O_5-CrAu device. For the Ni-NiO-ZnO-CrAu device, shown in Figure 4.11, the rectified voltage is 104 nV with a peak open circuit voltage of 122 nV; the thermal voltage is 70 nV with an R^2 of 0.71.

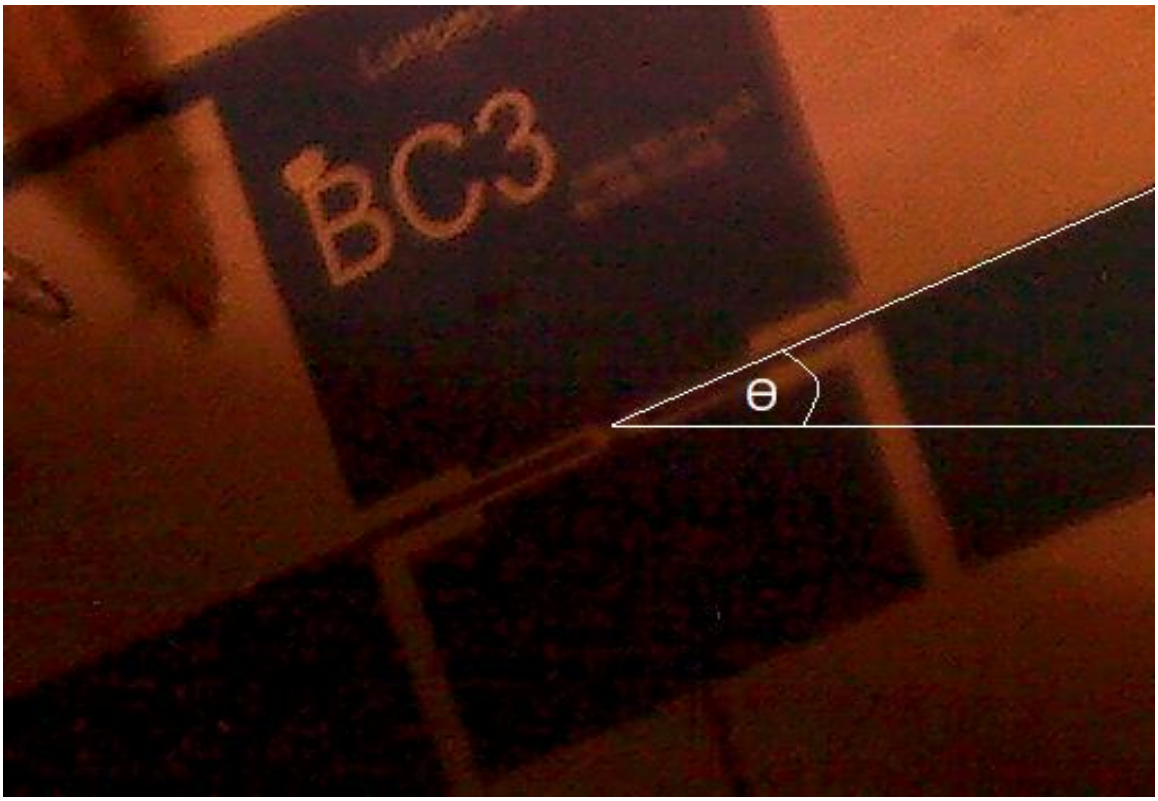

Figure 4.8: Antenna polarization angle respect to terahertz polarization on the horizontal axis is demonstrated with rectenna located in center of image.

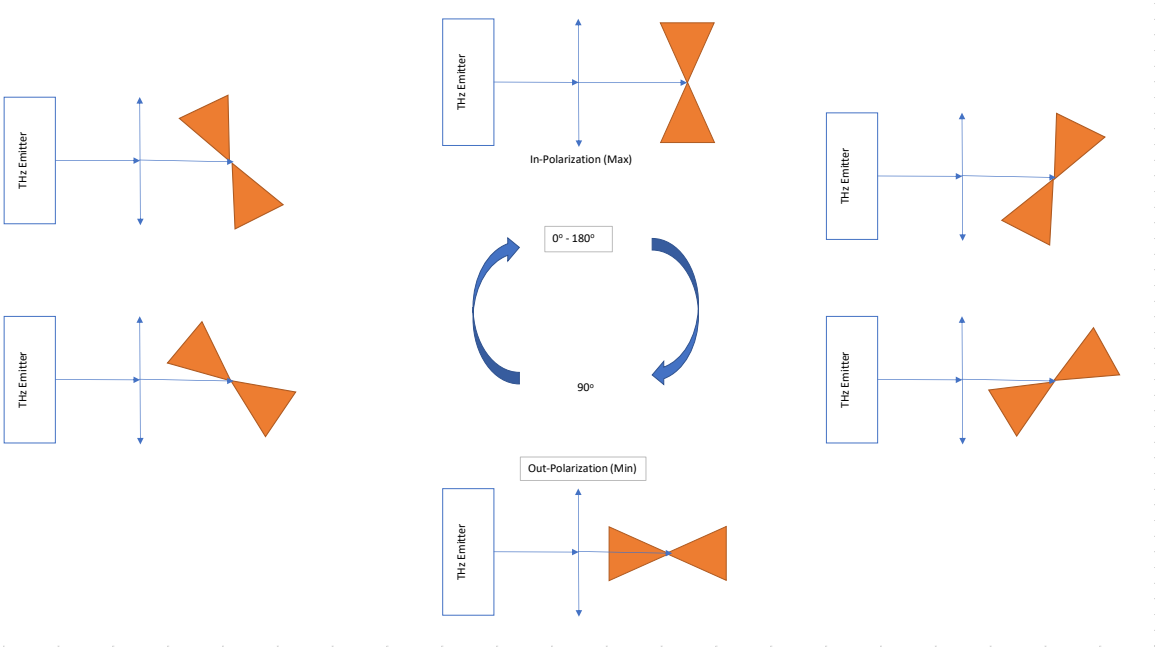

Figure 4.9: Illustration of the polarization test and polarization dependence of rectenna with respect to terahertz polarization demonstrating how the polarization of the rectenna and terahertz radiation are related.

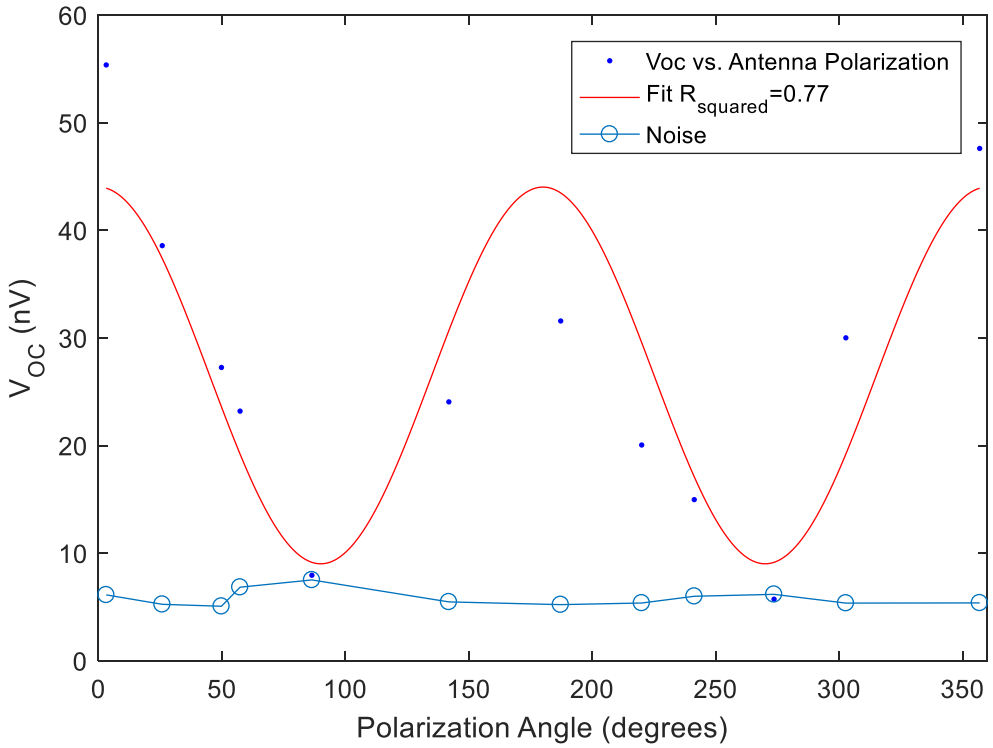

Figure 4.10: The open-circuit voltage of a Ni-NiO-Nb_2O_5-CrAu rectenna depends on the antenna polarization angle with respect to incident terahertz radiation.

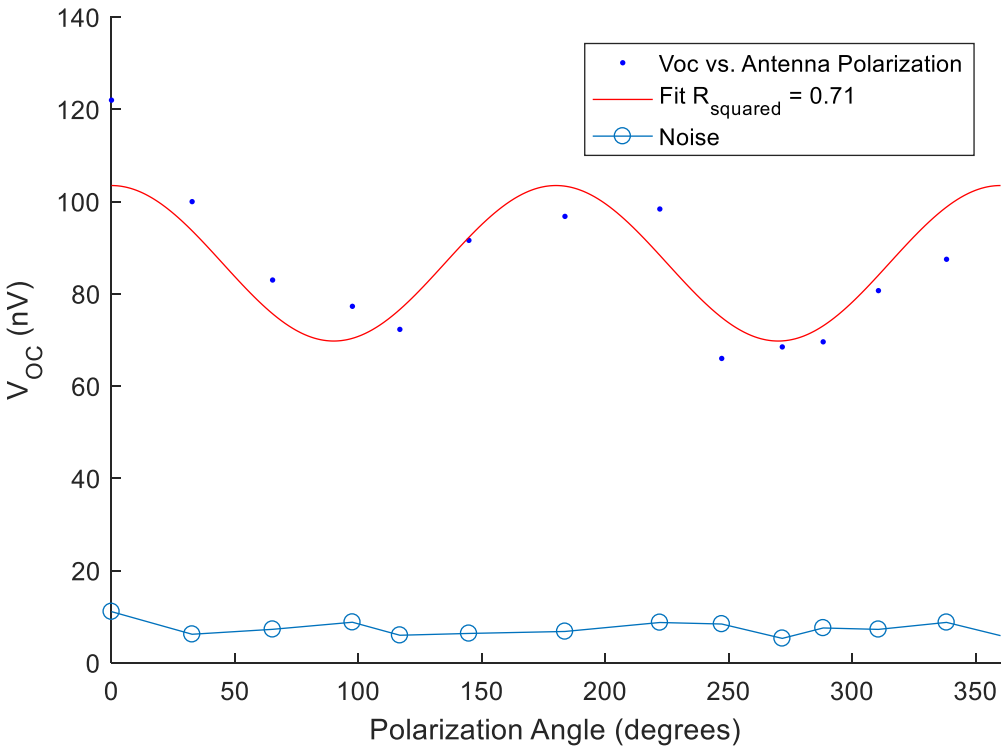

Figure 4.11: The open-circuit voltage of a Ni-NiO-ZnO-CrAu rectenna depends on the antenna polarization angle with respect to incident terahertz radiation.

By rotating the sample with respect to the polarization of the terahertz pulse, the rectification of the device is confirmed. Any thermal response for the Ni-NiO-Nb_2O_5-CrAu is indistinguishable from the noise of the measurement. For the Ni-NiO-ZnO-CrAu device, a substantial portion of the response is due to a thermal response. Since zinc oxide has a much lower thermal conductivity than niobium oxide, it can be expected that larger thermal gradients exist in the diode thereby driving the thermo-electric effect [54]. The Seebeck thermo-electric effect, which is shown in Equation (4.3.2), describes the voltage generated between two adjacent materials with a thermal gradient between them [55].

$$V_{thermal} = (S_1 - S_2)\Delta T \tag{4.3.2}$$

The Seebeck coefficient, *S*, for ZnO and Nb_2O_5 has been measured previously to be of the same order of magnitude [56, 57]; thus, the larger temperature gradient due to the low thermal

conductivity of zinc oxide can explain the larger thermal response. Results of the polarization study are shown in Table 4.3.

Table 4.3: Results of a three-angle polarization study for both material sets.

Material Set	R_D (Ω)	β_0 (A/W)	0° V_{oc} (nV)	45° V_{oc} (nV)	90° V_{oc} (nV)	Noise (nV)
Ni-NiO-Nb_2O_5-CrAu	465	0.47	36.8	11.9	5.7	5.6
Ni-NiO-Nb_2O_5-CrAu	503	0.46	38.8	11.2	3.8	5.5
Ni-NiO-Nb_2O_5-CrAu	564	0.49	55.4	27.3	7	5.8
Ni-NiO-ZnO-CrAu	1471	0.63	100.4	58.9	54.7	7.1
Ni-NiO-ZnO-CrAu	1506	0.66	111.3	70.6	62.0	6.7
Ni-NiO-ZnO-CrAu	1554	0.67	107.8	75.3	59.3	9.4

4.3.3 Non-Linear Versus Linear Devices

Linear devices of both material sets were additionally measured under illumination from the terahertz pulse and the open-circuit voltage of these devices remained at the noise level of the instrumentation to provide additional support to the determination of the terahertz response mechanism. Generally, there are three mechanisms for the rectenna response under illumination: photovoltaic, photo-thermoelectric, and photo-bolometric [55]. The I(V) curve of one of the linear Ni-NiO-Nb_2O_5-CrAu rectenna is shown in Figure 4.12. This result, coupled with the results of the polarization study, support the result of AC to DC rectification of the terahertz radiation through a photovoltaic effect rather than a photo-thermoelectric or photo-bolometric response for the Ni-NiO-Nb_2O_5-CrAu rectenna [23]. For the Ni-NiO-ZnO-CrAu, rectification is due to multiple mechanisms. For the photo-thermoelectric effect, a temperature gradient generates a current according to the Seebeck effect. In the photo-bolometric effect, photon-phonon interactions in the rectenna lead to an increase in localized temperature and an increase in resistance, thus reducing the current [55]. For the diodes with zinc oxide, it is evident that the response is due to a combination of the Seebeck effect and the photoelectric effect that is desired. Since none of

the linear devices responded to the terahertz radiation, it can be reasonably deduced that the photo-bolometric effect plays an insignificant role in the mechanism of the response. If the terahertz radiation caused a temperature gradient that generated a response for the linear devices that act as ohmic resistors, the photo-bolometric effect may exist to a more significant extent. Since the devices that have linear I(V) curves are likely linear due to dielectric breakdown in the diode, it is possible that a larger photo-bolometric effect occurs for an "intact" diode, especially in the Ni-NiO-ZnO-CrAu rectenna. However, with current evidence, the likely mechanisms are the photo-electric effect, confirmed by the polarization dependence of the rectenna, and the thermo-electric effect. The results for the remaining linear devices are found in Table 4.4.

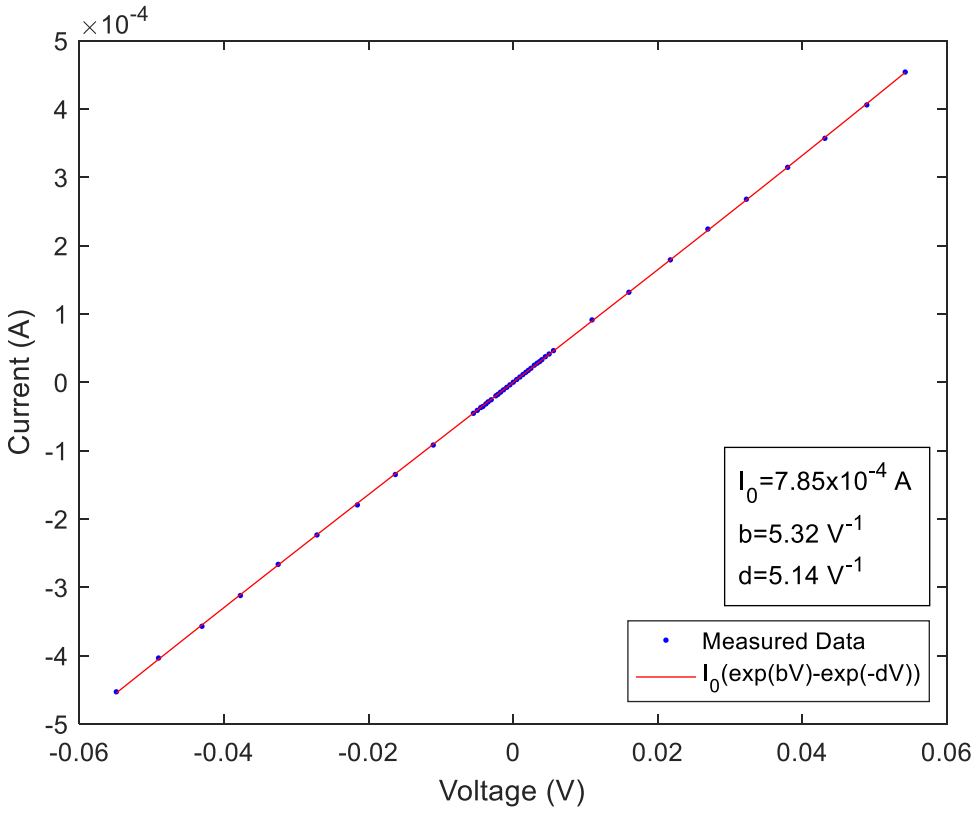

Figure 4.12: I(V) data of linear device used as confirmation of a rectification response is presented with coefficients from the two-term exponential fit.

Table 4.4: Terahertz illumination results of linear devices.

Material Set	R_D (Ω)	β_0 (A/W)	V_{OC} (nV)
Ni-NiO-Nb_2O_5-CrAu	101	-0.04	-0.1
Ni-NiO-Nb_2O_5-CrAu	122	0.09	1.3
Ni-NiO-ZnO-CrAu	94	-0.03	-0.9
Ni-NiO-ZnO-CrAu	131	-0.01	-1.5
Ni-NiO-ZnO-CrAu	31	-0.02	0.7
Ni-NiO-ZnO-CrAu	165	0.04	-0.5
AVERAGE	**105**	**0.00**	**-0.6**
STD DEVIATION	**50**	**0.03**	**0.8**

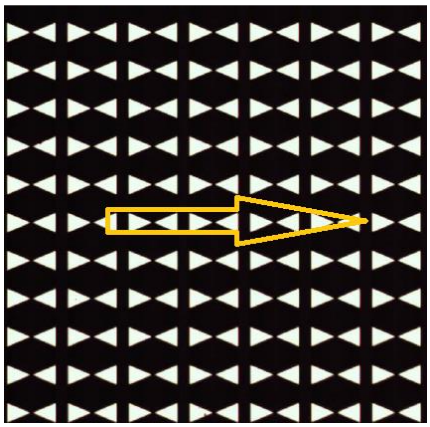

Figure 4.13: The array antenna used as a frequency-selective surface to determine the resonance frequency of the rectenna. The yellow arrow in the figure illustrates the direction of the electric field.

4.3.4 Attenuated Terahertz Rectification

The expected peak operating resonance frequency of the antenna is 800 GHz with an estimated bandwidth of 100 GHz. The antenna was designed as an array antenna with a resonant frequency of 1.2 THz, but when the antenna is removed from the array and the diode is added, the expected resonance drops to around 800 GHz [49]. The frequency selective surface, FSS, of the array antenna, shown in Figure 4.13, was previously modeled and measured to confirm the resonance frequency at 1.2 THz, shown in Figure 4.14 [38]. The operating frequency should depend on the materials in the diode. The antenna characteristics such as radiation impedance, radiation efficiency, resonance frequency, and bandwidth were provided by collaborators also working on the project [49].

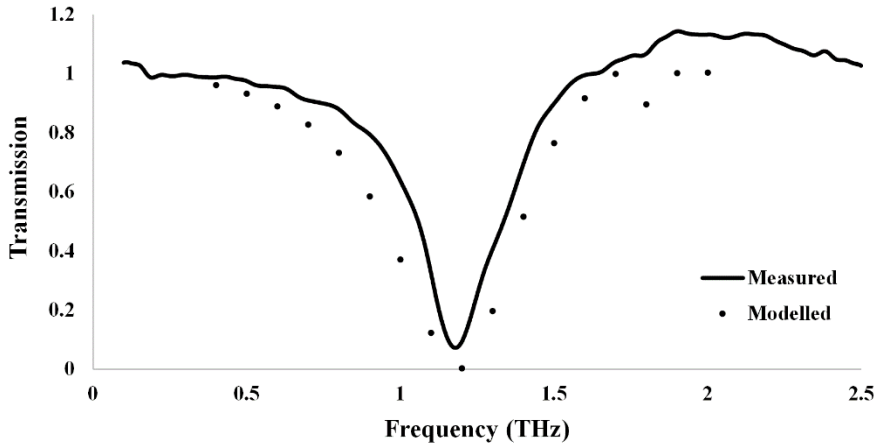

Figure 4.14: The frequency-selective surface, Figure 4.13, was modeled and measured to determine the resonance frequency of the array. When the transmittance of the terahertz radiation is reduced to zero, it is being absorbed by the antenna. This occurs at approximately 1.2 THz [38].

To test the operating frequency of the rectenna, the rectified open circuit voltage was measured through a 1 THz and 1.5 THz bandpass filter. Because of the low voltage response of the Ni-NiO-Nb_2O_5-CrAu rectenna through the 1 THz bandpass filter, the signal to noise ratio was increased by increasing the time constant of the lock-in amplifier to 10 s and longer scans were performed. For the Ni-NiO-ZnO-CrAu rectenna, the time constant and test conditions remained the same as the previous tests. All results are reported as the average rectified voltage above the noise level. The average rectified open circuit voltage for the reference terahertz pulse is 33.9 nV for the Ni-NiO-Nb_2O_5-CrAu rectenna and 96.0 nV for the Ni-NiO-ZnO-CrAu rectenna, tabulated in Table 4.1 and Table 4.2. For the purposes of reporting an accurate average rectified voltage, the Ni-NiO-ZnO-CrAu devices with lower resistance and responsivity were omitted for comparison to the statistically standard device. All results for measured devices of both material sets are tabulated in Appendix II.I and Appendix II.II.

For ten Ni-NiO-Nb_2O_5-CrAu rectenna tested for 1 THz attenuated rectification, the average response is 2.4 nV. For the Ni-NiO-ZnO-CrAu rectenna, the average 1 THz attenuated rectification is 36.9 nV. Assuming the diode resistance and responsivity are constant with respect

to the input voltage due to the AC input voltage being sufficiently low to be within the linear limit of the diode responsivity, the relative AC power to the diode is the ratio of the two measured open circuit voltages,

$$\frac{P_{AC_{1THz}}}{P_{AC_0}} = \frac{V_{OC_{1THz}}}{V_{OC_0}}. \tag{4.3.3}$$

No open circuit voltage above the noise was measured when the terahertz radiation was attenuated through the 1.5 THz bandpass filter for either material set. The ratio of attenuated rectification voltage to reference rectification voltage for the Ni-NiO-Nb_2O_5-CrAu rectenna is 8%, while that for the Ni-NiO-ZnO-CrAu rectenna is 42%. Additional attenuated power measurements are recorded in Table 4.5 and Table 4.6.

Table 4.5: Results of the 1 THz attenuated power rectification for Ni-NiO-Nb_2O_5-CrAu diodes.

	Resistance (Ω)	**Responsivity (A/W)**	**V_{oc} Reference (nV)**	**V_{oc} 1 THz BPF (nV)**	**Attenuated Power Ratio**
	697	0.45	2.42	39.66	6.1%
	669	0.49	3.58	48.24	7.4%
	589	0.49	1.95	40.18	4.8%
	549	0.45	2.25	29.87	7.5%
	601	0.45	2.62	26.20	10.0%
	657	0.35	2.62	42.72	6.1%
	566	0.51	1.94	38.74	5.0%
	528	0.48	1.79	27.14	6.6%
	524	0.48	2.09	24.91	8.4%
	568	0.43	1.90	19.64	9.7%
	713	0.49	3.13	24.47	12.8%
AVERAGE	**605**	**0.46**	**2.39**	**32.89**	**7.7%**
STD DEVIATION	**64**	**0.04**	**0.54**	**8.85**	**2.3%**

Table 4.6: Results of the 1 THz attenuated power rectification for Ni-NiO-ZnO-CrAu diodes.

	R_D (Ω)	β_0 (A/W)	V_{OC} Reference (nV)	V_{OC} 1 THz BPF(nV)	Attenuated Power Ratio
	463	0.19	16.4	3.5	21.5%
	1506	0.68	98.9	37.7	38.1%
	1410	0.64	74.7	35.1	46.9%
	2258	0.30	45.6	27.8	61.0%
	1745	0.65	111.3	53.6	48.2%
	1471	0.63	100.4	53.3	53.1%
	1021	0.32	43.1	11.3	26.1%
	1506	0.66	111.3	52.2	46.9%
	1554	0.67	107.8	44.0	40.8%
	1535	0.65	109.8	42.5	38.7%
	1560	0.67	116.5	44.5	38.2%
AVERAGE	**1457**	**0.55**	**85.1**	**36.9**	**41.8%**
STD DEVIATION	**420**	**0.18**	**33.1**	**15.9**	**10.8%**

For the rectenna measured here, the bandwidth and resonance frequency for the Ni-NiO-Nb_2O_5-CrAu is difficult to determine. The slight increase in rectified voltage suggests the rectenna resonant frequency is further away from the bandwidth of the 1 THz bandpass filter, either closer to 800 GHz or 1.2 THz, while having some bandwidth that absorbs a range of frequencies that passes through the bandpass filter. For the Ni-NiO-ZnO-CrAu rectenna, the bandwidth and resonance frequency of the rectenna is likely closer to the central wavelength of the 1 THz bandpass filter. This difference could be due to the cut-off frequency of the rectenna, defined in Appendix I.III. The cut-off frequency,

$$f_C = \frac{1}{2\pi\left(\frac{R_A R_D}{R_A + R_D}\right) C_D}, \tag{4.3.4}$$

is the limiting frequency of rectenna operation. It depends on the resistance of the antenna, R_A, the diode resistance, R_D, and the diode capacitance, C_D. Because of the higher capacitance of the

Ni-NiO-Nb_2O_5-CrAu rectenna compared to the Ni-NiO-ZnO-CrAu antenna, the cut-off frequency is expected to be lower for the Ni-NiO-Nb_2O_5-CrAu material set. The cut-off frequency could be reducing the bandwidth of the device to a smaller bandwidth than the antenna bandwidth.

4.4 Rectenna Efficiency

The rectenna efficiency is defined as the ratio of the DC output power converted from the AC input power [26],

$$\eta_{rectenna} = \eta_{ant}\eta_{diode} = \frac{P_{DC}}{P_{THz}}. \tag{4.4.1}$$

The DC power can be calculated from the measured open circuit voltage from the lock-in amplifier,

$$P_{DC} = \frac{{V_{OC}}^2}{4R_D}. \tag{4.4.2}$$

Using the calculations for the power into the rectenna, the terahertz power absorbed by the antenna is roughly 0.75 nW. Using this as the total power of the antenna bandwidth, the rectification efficiencies of the rectenna are 7.1×10^{-10} and 1.7×10^{-9} for the Ni-NiO-Nb_2O_5-CrAu and Ni-NiO-ZnO-CrAu devices, respectively. This rectification efficiency is 1000× larger than reported rectification efficiencies at 28 THz [33]. The differences largely are associated with the RC coupling mismatch. The diodes in this study were lower resistance and provided better RC coupling to the antenna, especially considering the difference in operating frequency. The antenna efficiency is broken into two different components: antenna radiation efficiency and the antenna coupling efficiency. The antenna radiation efficiency is estimated to be > 90% at the operating frequencies of the antenna. The antenna coupling efficiency, Equation (1.5.9), is a function of the impedance matching of the antenna and the diode.

4.5 Conclusions

Two sets of MIIM diode rectenna were characterized with a four-point probe to give the diode's DC characteristics. The rectenna were measured under illumination of terahertz radiation using a THz-TDS setup with PCA emitter. The AC input power calculated from the measurements from each rectenna averaged 0.75 nW when accounting for the antenna and RC impedance match efficiency. Rectification was confirmed by rotating the rectenna polarization with respect to the terahertz polarization. By performing the polarization study and illuminating linear devices, the primary mechanism of rectification that explains the results was determined. The attenuated rectification through a 1 THz BPF was measured, confirming the rectenna responds to terahertz radiation near 1 THz. Overall, rectification of terahertz radiation by MIIM rectenna was examined and compared. The calculated rectification efficiencies are 7.1×10^{-10} and 1.7×10^{-9} for the Ni-NiO-Nb_2O_5-CrAu and Ni-NiO-ZnO-CrAu rectenna, respectively. The Ni-NiO-Nb_2O_5-CrAu rectenna likely responded primarily by the photoelectric effect with very little contribution from thermal effects. The Ni-NiO-ZnO-CrAu rectenna responded by a combination of photoelectric and thermal effects. The higher rectification efficiencies of the Ni-NiO-ZnO-CrAu material set is likely because of a better impedance matching efficiency due to the lower capacitance and the larger thermal contributions from the low zinc oxide thermal conductivity. Future work should primarily target the confirmation of the operating frequency of the rectenna and possibly, the capacitance of the diode. Additionally, preliminary work, shown in Appendix II.III, has been done on diode capacitance compensation circuits that would reduce the effective capacitance of the diode. By reducing this effective capacitance, more current would be driven through the diode by increasing the RC impedance matching efficiency.

Chapter 5 Conclusions and Future Work

The two-term exponential function is fit to I(V) data of MIIM diodes to better understand the characteristics of a diode. Justification for continued development and use of the two-term exponential function is provided to avoid overfitting using polynomial functions. The exponential function for a diode is used to develop an analytical model that correlates well to a Simulink model. The mathematical model can be used when AC input voltages enter the non-linear regime for the responsivity to approximate the DC output voltage. Additionally, the analytical model provides a quick and easy estimation for the optimal load resistance for a power extracting system. Using the two-term exponential function, a figure of merit is presented to scale all diodes from linear to the Shockley diode. The figure of merit better describes the rectifying capabilities of a diode than the typical asymmetry because the asymmetry is a function of the device responsivity, an already important figure of merit for rectification. Due to the requirement for a higher power AC source and the fabrication limitations of the samples, future work should focus on experimental validation rather than a conceptual model using Simulink using higher power sources and different material sets.

The THz-TDS is used to generate terahertz radiation. The power for the terahertz radiation is measured and compared to the estimated power at the diode using the Fourier transform of the time-domain spectrum. While the estimation includes some of the largest contributors to the reduced detection of the zinc telluride used in the system, further validation of the transfer functions or any additional transfer functions should be examined, especially accounting for the phase retardation in ZnTe and terahertz propagation effects. Future work should explore the shape of the terahertz power spectrum below 1 THz.

Finally, zero-bias rectification of MIIM rectenna was examined. The MIIM rectenna responded under illumination of the terahertz radiation that is confirmed through a study of the polarization dependence of the rectenna and the attenuated rectification through the 1 THz bandpass filter. The polarization study provides insight into the primary mechanism of rectification. Further examination of other diode material sets should be performed to optimize the rectification response. Further attenuated power studies should be performed to confirm the operating frequencies of the rectenna.

Ultimately, the measurement of the rectenna at zero-bias provides a step towards the harvesting of electromagnetic energy. Due to the low density of energy available on Earth for these frequencies, the valuable information gained from these experiments should be applied to devices operating at higher, more energy-dense frequencies.

Appendix

Appendix I: Derivations

In this section of the appendix, many of the metrics and equations used throughout this work are derived and explained in further detail, including the small signal responsivity, the RC-coupling efficiency, and the cut-off frequency.

I.I Small Signal Responsivity

The responsivity is derived by starting with an AC voltage across the diode,

$$V = V_B + V_{AC}\cos\omega t\,, \tag{6.1.1}$$

where V_B is the bias voltage across the diode, V_{AC} is the magnitude of the AC voltage, and ω is the angular frequency of the AC voltage. For our purposes, the diodes in this study are operating at zero-bias, $V_B = 0$, but the derivation of the small signal responsivity is still the same if operating at a bias-voltage. The current through the diode is then a function of the voltage and time. In our case, we will take the Taylor expansion of the diode current around our bias voltage,

$$I(V,t) = I(0) + \frac{dI}{dV}\bigg|_{V=0}[V_{AC}\cos(\omega t)] + \frac{1}{2}\frac{d^2I}{dV^2}\bigg|_{V=0}[V_{AC}\cos(\omega)]^2. \tag{6.1.2}$$

Since the bias voltage is the DC term and in our case is zero, it can be dropped, and the average current can be determined by integrating over one full cycle, $2\pi/\omega$,

$$\langle I\rangle = \frac{{V_{AC}}^2}{4}\frac{d^2I}{dV^2}\bigg|_{V=0}. \tag{6.1.3}$$

The responsivity is defined as the DC response to some AC input power,

$$P_{AC} = \frac{{V_{AC}}^2}{2R_{diff}}, \tag{6.1.4}$$

where R_{diff} is the differential resistance of the diode, defined in Equation (1.5.4). Then, taking the average direct current per input power yields the zero-bias responsivity,

$$\beta_0 = \frac{\langle I \rangle}{P_{AC}} = \frac{1}{2}\left[\frac{\frac{d^2 I}{dV^2}}{\frac{dI}{dV}}\right]_{V=0} . \tag{6.1.5}$$

This is also the responsivity at any bias voltage when the DC current term in Equation (6.1.2) is dropped.

I.II Resistance-Capacitance Coupling Efficiency

The resistance-capacitance coupling efficiency can be derived by using a similar circuit to that shown in Figure 2.1. This circuit is shown in Figure 6.1. In this circuit, R_D is the diode resistance, R_A is the real part of the antenna impedance, and C_D is the diode capacitance.

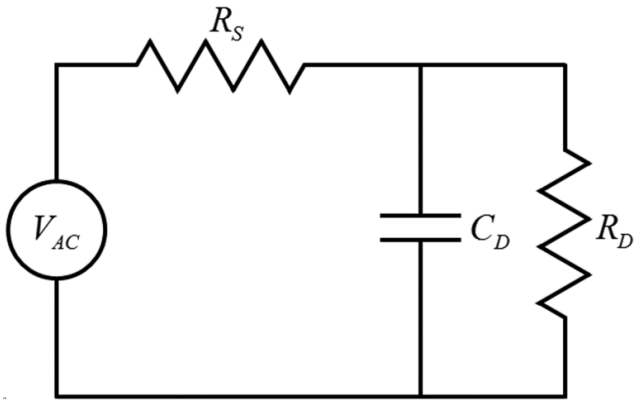

Figure 6.1: Rectenna circuit used for calculating the RC coupling efficiency, the ratio of the power delivered to the diode to the maximum power that could be delivered to the diode when R_D is equal to R_A and C_D is zero.

The AC input voltage into the circuit is the real part of the AC voltage given by:

$$V_{AC} \equiv Re\{V_0 e^{i\omega t}\}, \tag{6.2.1}$$

where V_0 is the amplitude of the AC voltage, ω is the angular frequency and t is time. From this circuit, the impedance of the diode is

$$Z_{R_D \| C_D} = \frac{R_D}{1 + i\omega C_D R_D} = R_D \left| Z_{R_D \| C_D} \right| e^{i\varphi_{R_D \| C_D}}, \tag{6.2.2}$$

where $\varphi_{Rd\|Cd}$ is the phase of the diode impedance. The total impedance of the circuit,

$$Z_{tot} = R_A + \frac{1}{\frac{1}{R_D} + i\omega C_D} \equiv |Z_{tot}| e^{i\varphi_{tot}}, \tag{6.2.3}$$

where φ_{tot} is the phase of the total impedance of the circuit, can be used to determine the current in the circuit as a function of time,

$$I(t) = \frac{V_{AC}}{Z_{tot}} = Re\left\{ \frac{V_0}{|Z_{tot}|} e^{i(\omega t - \varphi_{tot})} \right\}. \tag{6.2.4}$$

The voltage across the diode as a function of time is given by

$$V_D(t) = I(t) Z_{R_D \| C_D} = Re\left\{ \frac{V_0 R_D \left| Z_{R_D \| C_D} \right|}{|Z_{tot}|} e^{i(\omega t + \varphi_{R_D \| C_D} - \varphi_{tot})} \right\} \tag{6.2.5}$$

which gives the current in the diode as a function of time as

$$I_D(t) = \frac{V_D(t)}{R_D} = Re\left\{ V_0 \frac{\left| Z_{R_D \| C_D} \right|}{|Z_{tot}|} e^{i(\omega t + \varphi_{R_D \| C_D} - \varphi_{tot})} \right\}. \tag{6.2.6}$$

Using Euler's formula [58],

$$e^{i(\omega t + \varphi_{R_D \| C_D} - \varphi_{tot})} = \cos\left(\omega t + \varphi_{R_D \| C_D} - \varphi_{tot}\right) + i \sin\left(\omega t + \varphi_{R_D \| C_D} - \varphi_{tot}\right), \tag{6.2.7}$$

the real part of both the diode voltage, V_D, and diode current, I_D, can be determined and used to calculate the average power delivered to the diode:

$$\langle P_D \rangle = \frac{\omega}{2\pi} \int_0^{2\pi/\omega} V_D(t) I_D(t) = \frac{\omega}{2\pi} R_D \frac{{V_0}^2 \left| Z_{R_D \| C_D} \right|^2}{|Z_{tot}|^2} \int_0^{2\pi/\omega} \cos^2\left(\omega t + \varphi_{R_D \| C_D} - \varphi_{tot}\right) dt\,. \tag{6.2.8}$$

Equation (6.2.8) gives the average power delivered to the diode as:

$$\langle P_D \rangle = \frac{R_D {V_0}^2}{2} \frac{\left|Z_{R_D \| C_D}\right|^2}{|Z_{tot}|^2} = \frac{R_D {V_0}^2}{2} \frac{1}{(R_A + R_D)^2 + (\omega C_D R_A R_D)^2}. \quad (6.2.9)$$

The maximum power that can be delivered to the diode occurs when the antenna impedance, R_A, is equal to the diode resistance, R_D, and the diode capacitance, C_D, is zero,

$$\langle P_{D_{max}} \rangle = \frac{{V_0}^2}{8R_A}. \quad (6.2.10)$$

The RC coupling efficiency, η_{RC}, is determined by taking the ratio of the power delivered to the diode for any circuit to that maximum power that can be delivered to the diode for an optimal circuit,

$$\eta_{RC} = \frac{\langle P_D \rangle}{\langle P_{D_{max}} \rangle} = \frac{\frac{4R_A R_D}{(R_A + R_D)^2}}{1 + \left(\frac{R_A R_D}{R_A + R_D} \omega C_D\right)^2}. \quad (6.2.11)$$

I.III Cut-Off Frequency

The cut-off frequency, f_c, is determined from Equation (6.2.11) and based on the RC time constant [16]. The cut-off frequency of the rectenna is determined by the antenna resistance, R_A, the diode resistance, R_D, and the diode capacitance, C_D. The cut-off frequency is the highest operating frequency where the capacitive impedance of the diode is less than the parallel resistance of the diode; thus, more current is driven through the capacitive, or lossy, branch of the diode and the RC coupling to the antenna is poor. First, Equation (6.2.11) is rewritten as:

$$\eta_{RC} = \frac{4R_A R_D}{(R_A + R_D)^2 + (\omega C_D R_A R_D)^2}. \quad (6.3.1)$$

The rectenna cut-off frequency is determined when the two terms in the denominator are equal. At frequencies above the cut-off frequency, the right-hand term in the denominator is larger than the left-hand term.

$$(R_A + R_D)^2 = (2\pi f_c C_D R_A R_D)^2 \tag{6.3.2}$$

Thus, the cut-off frequency is

$$f_c = \frac{R_A + R_D}{2\pi C_D R_A R_D} = \frac{1}{2\pi \frac{R_A R_D}{(R_A + R_D)} C_D}. \tag{6.3.3}$$

Appendix II: Supporting Data

In this section, supporting data for all measured devices, linear or non-linear, for both material sets are presented. Additionally, a section is provided for capacitance compensation structures that have been measured as part of this work. The cumulative population densities of the resistance and responsivity for both material sets are shown in Figure 6.2 and Figure 6.3, respectively.

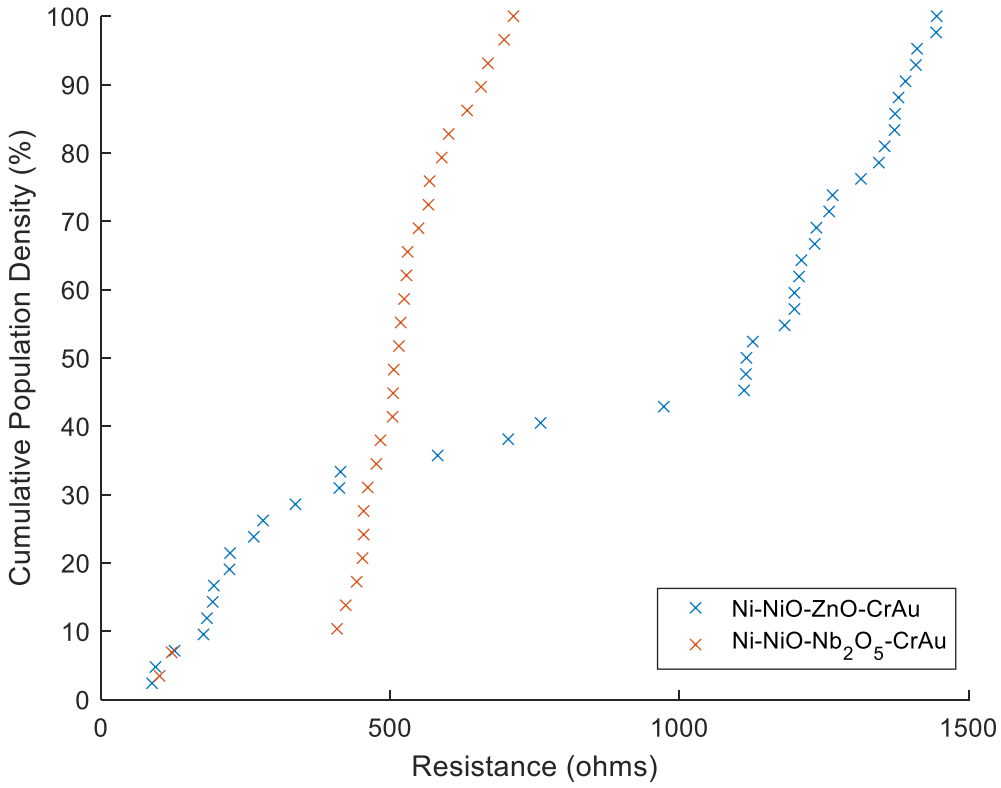

Figure 6.2: The cumulative population density of the diode resistance of all rectenna devices from both material sets that were tested under terahertz illumination. This includes linear and non-linear devices.

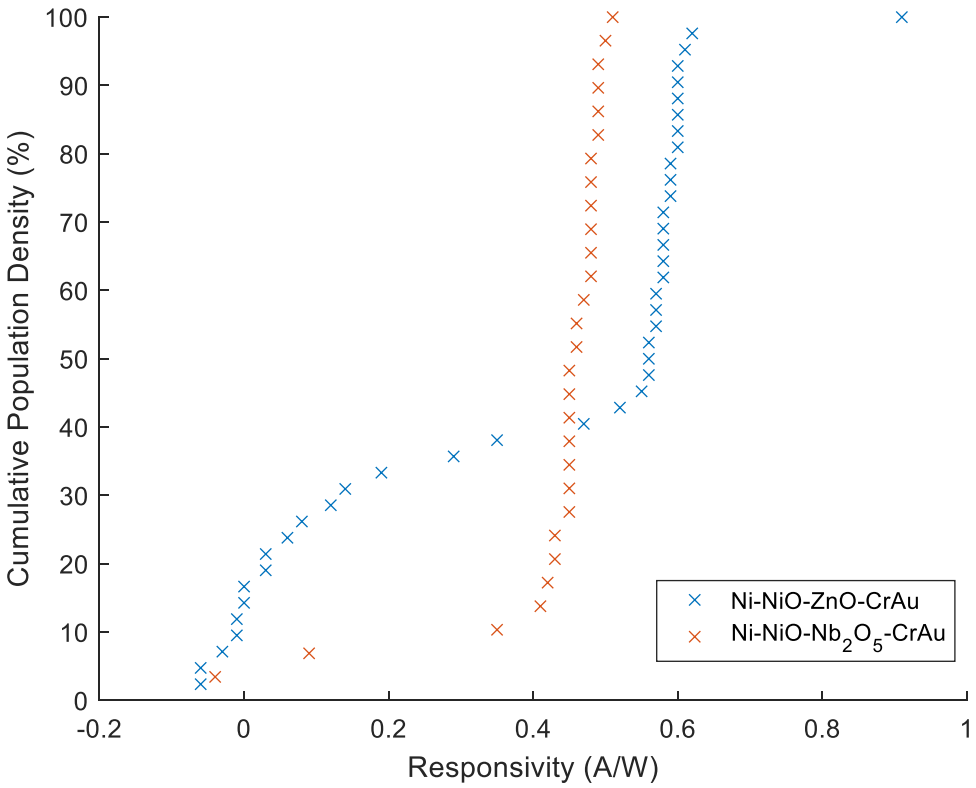

Figure 6.3: The cumulative population density of the diode responsivity of all rectenna devices from both material sets that were tested under terahertz illumination. This includes linear and non-linear devices.

II.I Ni-NiO-Nb_2O_5-CrAu Device Measurements

All results for Ni-NiO-Nb_2O_5-CrAu rectenna that were tested under terahertz illumination are gathered in Table 6.1. The linear devices showed no response to the terahertz illumination.

Table 6.1: Tabulated results displayed for all terahertz rectification studies of Ni-NiO-Nb_2O_5-CrAu rectenna for both linear and non-linear devices. Linear devices are italicized for emphasis.

R_D (Ω)	β_0 (A/W)	V_{OC} (nV)	Measured P_{DC} Out (W)	Calculated P_{AC} In (W)	Rectenna Efficiency (%)
483	0.46	40.9	8.64E-19	9.12E-10	9.47E-08
423	0.41	34.1	6.89E-19	8.84E-10	7.79E-08
452	0.45	34	6.41E-19	7.94E-10	8.07E-08
442	0.45	29.1	4.78E-19	6.73E-10	7.11E-08
408	0.48	33.6	6.92E-19	7.45E-10	9.29E-08
476	0.5	26	3.54E-19	5.39E-10	6.57E-08
461	0.45	26.7	3.86E-19	6.14E-10	6.28E-08
505	0.45	30.4	4.56E-19	7.02E-10	6.51E-08
633	0.48	61.8	1.51E-18	1.30E-09	1.16E-07
101	*-0.04*	*-0.1*	*1.25E-23*	*2.91E-11*	*4.31E-11*
657	0.35	40.8	6.35E-19	1.16E-09	5.48E-08
566	0.51	40.8	7.36E-19	8.20E-10	8.97E-08
506	0.48	30.2	4.51E-19	6.47E-10	6.97E-08
515	0.47	34.8	5.87E-19	7.66E-10	7.67E-08
454	0.42	32.7	5.90E-19	8.05E-10	7.33E-08
454	0.49	20.2	2.25E-19	4.32E-10	5.22E-08
518	0.43	29.4	4.16E-19	6.97E-10	5.98E-08
530	0.48	25.8	3.14E-19	5.52E-10	5.69E-08
122	*0.09*	*1.3*	*3.49E-21*	*2.23E-10*	*1.56E-09*
504	0.46	27.4	3.71E-19	6.09E-10	6.09E-08
713	0.49	38.8	5.28E-19	7.87E-10	6.71E-08
568	0.43	22.9	2.32E-19	5.38E-10	4.31E-08
524	0.48	30.5	4.45E-19	6.55E-10	6.79E-08
528	0.48	33.2	5.23E-19	7.09E-10	7.37E-08
601	0.45	27.5	3.14E-19	6.19E-10	5.08E-08
549	0.45	33.1	5.00E-19	7.43E-10	6.73E-08
589	0.49	40	6.80E-19	8.30E-10	8.18E-08
669	0.49	40.9	6.26E-19	8.27E-10	7.57E-08
697	0.45	42.2	6.38E-19	9.38E-10	6.80E-08

II.II Ni-NiO-ZnO-CrAu Device Measurements

All results for Ni-NiO-ZnO-CrAu rectenna that were tested under terahertz illumination are gathered in Table 6.2. The linear devices showed no response to the terahertz illumination. Other devices with lower resistance and responsivity are also included. These devices were excluded because it is expected that the devices fabricated in the same lot, under the same conditions, should have similar resistances and responsivity. The deviation from the rest of the lot suggests a possible dielectric breakdown of the diode.

Table 6.2: Tabulated results displayed for all terahertz rectification studies of Ni-NiO-ZnO-CrAu rectenna for both linear and non-linear devices. Linear devices are italicized for emphasis. Additional results are included for non-linear devices that had lower resistance and responsivity.

R_D (Ω)	β_0 (A/W)	V_{OC} (nV)	Measured P_{DC} Out (W)	Calculated P_{AC} In (W)	Rectenna Efficiency (%)
1644	0.64	96.1	1.41E-18	7.06E-10	1.99E-07
1669	0.64	102.6	1.58E-18	7.50E-10	2.10E-07
1707	0.61	81.8	9.79E-19	6.25E-10	1.57E-07
1648	0.61	77.8	9.18E-19	6.02E-10	1.52E-07
1576	0.62	73.7	8.61E-19	5.60E-10	1.54E-07
94	*-0.03*	*-0.9*	*2.37E-21*	*4.96E-10*	*4.79E-10*
588	0.19	29.4	3.68E-19	8.16E-10	4.51E-08
459	0.11	12.6	8.67E-20	6.39E-10	1.36E-08
650	0.27	33.1	4.21E-19	6.54E-10	6.44E-08
565	0.20	19.1	1.61E-19	5.20E-10	3.09E-08
1568	0.64	120.8	2.33E-18	8.96E-10	2.60E-07
1628	0.68	94.1	1.36E-18	6.55E-10	2.08E-07
1524	0.66	101.9	1.70E-18	7.28E-10	2.34E-07
131	*-0.01*	*-1.5*	*4.41E-21*	*3.11E-09*	*1.42E-10*
1461	0.64	86.2	1.27E-18	6.37E-10	1.99E-07
1570	0.65	91.5	1.33E-18	6.66E-10	2.00E-07
1520	0.66	85.7	1.21E-18	6.18E-10	1.96E-07
1548	0.61	80.5	1.05E-18	6.21E-10	1.69E-07
1475	0.65	88.8	1.34E-18	6.52E-10	2.05E-07
31	*-0.02*	*0.7*	*4.35E-21*	*-1.71E-09*	*-2.55E-10*
165	*0.04*	*-0.5*	*3.46E-22*	*-9.56E-11*	*-3.62E-10*
463	0.19	16.4	1.45E-19	4.87E-10	2.98E-08
1506	0.68	98.9	1.62E-18	6.89E-10	2.36E-07
1410	0.64	74.7	9.89E-19	5.56E-10	1.78E-07
2258	0.30	45.6	2.31E-19	7.13E-10	3.24E-08
1745	0.65	111.3	1.77E-18	8.01E-10	2.21E-07
1471	0.63	100.4	1.71E-18	7.61E-10	2.25E-07
1021	0.32	43.1	4.54E-19	6.58E-10	6.90E-08
1506	0.66	111.3	2.06E-18	7.95E-10	2.59E-07
1554	0.67	107.8	1.87E-18	7.61E-10	2.46E-07
1535	0.65	109.8	1.97E-18	7.97E-10	2.47E-07
1560	0.67	116.5	2.17E-18	8.21E-10	2.65E-07

II.III Capacitance Compensation Measurements

A large factor in the low efficiency of these MIIM rectenna is the diode capacitance. It reduces the RC coupling efficiency quickly until the diode reaches its cut-off frequency. Some work has been performed to reduce the effective capacitance of the diodes. The work suggested the use of capacitance circuit compensation structures that effectively reduce the diode capacitance, or imaginary part of the diode, such that more of the current is driven through the real, or resistive, part of the diode for rectification. The compensation structures used here are capacitive and inductive branches added to the AC portion of the rectenna circuit. An illustration of the physical compensation structures in a rectenna is shown in Figure 6.4. The compensation structure consists of five structural parameters that are varied to alter the effect of the compensation circuit. Depicted in Figure 6.5, these five parameters are the trace length, stub-2 position, stub length, diode position and linear separation. The physical dimensions of these structures in provided in Table 6.3.

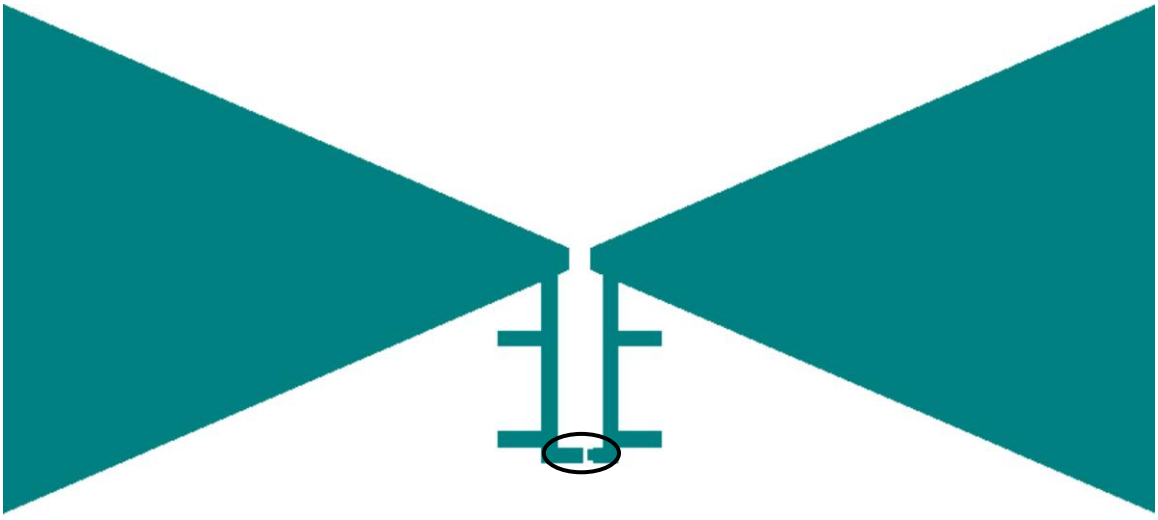

Figure 6.4: The rectenna with a compensation structure is illustrated. The diode in the compensation structure device is located at the point where the branches come together, highlighted by the black circle. The compensation structure acts to effectively reduce the diode capacitance.

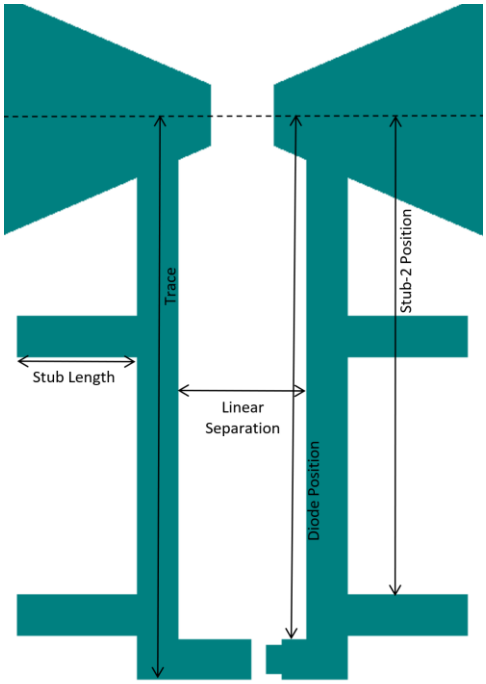

Figure 6.5: The five physical structures within the compensation structure that affect the diode capacitance are provided. The dimensions of these structures are provided in Table 6.3.

Table 6.3: The physical dimensions of the compensation structures that have been tested for their ability to effectively reduce the diode capacitance are provided.

Compensation Structure Type	Trace (µm)	Stub-2 Position (µm)	Stub Length (µm)	Diode Position (µm)	Linear Separation (µm)
1	14	11.9	3	13	3.2
2	13.5	11.9	3	12.5	3.2
3	14.5	11.9	3	13	3.2
4	14	11.85	3	13	3.2
5	14	11.95	3	13	3.2
6	14	11.9	2.5	13	3.2
7	14	11.9	3.5	13	3.2
8	14.5	11.9	3	13.5	3.2
9	14	11.9	3	12.5	3.2
10	14	11.9	3	13	2.8
11	14	11.9	3	13	3.6

Preliminary results for these compensation structures for both material sets are presented in Table 6.4 and Table 6.5. Additional work is required identifying the diode capacitance such that a structure that reduces the effective capacitance of the diode can be deduced. Some compensation structures should increase the impedance of the diode in the rectenna circuit so that the RC coupling efficiency decreases and these such rectenna would rectify less AC voltage. It is possible the Ni-NiO-ZnO-CrAu rectenna has such a low capacitance, as fabricated, that the compensation structure does little to increase the RC coupling efficiency. Each rectenna device with a compensation structure was tested under terahertz illumination, as with the experiments in Section 4.3.1. For the purposes of comparison, the AC power into each rectenna was assumed to be 0.75 nW, the average AC power that was calculated by the lumped element devices, and the effective diode capacitance was calculated using Equation (1.5.9), the RC coupling efficiency.

Table 6.4: The results of the Ni-NiO-Nb_2O_5-CrAu rectenna with compensation circuits, provided in Figure 6.5 and Table 6.3, is presented. The capacitance is calculated from the RC efficiency, Equation (1.5.9), for an antenna impedance of 100 Ω at 1 THz with an AC power of 0.75 nW.

Compensation Structure Type	**R_D (Ω)**	**β_0 (A/W)**	**V_{OC} (nV)**	**Calculated Capacitance (fF)**
5	549	0.29	10.9	6.03
5	629	0.15	3.7	7.65
7	448	0.38	14.3	6.05
8	506	0.38	17.5	5.39
8	439	0.38	13.7	6.21
9	504	0.32	14.9	5.36
9	436	0.37	18.1	5.24
10	505	0.37	16.8	5.48
10	506	0.38	16.2	5.61
11	485	0.35	11.4	6.53

Table 6.5: The results of the Ni-NiO-ZnO-CrAu rectenna with compensation circuits, provided in Figure 6.5 and Table 6.3, is presented. The capacitance is calculated from the RC efficiency, Equation (1.5.9), for an antenna impedance of 100 Ω at 1 THz with an AC power of 0.75 nW.

Compensation Structure Type	R_D (Ω)	β_0 (A/W)	V_{OC} (nV)	Calculated Capacitance (fF)
1	1445	0.52	62.9	2.09
1	1409	0.56	74.6	1.88
1	1391	0.58	85.7	1.64
2	1345	0.57	68.9	2.06
2	1199	0.56	66.1	2.09
2	1199	0.58	82.5	1.68
2	1115	0.58	65.2	2.19
3	1379	0.56	76.5	1.82
3	1265	0.55	75.8	1.79
3	1127	0.58	64.4	2.24
4	1116	0.57	70.0	2.00
4	1112	0.59	77.4	1.85
6	1314	0.58	80.3	1.76
6	1207	0.60	86.3	1.66
6	760	0.35	32.4	2.55
7	1234	0.59	86.6	1.64
7	1355	0.62	90.3	1.65
8	1444	0.57	82.8	1.67
9	1237	0.61	98.6	1.42
9	1259	0.60	65.4	2.30
10	1411	0.60	74.8	2.00
10	1182	0.60	58.0	2.54
11	1373	0.60	88.0	1.64
11	1372	0.59	91.3	1.53
11	1211	0.60	3.2	14.00
11	973	0.47	44.9	2.51

Bibliography

[1] N. Tesla, My Inventions, New York City: Experimenter Publishing Company, Inc., 1919.

[2] N. Tesla, "The Transmission of Electrical Energy Without Wires as a Means for Furthering Peace," *Electrical World and Engineer,* pp. 21-24, 1905.

[3] W. Brown, "The History on Power Transmission by Radio Waves," *IEEE Transactions on Microwave Theory and Techniques,* Vols. MTT-32, no. 9, pp. 1230-1242, 1984.

[4] W. Brown, "Experiments in the transportation of energy by microwave beam," in *IEEE International Convention*, New York City, NY, 1964.

[5] W. Brown, J. Mims and N. Heenan, "An Experimental Microwave-Powered Helicopter," in *IRE International Convention*, New York City, NY, 1965.

[6] E. C. Okress, Microwave Power Engineering: Generation, Transmission, Rectification, Waltham, MA: Academic Press, 2017.

[7] W. Brown, "Microwave to DC converter". US Patent 3434678A, 25 03 1969.

[8] R. Bailey, "Electromagnetic Wave Energy Converter". US Patent 3760257, 18 09 1973.

[9] W. C. Brown, "Optimization of the Efficiency and Other Properties of the Rectenna Element," in *1976 IEEE-MTT-S International Microwave Symposium*, Cherry Hill, NJ, 1976.

[10] S. S. Mohammed, K. Ramasamy and T. Shanmuganantham, "Wireless Power Transmission - A Next Generation Power Transmission System," *International Journal of Computer Applications,* vol. 1, no. 13, pp. 100-103, 2010.

[11] A. Khan, J. G., F. Gahaffar and A. Shamim, "Metal-insulator-metal diodes with sub-nanometre surface roughness for energy-harvesting applications," *Microelectronic Engineering,* vol. 181, pp. 34-42, 2017.

[12] C. Henry, "Limiting efficiencies of ideal single and multiple energy gap terrestrial solar cells," *Journal of Applied Physics,* vol. 51, pp. 4494-4500, 1980.

[13] W. Shockley and H. J. Queisser, "Detailed Balance Limit of Efficiency of *p-n* Junction Solar Cells," *Journal of Applied Physics,* vol. 32, no. 3, pp. 510-519, 1961.

[14] P. Landsberg and P. Baruch, "The thermodynamics of the conversion of radiation energy for photovoltaics," *Journal of Physics A: Mathematical and General,* vol. 22, no. 11, pp. 1911-1926, 1989.

[15] A. Sanchez, C. Davis, K. Liu and A. Javan, "The MOM Tunneling diode: Theoretical estimate of its performance at microwave and infrared frequencies," *Journal of Applied Physics,* vol. 49, no. 10, pp. 5270-5277, 1978.

[16] G. Moddel and S. Grover, Rectenna Solar Cells, New York City: Springer Science and Business Media, 2013, pp. 209-227.

[17] S. Krishnan, S. Bhansali, K. Buckle and E. and Stefankos, "Fabrication and Characterization of Thin-Film Metal-Insulator-Metal Diode for Use in Rectenna as Infrared Dectector," *MRS Proceedings,* vol. 935, no. 1, pp. 0935-K03-18, 2006.

[18] Z. Zhu, S. Joshi and G. Moddel, "High Performance Room Temperature Rectenna IR Detectors Using Graphene Geometric Diodes," *IEEE Journal of Selected Topics in Quantum Electronics,* vol. 20, no. 6, pp. 70-78, 2014.

[19] L. Cabral, "Annual Energy Review," U.S. Energy Information Administration, 2017.

[20] D. V. Schroeder, An Introduction to Thermal Physics, San Francisco, CA: Addison Wesley Longman, 1999.

[21] S. Grover and G. Moddel, "Engineering the current-voltage characteristics of metal-insulator-metal diodes using double-insulator tunnel barriers," *Solid-State Electronics,* vol. 67, no. 1, pp. 94-99, 2012.

[22] S. Joshi and G. Moddel, "Optical rectenna operation: where Maxwell meets Einstein," *Applied Physics,* vol. 49, no. 26, 2016.

[23] M. Shanawani, D. Masotti and A. Costanzo, "THz Rectennas and Their Design Rules," *Electronics,* vol. 6, no. 4, p. 99, 2017.

[24] F. Habbal, W. Danchi and M. Tinkham, "Photon-assisted tunneling at 246 and 604 GHz in small-area superconducting tunnel junctions," *Applied Physics Letters,* vol. 42, no. 3, pp. 296-298, 1983.

[25] J. R. Tucker and M. J. Feldman, "Quantum detection at millimeter wavelengths," *Rev. Mod. Phys.,* vol. 57, no. 4, pp. 1055-1113, 1985.

[26] E. Donchev, J. S. Pang, P. M. Gammon, A. Centeno, F. Xie, P. K. Petrov, J. D. Breeze, M. P. Ryan, D. J. Riley and N. M. Alford, "The rectenna device: From theory to practice (a review)," *MRS Energy & Sustainability,* vol. 1, no. 1, pp. 1-34, 2014.

[27] C. D. Garbo, P. Livreri and G. Vitale, "Optimal matching between optical rectennas and harvester circuits," in *IEEE International Conference on Environmental and Electrical Engineering and 2017 IEEE Industrial and Commercial Power Systems Europe*, Milan, Italy, 2017.

[28] S. B. Herner, A. Belkadi, A. Weerakkody, B. Pelz and G. Moddel, "Responsivity-Resistance Relationship in MIIM Diodes," *Journal of Photovoltaics,* vol. 8, no. 2, pp. 499-504, 2018.

[29] S. Krishnan, H. La Rosa, E. Stefanakos, S. Bhansali and K. Buckle, "Design and development of batch fabricable metal-insulator-metal diode and microstrip slot antenna as rectenna elements," *Sensors and Actuators A: Physical,* vol. 142, no. 1, pp. 40-47, 2008.

[30] M. Dagenais, "Solar spectrum rectification using nano-antenna and tunneling diodes," in *SPIE Optoelectronic Integrated Circuits*, San Francisco, CA, 2010.

[31] A. Singh, "Fabrication and current-voltage characteristics of NiOx/ZnO based MIIM tunnel diode," *Applied Surface Science,* vol. 334, no. 15, pp. 197-204, 2015.

[32] S. Herner, A. Weerakkody, A. Belkadi and G. Moddel, "High performance MIIM diode based on cobalt oxide/titanium oxide," *Applied Physics Letters,* vol. 110, no. 22, 2017.

[33] G. Jayaswal, A. Belkadi, A. Meredov, B. Pelz, G. Moddel and S. A., "Optical rectification through an Al2O3 based MIM passive rectenna at 28.3 THz," *Materials Today Energy,* vol. 7, pp. 1-9, 2018.

[34] M. Gadalla, M. Abdel-Rahman and A. Shamim, "Design, Optimization, and Fabrication of a 28.3 THz Nano-Rectenna for Infrared Detection and Rectification," *Scientific Reports,* vol. 4, no. 4270, 2014.

[35] E. Ozkan, M. Inac, A. Shaique, M. Ozcan and Y. Gurbuz, "The metal-insulator-metal diodes for infrared energy harvesting and detection applications," *SPIE Defense and Security, International Society for Optics and Photonics,* pp. 98190F-98190F, 2016.

[36] B. Pelz, A. Belkadi and G. Moddel, "Avoiding Erroneous Analysis of MIM Diode Current-Voltage Characteristics: Exponential Fitting," *Journal of Thin Solid Films,* vol. 120, pp. 28-33, 2018.

[37] W. Shockley, "The theory of *p-n* junctions in semiconductors and *p-n* junction transistors," *The Bell System Technical Journal,* vol. 28, no. 3, pp. 435-489, 1949.

[38] Z. Thacker, "Terahertz Materials for Energy Harvesting Rectenna," Ph.D. Dissertation, University of Missouri, Columbia, MO, 2016.

[39] B. Pelz, A. Belkadi and G. Moddel, "Traveling-Wave Metal-Insulator-Metal Diodes for Infrared Rectennas," in *2016 IEEE 43rd Photovoltaic Specialists Conference (PVSC)*, Portland, OR, 2016.

[40] Z. Thacker and P. J. Pinhero, "Terahertz Spectroscopy of Candidate Oxides in MIM Diodes for Terahertz Detection," *IEEE Transactions on Terahertz Science and Technology,* vol. 6, no. 3, pp. 414-419, 2016.

[41] MATLAB, "MathWorks Products and Services," The MathWorks, Inc., [Online]. Available: https://www.mathworks.com/. [Accessed 2018].

[42] P. Midya, *private communciation,* 2017.

[43] Q. Wu and X.-C. Zhang, "Free-space electro-optic sampling of terahertz beams," *Appl. Phys. Lett.,* vol. 67, no. 24, pp. 3523-3525, 1995.

[44] S. Casalbuoni, H. Schlarb, H. Schmidt, P. Schmuser, B. Steffen and A. Winter, "Numerical studies on the electro-optic detection of femtosecond electron bunches," *Physical Review Special Topics - Accelerators and Beams,* vol. 11, no. 7, pp. 072802-072820, 2008.

[45] G. Gallot, J. Zhang, R. McGowan, T.-I. Jeon and D. Grischkowsky, "Measurements of the THz absorption and dispersion of ZnTe and their relevance to the electro-optic detection of THz radiation," *Appl. Phys. Lett.,* vol. 74, no. 23, pp. 3450-3452, 1999.

[46] H. Bakker, G. Cho, H. Kurz, Q. Wu and X.-C. Zhang, "Distortion of terahertz pulses in electro-optic sampling," *Optical Society of America,* vol. 15, no. 6, pp. 1795-1801, 1998.

[47] "Thorlabs," Thorlabs, Inc., [Online]. Available: https://www.thorlabs.com/.

[48] J. Faure, J. van Tilborg, R. Kaindl and W. Leemans, "Modelling laser-based table-top THz sources: Optical rectification, propagation and electro-optic sampling," *Optical and Quantum Electronics,* vol. 36, no. 8, pp. 681-697, 2004.

[49] Z. Thacker, *private communication,* 2018.

[50] E. Hecht, Optics, San Francisco, CA: Pearson Education, Inc., 2002.

[51] D. Marple, "Refractive Index of ZnSe, ZnTe, and CdTe," *Applied Physics,* vol. 35, no. 539, 1964.

[52] L. Ward, "Zinc Selenide (ZnSe) Zinc Telluride (ZnTe)," in *Handbook of Optical Constants of Solids, Volume II*, Cambridge, MA, Academic Press, 1997, pp. 737-758.

[53] K. Choi, F. Yesilkoy, G. Ryu, S. H. Cho, N. Goldsman, M. Dagenais and M. Peckerar, "A focused asymmetric metal-insulator-metal tunneling diode: fabrication, DC characteristics, and RF rectification anaylsis," *IEEE Transactions on Electron Devices,* vol. 58, no. 10, pp. 3519-3528, 2011.

[54] J. R. Rumble, *Handbook of Chemistry and Physics, 98th Edition*, Boca Raton, FL: CRC Press, 2017.

[55] Y. Wang, W. Yin, Q. Han, X. Yang, H. Ye, Q. Lv and D. Yin, "Bolometric effect in a waveguide-intergrated graphene photodetector," *Chinese Physics B,* vol. 25, no. 11, p. 118103, 2016.

[56] K. H. Kim, S. H. Shim, K. B. Shim, K. Niihara and J. Hojo, "Microstructural and Thermoelectric Characteristics of Zinc Oxide-Based Thermoelectric Materials Fabricated Using a Spark Plasma Sintering Process," *Journal of American Ceramic Society,* vol. 88, no. 3, pp. 628-632, 2005.

[57] R. Janninck and D. Whitmore, "Thermoelectric Power in Nonstoichoimetric alpha-Nb2O5," *Journal of Chemical Physics,* vol. 39, no. 1, pp. 179-182, 1963.

[58] L. Euler, "On Transcending Quantities Arising from the Circle," in *Introductio In Analysin Infinitorum, Vol. 1*, Translated and annotated by Ian Bruce, 2013, pp. 202-233.